MODAL ANALYSIS OF RADIATION AND ENERGY STORAGE MECHANISMS ON CONDUCTING SCATTERERS

BY

KURT RICHARDSON SCHAB

DISSERTATION

Submitted in partial fulfillment of the requirements
for the degree of Doctor of Philosophy in Electrical and Computer Engineering
in the Graduate College of the
University of Illinois at Urbana-Champaign, 2016

Urbana, Illinois

Doctoral Committee:

Professor Jennifer Bernhard, Chair
Professor Steven Franke
Assistant Professor Songbin Gong
Professor Jianming Jin

ABSTRACT

The manifestation of radiation and stored energy by electric currents on conducting bodies is studied via modal expansions. The novel modal expansions are based on the quadratic operators which map a current distribution to each quantity. Adaptations of the continuous forms of these operators into the Method of Moments is reviewed. The discrete modal expansions are studied on several example objects, leading to conclusions regarding the sparsity of the radiation mode spectrum. Analytic forms for the sparse radiation modes on electrically small objects are derived. Negative energy current distributions are studied using the energy storage modal expansions. The role of ground plane radiation on the determination of an embedded antenna's Q factor is studied using radiation modes, giving a new perspective on the convergence behavior of this parameter with respect to ground plane size. Leveraging the invariance of radiation modes on small objects, an example procedure for the design of an embedded antenna array using radiation modes is presented.

ACKNOWLEDGMENTS

This dissertation's completion owes many thanks to those who supported me throughout my graduate studies. First and foremost, many thanks to my advisor Jennifer Bernhard for her wise coaching, both technical and professional. Additionally the input, critique, and motivation from faculty and my colleagues at the University of Illinois greatly helped in steering the focus of this work.

TABLE OF CONTENTS

NOTATION

r	Spatial location vector, shorthand for the special vector field $\vec{r}$ (see next definition). Vector notation is dropped for clarity except when needed to show explicit vector nature.
$\vec{a}(r)$	Vector field in $\mathbb{R}^3$ which is a function of spatial location, r.
a	Scalar.
a^*	Complex conjugate of a.
$\hat{A}\vec{f}(r)$	Vector field resulting from the operator $\hat{A}$ acting on the vector field $\vec{f}$.
$A\left(\vec{f}\right)$	Scalar value returned from the functional A acting on the vector field $\vec{f}$.
$\mathbf{a}$	N by 1 vector object.
$\mathbf{A}$	M by N array (matrix) object.
$\mathbf{a}^H$	Complex (Hermitian) transpose of $\mathbf{a}$.

CHAPTER 1

INTRODUCTION

This dissertation focuses on tying together modern electromagnetic analysis techniques (both analytic and computational) with practical insight that can be applied to antenna design. In particular, we focus on problems related to small antennas mounted to larger conducting objects, e.g., a miniaturized antenna mounted next to the circuit board in a mobile phone. Throughout this dissertation these types of systems will be referred to as embedded antennas. The research described here includes a new approach to understanding radiation and energy storage in such systems by way of a set of eigenvalue expansions. Because all antenna parameters are determined by these quantities, this approach yields novel insight into physical processes underlying an antenna's performance. Specifically, radiation and energy storage mechanisms can be effectively isolated, allowing for a critical examination of the colloquial "ground plane as a radiator" and "antenna as a matching network" notions.

Chapter 2 begins with an overview of the state-of-the-art source-based techniques used in contemporary antenna analysis and design. Following that introduction, Poynting's theorem is discussed in the context of the electric field integral equation, the backbone of the computational method of moments. Contemporary research on stored electromagnetic energy and its application in antenna design is then summarized and discussed both in terms of analytic approaches and the method of moments. The chapter concludes with a presentation of the novel set of radiation and energy storage eigenvalue problems used throughout the dissertation.

Because this research utilizes various numerical methods, the development of method of moments code is outlined in detail in Chapter 3. Therein we discuss various discretization techniques, a popular method for dealing with singular integral components, and problems related to tracking eigenvalue solutions over frequency.

In Chapter 4, we present examples of identifying the current mechanisms responsible for radiation and energy storage in antenna systems. In all of these examples, the novel expansions proposed in Chapter 2 are implemented using code making use of the techniques outlined in Chapter 3. As mentioned previously, this research is largely motivated by embedded antennas, or antennas mounted next to larger conducting objects. As such, the examples in this chapter include both a canonical antenna design and an embedded antenna topology. These examples shed light on the physical implications of the matrix properties of the maps connecting a current to its radiated power and stored energies.

Observations regarding the expansion associated with radiated power motivate the analytic studies presented in Chapter 5. There we derive closed-form expressions for the dominant solutions to the radiation eigenvalue problem on simple conducting structures. These analytic expressions are validated against numerical calculations. The result of these analyses is a connection between the readily-available electric-field integral equation impedance matrix and an object's canonical radiating moments.

To calculate stored electric magnetic energies from arbitrary currents we use a recently-developed matrix operator technique. In the literature, the mathematical properties of the matrices associated with this method are commonly quoted as being indicative of non-physical and therefore erroneous calculations of "negative energy" on electrically large objects. In Chapter 6, we use the energy storage modal expansion to study the loss of positive-semi-definiteness of the energy storage matrices responsible for this anomalous behavior. Results show that the threshold for energy matrix loss of positive-semi-definiteness depends on geometry. Further, the currents responsible for "negative energy" are simple.

In Chapter 7 we use several metrics, including the novel radiation mode expansion, to study the effective electrical size of an antenna system consisting of a small driven element mounted on or near a finite ground plane. Using radiation mode expansion, we quantify the relation between ground plane size and radiation complexity in order to describe the design regimes where ground plane radiation is dominant over that of the small antenna element. Additionally, the quality factor of the antenna systems are calculated as functions of ground plane size, giving some indication as to the capability of a finite ground plane to add to the electrical size (and thus increase the

bandwidth) of a small antenna. Three metrics for quality factor are used; and their comparison shows that the loss of positive-semi-definiteness discussed in the Chapter 6 has little effect in the calculation of Q for electrically large, low bandwidth systems.

The derivation of analytic forms of radiation modes in Chapter 5 corroborate the observations from examples in Chapter 3. Using the knowledge that electrically small objects radiate via only a few low-order radiation modes, a novel approach to beamforming with these modes is proposed in Chapter 8. Instead of treating several antennas mounted to a finite ground plane as radiators, the small antennas are treated merely as feeds to a radiating ground plane. The basic structure of this approach has been proposed before using characteristic modes, however in this chapter we demonstrate the utility and advantages of a radiation modes for this particular application. The proposed method, along with an example design of a two-element null-steering array is presented.

An overview of the methods and results from each component of the research is given at the beginning of each chapter. These results are reiterated and discussed in detail in the summary contained in Chapter 9. There we also propose further research questions, both fundamental and applied.

CHAPTER 2

RADIATION AND ENERGY STORAGE MODES

2.1 Overview

Motivation and background is provided for techniques primarily focused on the calculation of antenna performance parameters in terms of source current distributions. State-of-the-art techniques for calculating physical quantities such as radiated power and stored energy are discussed in both continuous and discrete implementations. Novel radiation and energy storage eigenvalue problems are presented based on these contemporary calculation techniques.

2.2 Source-based analyses

The Institute of Electrical and Electronics Engineers (IEEE) defines an antenna as "the part of a transmitting or receiving system that is designed to radiate or receive electromagnetic waves" [1]. A more useful definition may define an antenna as a system component used to transduce signals between guided and unguided form. Here guided refers to signals and systems analyzable by circuit theory (waveguide systems, shielded cable components, printed circuit boards, fiber optic connections, etc.), whereas "unguided" refers to signals analyzed by electromagnetic field analysis in an unbounded space (radiation, near-field energy, etc.). From a practical point of view, antennas under this definition bridge the gap between the circuit and free-space aspects of a wireless system. As such, a designer will have objectives and concerns in both worlds. Of primary interest on the circuit side is the antenna's input impedance and its behavior over frequency. This will determine the impedance match of the antenna to the "guided" portion of the system as well as its operating bandwidth. In the unguided regime, design

objectives include radiation pattern, radiation efficiency, and polarization. These parameters describe how energy is converted between guided signals and waves in free-space. Both the circuit and radiation performance of an antenna are of great importance for proper system performance. Generally, the task of designing an antenna is decoupled into two components, that of achieving proper circuit performance and that of obtaining desirable radiation characteristics. Both of these sets of properties are governed implicitly by the antenna geometry and its feeding structure, as shown schematically in Figure 2.1. The link between the structure of an antenna and its realized performance is its excited current distribution, generally including surface currents on conducting surfaces, polarization currents in dielectrics, and equivalent magnetic currents formed by aperture fields. A current distribution is present in both transmit and receive modes of operation, but for simplicity here language is restricted that of a transmitting antenna. In this dissertation, focus is put on perfect electrically conducting (PEC) antennas with electric surface currents. As shown in Figure 2.1, the antenna's geometry, feed, and loading dictate its current distribution which in turn determine both the circuit and field characteristics of the device. The design process is represented by the backwards arrow: the role of the antenna designer is to manipulate a structure so it will achieve certain performance expectations by proxy of the currents it supports. Classical antenna design focused on simple objects with predictable current patterns analyzable by closed-form or heuristic methods [2], [3]. Performance of these designs was modified by small perturbations to the geometry or feed location driven mainly by intuition and similarity to other canonical problems. This approach is still widely used today, though the process is often automated using iterative simulation tools to optimize a baseline heuristic design.

Research into more modern antenna design strategies is driven in no small part by the internalization of antennas within small portable devices [4]. In such devices, there may exist conducting bodies over which the antenna designer has no control and the volume allocated for an antenna is relatively small compared to the entire system. In these cases, the common knowledge is that the larger conducting portions of the device will radiate and that the mounted antenna acts mainly to excite currents on the chassis [5]. Techniques involving the calculation and analysis of the currents on the chassis and within the antenna design volume are termed "source-based" [6].

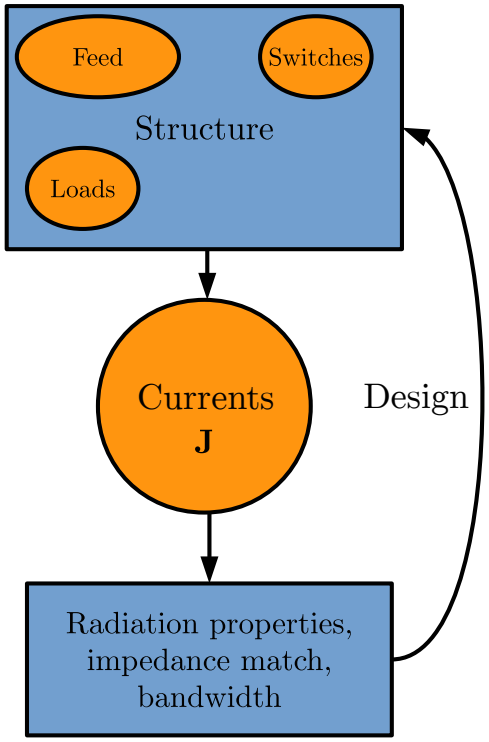

Figure 2.1: Schematic of the process by which structural features of the antenna influence its circuit and field characteristics by way of the currents supported on its surface. The backwards arrow represents the inverse problem, i.e., the design process of synthesizing an antenna which has the desired circuit and field parameters.

Source-based methods include applications of characteristic mode decomposition [7, 8, 9], current-based Q calculations [10, 11], and optimal currents for minimal stored energy [12, 13]. All of the aforementioned techniques involve manipulation of matrices calculated via the method of moments and inform which current mechanisms are available to achieve optimal performance. While source-based tools offer simple, fast analysis of current distributions, the missing link in antenna design is still how to design antennas and feed structures which can support and excite the desired current. Recent work has started to bridge this gap by incorporating source-based analyses into automated design. In [14], energy storage calculations were included in an optimization to design a pixelated antenna with minimal Q, maximiz-

ing narrowband bandwidth. In [15], a multiband antenna was optimized to support only one resonant characteristic mode at each operating frequency. The authors of [16] used a pixelated approach to optimize an antenna with a single resonant characteristic mode and addressed some of the problems associated with the popular technique of pixelized optimization. In each of these examples, source-based calculations were used to calculate costs in an optimization routine. While in each paper there is discussion of basic design choices (e.g., feed location, orientation, etc.), the end designs are not necessarily intuitive and leave the questions "why did this come out this way?" and "will it come out the same way if I run it again?" These questions do not devalue the approaches used, but rather they elucidate work still to be done in understanding the output of optimization tools using source-based objectives. In contrast to these examples of fully automated optimization, other source-based designs draw direct inspiration from canonical current distributions which are known to have desirable properties. Examples in the literature include several instances of designs using spherical geometries to support currents with minimal Q [17] and which induce self-tuning using characteristic modes [18]. While these designs are intuitively and analytically satisfying, their restrictive geometries make them ill-suited for antennas mounted inside small devices.

In subsequent sections of this chapter, energy storage and radiation are discussed in the context of source-based, method of moments techniques. Following that, a new set of source-based modal decompositions is presented. The goal of these novel decompositions is to isolate currents on a structure which contribute most to stored electric energy, stored magnetic energy, and radiated power. To do this, the approach used in characteristic modes of making the modal expansions based on matrix operators derived from the method of moments is adopted. Because of this, the expansions are independent of feed location and easily manipulated during pixellization or other automated design processes. The new expansions proposed in this chapter differ from characteristic modes in that these eigenvalue problems do not couple fields associated with radiation and stored energy. This allows for clear views of radiation and energy storage current mechanisms, particularly in embedded antenna systems.

2.3 Energy and radiation functionals

In this section, the electric field integral equation (EFIE) is developed along with the standard method of moments impedance matrix, $\mathbf{Z}$. Splitting this matrix into real and imaginary parts yields the radiation and energy difference matrix operators $\mathbf{R}$ and $\mathbf{X}$, respectively. The continuous operators associated with stored electric and magnetic energy are also discussed, along with a modified method of moments calculation used to arrive at their discrete matrix forms.

2.3.1 The electric field integral equation and the impedance matrix

The electric field at an observation point r due to a current $\vec{J}$ distributed over a surface S in free space is calculated using the dyadic Green's function via

$$\vec{E}_{sc}(\vec{r}) = -\frac{j\eta k}{4\pi} \int_{S'} \bar{\bar{G}}(r, r') \cdot \vec{J}(r') dr'. \tag{2.1}$$

The integral on the right-hand side can be expressed in three ways, containing either derivatives of the free space Green's function $G_0(r, r')$

$$\vec{E}_{sc}(\vec{r}) = -\frac{j\eta k}{4\pi} \int_{S'} \left[\bar{\bar{I}} + \frac{\nabla\nabla}{k^2} \right] G_0(r, r') \cdot \vec{J}(r') dr', \tag{2.2}$$

derivatives of the source distribution

$$\vec{E}_{sc}(\vec{r}) = -\frac{j\eta k}{4\pi} \int_{S'} \left[\vec{J}(r') + \frac{1}{k^2} \nabla'\nabla' \cdot \vec{J}(r') \right] \cdot G_0(r, r') dr', \tag{2.3}$$

or one derivative on each

$$\vec{E}_{sc}(\vec{r}) = -\frac{j\eta k}{4\pi} \int_{S'} \left[G_0(r, r') \vec{J}(r') + \frac{1}{k^2} \nabla G_0 \nabla' \cdot \vec{J}(r') \right] dr'. \tag{2.4}$$

Here the free space Green's function $G_0(r, r')$ is defined as

$$G_0(r, r') = \frac{e^{-jk|r-r'|}}{|r - r'|}. \tag{2.5}$$

Making S a perfect electrical conductor (PEC) imposes the boundary condition that the total tangential electric field at observation points $r \in S$ must

be zero. This total field is the sum of both the field due the the current on S (also called the scattered field), $\vec{E}_{sc}$, and the incident field $\vec{E}_i$. Defining the unit vector normal to S as $\hat{n}$, the PEC boundary condition is written as

$$\hat{n} \times \left(\vec{E}_{sc} + \vec{E}_i \right) = 0, \quad r \in S. \tag{2.6}$$

Substituting (2.4) into the above expression gives an integral equation relating the the incident tangential electric field to the induced current on S,

$$\hat{n} \times \vec{E}_i(\vec{r}) = \hat{n} \times \frac{j\eta k}{4\pi} \int_{S'} \left[G_0(r, r')\vec{J}(r') + \frac{1}{k^2} \nabla G_0 \nabla' \cdot \vec{J}(r') \right] dr'. \tag{2.7}$$

This is a form of the electric field integral equation (EFIE) [19]. We can apply the method of moments to discretize the system and convert the integral operator on the right-hand side into a matrix operator. In matrix form, the operator can easily be inverted to solve for the currents induced by a given incident field. This inverse solution is particularly useful for antenna analysis. Equation (2.7) has two important implications: first, (assuming one can invert the integral operator) one can solve for the currents due to an incident field; and second, given a current distribution one can easily calculate its scattered field. We now test both sides of (2.7) with $\vec{J}^*$ and integrate over S. Because $\vec{J}$ is restricted to the surface of S, the normal cross-product on both sides can be dropped. This yields

$$\int_S \vec{J}^*(r) \cdot \vec{E}_i(\vec{r}) dr = \int_S \vec{J}^*(r) \cdot \frac{j\eta k}{4\pi} \int_{S'} \left[G_0(r, r')\vec{J}(r') + \frac{1}{k^2} \nabla G_0 \nabla' \cdot \vec{J}(r') \right] dr' dr. \tag{2.8}$$

This can be rearranged using some manipulations involving the divergence theorem to give

$$\int_S \vec{J}^*(r) \cdot \vec{E}_i(\vec{r}) dr = \frac{j\eta k}{4\pi} \int_S \int_{S'} \left[\vec{J}^*(r) \cdot \vec{J}(r') - \frac{1}{k^2} \nabla \cdot \vec{J}^*(r) \nabla' \cdot \vec{J}(r') \right] G_0(r, r') dr' dr. \tag{2.9}$$

The left-hand side now resembles the expression used to denote "source power" in Poynting's theorem. If we assume for a moment that the incident field is localized to a small aperture (e.g., the gap feed on a dipole or the opening on a coaxial cable on a probe-fed microstrip patch antenna), the integrand of the left-hand side will be non-zero over only a small region. The left-hand side then takes the form of $P = I^* V_i$, where P is the complex power provided to the antenna by the feed, I is the current at the feed location, and V_i is the driving voltage. In effect, (2.9) relates the complex power at the antenna terminal to the current density over the whole surface S. We put this observation aside for now, but it will be an important concept used when discussing the non-linear functionals which give the radiated power and stored energies from a current distribution. To discretize (2.9), a set of N vector basis functions $\{\vec{\psi}_n\}$ is introduced which are reasonably complete over S. Both $\vec{J}$ and $\vec{E}_i$ can be expanded in terms of $\{\vec{\psi}_n\}$ as

$$\vec{J}(r) = \sum_{n=1}^{N} J_n \vec{\psi}_n \tag{2.10}$$

and

$$\vec{E}_i(r) = \sum_{n=1}^{N} V_n \vec{\psi}_n. \tag{2.11}$$

The vectors $\mathbf{J}$ and $\mathbf{V}$ contain the coefficients $\{J_n\}$ and $\{V_n\}$, respectively. Inserting these expansions into (2.9) gives the quadratic form

$$\mathbf{J}^H \mathbf{V} = \mathbf{J}^H \mathbf{Z} \mathbf{J}, \tag{2.12}$$

where the elements of $\mathbf{Z}$ and $\mathbf{V}$ are

$$Z_{mn} = \frac{j\eta k}{4\pi} \int_{S_m} \int_{S_n} \Big[\vec{\psi}_m^*(r) \cdot \vec{\psi}_n(r') - \frac{1}{k^2} \nabla \cdot \vec{\psi}_m^*(r) \nabla' \cdot \vec{\psi}_n(r') \Big] G_0(r, r') dr' dr \tag{2.13}$$

and

$$V_m = \int_{S_m} \vec{\psi}_m^*(r) \cdot \vec{E}_i(\vec{r}) dr. \tag{2.14}$$

Drawing from the observations made before, (2.12) represents a discrete form of Poynting's theorem. In an alternate derivation, testing (2.8) with a single basis function and following the same procedure, yields the linear system

$$\mathbf{V} = \mathbf{Z}\mathbf{J}. \tag{2.15}$$

Equation (2.12) can be derived from (2.15), but the previous observation regarding its relation to Poynting's theorem is not necessarily obvious by following that train of thought. Due to the explicit use of Galerkin's testing, the impedance matrix, $\mathbf{Z}$, is symmetric. The elements of $\mathbf{Z}$ depend only on the structure of S, the form of basis functions used, and the operating frequency. All information about excitation is contained in the vector $\mathbf{V}$. Inverting $\mathbf{Z}$ in (2.15) is a straightforward method for calculating the currents on an antenna for a given excitation.

We can split the impedance matrix into its real and imaginary parts

$$\mathbf{Z} = \mathbf{R} + j\mathbf{X}, \tag{2.16}$$

where $\mathbf{R}$ and $\mathbf{X}$ are symmetric and real-valued. Inserting this expansion into (2.12) leads to

$$\mathbf{J}^H\mathbf{V} = \mathbf{J}^H\mathbf{R}\mathbf{J} + j\mathbf{J}^H\mathbf{X}\mathbf{J}. \tag{2.17}$$

By the symmetric real nature of $\mathbf{R}$ and $\mathbf{X}$, both quadratics on the right-hand side of (2.17) are real for all $\mathbf{J}$. Comparing the real and imaginary parts of the above expression with Poynting's theorem we find

$$P_{rad} = \mathbf{J}^H\mathbf{R}\mathbf{J} \tag{2.18}$$

and

$$2\omega\left(\bar{W}_m - \bar{W}_e\right) = \mathbf{J}^H\mathbf{X}\mathbf{J}. \tag{2.19}$$

Note that $\mathbf{J}$ is rms normalized while $\vec{J}$ is peak normalized. The quadratics in (2.18) and (2.19) are interpreted as the reaction integral of $\vec{J}$ with the in-phase and quadrature components of the electric field which it produces. From a practical standpoint, $\mathbf{R}$ and $\mathbf{X}$ are readily available from a complete impedance matrix by taking the real and imaginary parts of $\mathbf{Z}$. Thus, with the impedance matrix constructed, we can calculate the radiated power and

time-average reactive energy difference due to any current representable in **J**. In order to calculate other field-based quantities, such as radiation Q, it is necessary to find the individual stored energy components, $\bar{W}_e$ and $\bar{W}_m$, which are not available using the preceding method of moments approach. Section 2.3.2 covers the functionals derived in [10] which give the energy quantities $\bar{W}_e$ and $\bar{W}_m$ individually in terms of a current distribution $\vec{J}$. The conversion of those functionals into matrix quadratic forms similar to those in (2.18) and (2.19) is also discussed.

2.3.2 Stored energy functionals

Antenna radiation Q is defined as the ratio of stored energy to radiated power

$$Q = 2\omega \frac{\max\{\bar{W}_e, \bar{W}_m\}}{P_{rad}}, \tag{2.20}$$

and is generally used as a metric of narrowband antenna bandwidth analogously to how it is used for other circuit components [20], [21]. The history of calculating antenna Q is long and varied; with many researchers taking a wide range of approaches. The primary difficulty in finding a general expression for Q arises in calculating the non-propagating stored energies, $\bar{W}_e$ and $\bar{W}_m$. The total stored energies are classically defined from Poynting's theorem as

$$\bar{W}_{e,T} = \frac{1}{4} \int_V \varepsilon |\vec{E}(r)|^2 dV \tag{2.21}$$

and

$$\bar{W}_{m,T} = \frac{1}{4} \int_V \mu |\vec{H}(r)|^2 dV. \tag{2.22}$$

The integrals in these definitions are taken over all space and include both stored energies in the near-field (non-propagating) and those associated with far-field radiation (propagating) [22]. The latter component is infinite and is not relevant for Q calculations. To obtain the near-field energies alone, many authors have used subtraction methods to remove the energy stored in the far-field (e.g., [22], [23], [24]) but this technique works only when closed-form expressions are known for the fields around the antenna or a canonical geometry is used. For general antennas, this method is difficult to apply. Following

the approach used in [25] and [26], Vandenbosch derived general expressions for the non-propagating stored energy around an antenna in terms of finite integrals over its source current distribution [10], [11]. That derivation involves the use of a frequency derivative form of Poynting's theorem and extensive manipulations involving the scalar Green's function and its derivatives. The resulting expressions for these non-infinite stored energies are

$$2\omega\bar{W}_m = \frac{\eta_0}{4\pi k}\int_S\int_{S'} k^2\vec{J}(r)\cdot\vec{J}(r')\frac{\cos\left(k|r-r'|\right)}{|r-r'|} - \frac{k}{2}\left[k^2\vec{J}(r)\cdot\vec{J}(r') - \nabla\cdot\vec{J}(r)\nabla'\cdot\vec{J}(r')\right]\sin\left(k|r-r'|\right)drdr' \quad (2.23)$$

and

$$2\omega\bar{W}_e = \frac{\eta_0}{4\pi k}\int_S\int_{S'} \nabla\cdot\vec{J}(r)\nabla'\cdot\vec{J}(r')\frac{\cos\left(k|r-r'|\right)}{|r-r'|} - \frac{k}{2}\left[k^2\vec{J}(r)\cdot\vec{J}(r') - \nabla\cdot\vec{J}(r)\nabla'\cdot\vec{J}(r')\right]\sin\left(k|r-r'|\right)drdr'. \quad (2.24)$$

For compactness, the following functional notation is adopted to represent the integrals on the right-hand sides of (2.23) and (2.24):

$$2\omega\bar{W}_m = X_m(\vec{J}), \quad (2.25)$$

$$2\omega\bar{W}_e = X_e(\vec{J}). \quad (2.26)$$

Using these relations, the non-propagating stored energies of any current distribution can be calculated by finite integrals. This is a critical result for calculating the Q of arbitrary currents and arbitrary antennas. The derivation in [10] is arduous but rigorous with the exception of the assumption that $\partial\vec{J}/\partial\omega = 0$. The implications of this assumption is discussed further in Chapter 6. In a response to [10], an alternative derivation of the same integral relations was presented using Poynting's theorem, Foster's reactance theorem, and a few *ad hoc* assumptions [27]. The alternative formulation is very compact; but as the original author points out, the assumptions made in intermediate steps are guided more by the existing final result rather than the underlying mathematics or physics [11]. In addition to the energy relations

in (2.23) and (2.24), a similar expression for the radiated power in terms of the source current is also presented in [10], given by

$$P_{rad} = \frac{\eta_0}{4\pi k} \int_S \int_{S'} \big[k^2 \vec{J}(r) \cdot \vec{J}(r') - \nabla \cdot \vec{J}(r) \nabla' \cdot \vec{J}(r')\big] \frac{\sin(k|r-r'|)}{|r-r'|} dr dr'. \quad (2.27)$$

Adopting the same shorthand notation we write this as

$$P_{rad} = R(\vec{J}). \quad (2.28)$$

To implement these integrals numerically, we follow the methods in [12] and expand $\vec{J}$ using the same basis set used in creating the method of moments impedance matrix. In this way, the integral operations in (2.23), (2.24), and (2.27) are converted into matrix multiplications. Inserting the expansion (2.10) into the above integral expressions we obtain the quadratic forms

$$2\omega \bar{W}_m = \mathbf{J}^H \mathbf{X}_m \mathbf{J}, \quad (2.29)$$

$$2\omega \bar{W}_e = \mathbf{J}^H \mathbf{X}_e \mathbf{J}, \quad (2.30)$$

and

$$P_{rad} = \mathbf{J}^H \mathbf{R} \mathbf{J}, \quad (2.31)$$

where the elements of each matrix operator are

$$X_{m,mn} = \frac{\eta_0}{4\pi k} \int_S \int_{S'} k^2 \vec{\psi}_m(r) \cdot \vec{\psi}_n(r') \frac{\cos(k|r-r'|)}{|r-r'|} - \frac{k}{2} \big[k^2 \vec{\psi}_m(r) \cdot \vec{\psi}_n(r') - \nabla \cdot \vec{\psi}_m(r) \nabla' \cdot \vec{\psi}_n(r')\big] \sin(k|r-r'|)\, dr dr', \quad (2.32)$$

$$X_{e,mn} = \frac{\eta_0}{4\pi k}\int_S\int_{S'} \nabla\cdot\vec{\psi}_m(r)\nabla'\cdot\vec{\psi}_n(r')\frac{\cos\left(k|r-r'|\right)}{|r-r'|} - \frac{k}{2}\left[k^2\vec{\psi}_m(r)\cdot\vec{\psi}_n(r') - \nabla\cdot\vec{\psi}_m(r)\nabla'\cdot\vec{\psi}_n(r')\right]\sin\left(k|r-r'|\right)drdr', \quad (2.33)$$

and

$$R_{mn} = \frac{\eta_0}{4\pi k}\int_S\int_{S'}\left[k^2\vec{\psi}_m(r)\cdot\vec{\psi}_n(r') - \nabla\cdot\vec{\psi}_m(r)\nabla'\cdot\vec{\psi}_n(r')\right]\frac{\sin\left(k|r-r'|\right)}{|r-r'|}drdr'. \quad (2.34)$$

By comparing (2.13) with (2.34) we see that $R_{mn} = \text{Re } Z_{mn}$. Hence (2.18) and (2.31) are identical and the discrete form of the integral relation for radiated power derived in [10] is the same as the real part of the impedance matrix obtained by the traditional method of moments using EFIE. Similarly, comparison of (2.13), (2.32), and (2.33) shows that $X_{m,mn} - X_{e,mn} = X_{mn} = \text{Im } Z_{mn}$. Unfortunately, there is no way to separate $X_{e,mn}$ and $X_{m,mn}$ from X_{mn} and these matrix elements must be calculated outside of a standard method of moments routine. Approximate methods using frequency derivatives of the impedance matrix have been reported and may result in agreeing figures, though these methods are still to be quantitatively compared with one another [28, 29, 30]. Inspecting the individual terms in (2.32) and (2.33) we observe that they have the forms [13]

$$X_{m,mn} = \frac{\eta_0}{4\pi k}\left(X^0_{m,mn} + X_{em,mn}\right) \quad (2.35)$$

and

$$X_{e,mn} = \frac{\eta_0}{4\pi k}\left(X^0_{e,mn} + X_{em,mn}\right), \quad (2.36)$$

where

$$X^0_{m,mn} = \int_S\int_{S'} k^2\vec{\psi}_m(r)\cdot\vec{\psi}_n(r')\frac{\cos\left(k|r-r'|\right)}{|r-r'|}drdr', \quad (2.37)$$

$$X^0_{e,mn} = \int_S\int_{S'} \nabla\cdot\vec{\psi}_m(r)\nabla'\cdot\vec{\psi}_n(r')\frac{\cos\left(k|r-r'|\right)}{|r-r'|}drdr', \quad (2.38)$$

and

$$X_{em,mn} = -\int_S \int_{S'} \frac{k}{2} \big[k^2 \vec{\psi}_m(r) \cdot \vec{\psi}_n(r') - \nabla \cdot \vec{\psi}_m(r) \nabla' \cdot \vec{\psi}_n(r')\big] \sin\left(k|r-r'|\right) dr dr'. \quad (2.39)$$

Both $X^0_{m,mn}$ and $X^0_{e,mn}$ are the imaginary parts of terms already calculated in Z_{mn}. These terms are usually calculated separately in method of moments code, so very little work is required to isolate them in existing code. These changes are discussed further in Chapter 3. The only remaining piece of the energy operators to calculate is then $X_{em,mn}$ which is common to both $X_{m,mn}$ and $X_{e,mn}$. This term clearly resembles those in Z_{mn} although it lacks the $1/R$ singularity. Therefore, with minor additions to existing code, the remaining integral term $X_{em,mn}$ is straightforward to obtain and does not require additional singularity treatment.

2.3.3 Comparing matrix and continuous operators

We can reconcile the quadratics forms in (2.29), (2.30), and (2.31) with the integrals in (2.23), (2.24), and (2.27) by rearranging the latter into inner products of $\vec{J}$ and the vector field returned from some operator acting upon it. For example, repeated application of the divergence theorem allows us to rewrite (2.27) as

$$P_{rad} = \frac{1}{2} \int_V J^*(r) \cdot \hat{R}\vec{J}(r) dV, \quad (2.40)$$

where we have defined the radiation operator $\hat{R}$ as

$$\hat{R}\vec{J}(r) = \frac{\eta k}{4\pi} \int_{V'} \left[\mathbf{I} + \frac{\nabla\nabla}{k^2}\right] \frac{\sin\left(kR\right)}{R} \cdot \vec{J}(r') dV'. \quad (2.41)$$

The relations for electric and magnetic stored energy can be written in a similar manner with the introduction of operators $\hat{X}_e$ and $\hat{X}_m$. Continuing with the radiation operator as an example, we note that $\mathbf{R}$ and $\hat{R}$ are related in the sense that product $\mathbf{RJ}$ returns a vector containing the coefficients of the vector field $\hat{R}\vec{J}$ tested by each basis function in $\{\vec{\psi}_m\}$. More precisely,

$$\mathbf{RJ}_m = \int_S \vec{\psi}_m(r) \cdot \hat{R}\vec{J}(r) dr. \tag{2.42}$$

While the structure and nature of $\hat{R}\vec{J}$ and $\mathbf{RJ}$ differ slightly due to this testing property, their physical meanings are still similar enough to deem them analogous. To reconstruct $\hat{R}\vec{J}$ from $\mathbf{RJ}$ we write it as a weighted expansion using the same basis functions, i.e.,

$$\hat{R}\vec{J}(r) = \sum_n \vec{\psi}_n \gamma_n. \tag{2.43}$$

Inserting this into (2.42) gives, after a few manipulations,

$$\mathbf{RJ} = \mathbf{P}\boldsymbol{\gamma}, \tag{2.44}$$

where

$$P_{mn} = \int_{V_m} \vec{\psi}_m \cdot \vec{\psi}_n dV_m. \tag{2.45}$$

The matrix $\mathbf{P}$ is called the scaling matrix and will be used to remove variations in $\mathbf{R}$ and other matrix operators caused by mesh effects.

2.3.4 Implications, applications, and issues of $\mathbf{R}$, $\mathbf{X}_e$, and $\mathbf{X}_m$

The quadratics in (2.29), (2.30), and (2.31) provide a means to calculate the stored magnetic energy, stored electric energy, and radiated power due to any current representable in $\mathbf{J}$. All three matrices are real and symmetric. For all objects, $\mathbf{R}$ is positive-semi-definite, resulting in any current radiating positive, real power. Some numerical inaccuracies can invalidate this physical requirement, but such non-positive-semi-definite matrices can by corrected to be positive-semi-definite easily with minimal consequence. For small objects ($ka < \lambda/3$), $\mathbf{X}_m$ and $\mathbf{X}_e$ are also positive-semi-definite, corresponding to all currents storing positive energy. However for larger objects ($ka > \lambda/3$), it has been observed that both $\mathbf{X}_m$ and $\mathbf{X}_e$ can systematically have negative eigenvalues [14]. Thus there exist, for larger objects, current distributions which appear to store negative energy. The physical issues with this, as well as more specifics on when it occurs, is the focus of Chapter 6. Assuming that analysis is restricted to small objects with positive-semi-definite energy

operators, the quadratics in (2.29), (2.30), and (2.31) can be used in (2.20) to calculate Q for any current distribution via

$$Q = 2\omega \frac{\max\{\mathbf{J}^H \mathbf{X}_m \mathbf{J}, \mathbf{J}^H \mathbf{X}_e \mathbf{J}\}}{\mathbf{J}^H \mathbf{R} \mathbf{J}}. \tag{2.46}$$

As discussed before, the matrices $\mathbf{X}_m$ and $\mathbf{X}_e$ are easy to calculate provided small changes in existing method of moments code can be made and the above expression lends itself well to the study of Q of arbitrary small objects. Bounds on Q for an arbitrary structure can be cast as a general optimization problem where the objective is to find the current distribution on that structure which generates minimum Q. Early attempts to do this involved traditional optimization techniques [31], though more recently the same authors adopted a modern approach using convex optimization [12, 13, 32, 33]. Furthermore, fast calculation of Q via (2.46) enables it to be incorporated as a cost in automated antenna shape synthesis [14]. Equation (2.46) has also been applied in the study of energy storage in characteristic modes [34]. The quadratic forms in (2.29) and (2.30) have further been identified as an intuitive means by which to discern numerical and physical crossing avoidances in characteristic mode eigenvalue tracking problems [35, 36].

2.4 Radiation and energy storage modes

Here the radiation and energy storage matrix operators discussed in previous sections are used to analyze which components of a current distribution contribute most to its total radiated power and stored energy. By doing this, we intend to elucidate if given substructures are dominant in the manifestation of these quantities. Observing where currents responsible for each quantity on a structure we can quantitatively understand the role of different regions of an object in producing radiation and stored energy. To do this, novel modal current expansions based on the matrix operators $\mathbf{R}$, $\mathbf{X}_m$, and $\mathbf{X}_e$ (originally presented in [37]) are developed. By sorting eigenmode magnitude in each expansion, a current distribution can be divided into contributing and non-contributing components, i.e., a radiating and non-radiating component from expansion in $\mathbf{R}$; a capacitive component and a non-capacitive component from $\mathbf{X}_e$; and an inductive component and a non-inductive component

from $\mathbf{X}_m$.

2.4.1 Eigenvalue problems in $\mathbf{R}$, $\mathbf{X}_e$, and $\mathbf{X}_m$

Define the matrix $\mathbf{L}$ to represent either $\mathbf{R}$, $\mathbf{X}_e$, or $\mathbf{X}_m$. We cast an eigenvalue problem related to $\mathbf{L}$ as

$$\mathbf{L}\mathbf{J}_n = \nu_n \mathbf{P}\mathbf{J}_n. \tag{2.47}$$

Because any choice of $\mathbf{L}$ is symmetric and real, the set of eigenmodes $\{\mathbf{J}_n\}$ forms a complete orthogonal set over the dimension of $\mathbf{L}$. We can normalize the modes to satisfy

$$\mathbf{J}_m^{lH}\mathbf{P}\mathbf{J}_n^l = \delta_{mn}. \tag{2.48}$$

$\mathbf{P}$ is taken to be the scaling matrix with elements given by (2.45) and is used here to remove eigenvalue dependence on meshing. Here the superscript l denotes the choice of $\mathbf{L}$. This notation is omitted for clarity in subsequent sections unless needed to avoid ambiguity. Any current $\mathbf{J}$ can be expanded into a particular eigenmode set by

$$\mathbf{J} = \sum_n \alpha_n^l \mathbf{J}_n^l, \tag{2.49}$$

where

$$\alpha_n^l = \mathbf{J}_n^{lH}\mathbf{P}\mathbf{J}. \tag{2.50}$$

Setting $\mathbf{L} = \mathbf{R}$ and substituting (2.49) into (2.18) using (2.47) and (2.48) gives a new power relation in terms of modal radiated powers:

$$P_{rad} = \sum_n |\alpha_n^r|^2 \nu_n^r = \sum_n p_{rad}^n. \tag{2.51}$$

Above, $|\alpha_n^r|^2\nu_n^r = p_{rad}^n$ is the power radiated by the n^{th} mode. Repeating this procedure using the other choices of $\mathbf{L}$, we arrive at similar expressions for total energies in terms of modal stored energies:

$$2\omega W_m = \sum_n |\alpha_n^m|^2 \nu_n^m = 2\omega \sum_n W_{m,n} \tag{2.52}$$

and

$$2\omega W_e = \sum_n |\alpha_n^e|^2 \nu_n^e = 2\omega \sum_n W_{e,n}. \tag{2.53}$$

2.4.2 Contributing and non-contributing current components

Here we propose that for each quantity (P_{rad}, $\bar{W}_e$, and $\bar{W}_m$), the total current $\mathbf{J}$ can be split into a contributing and a non-contributing components. For example, looking at radiated power we postulate that the current $\mathbf{J}$ consists of a radiating component $\mathbf{J}_r$ and a non-radiating component $\mathbf{J}_{nr}$, i.e.,

$$\mathbf{J} = \mathbf{J}_r + \mathbf{J}_{nr}. \tag{2.54}$$

Using (2.18), it follows that these components should have the properties

$$\mathbf{J}_r^H \mathbf{R} \mathbf{J}_r \approx P_{rad}, \tag{2.55}$$

$$\mathbf{J}_{nr}^H \mathbf{R} \mathbf{J}_{nr} \approx 0, \tag{2.56}$$

and

$$\mathbf{J}_{nr}^H \mathbf{R} \mathbf{J}_r \approx 0. \tag{2.57}$$

Examining (2.51) along with the above conditions, we can see that $\mathbf{J}_r$ must be composed of the radiation modes present in $\mathbf{J}$ which have non-trivial modal powers. For a modal power $|\alpha_n^r|^2 \nu_n^r$ to be non-trivial, both the excitation coefficient α_n^r and the eigenvalue must be non-zero. Hence the eigenspectrum of $\mathbf{R}$ indicates which modes are capable of radiating independent of excitation while the coefficients give a metric of how much of the total current projects onto each mode. Modes which are either not present in $\mathbf{J}$ or those which have trivially small eigenvalues do not contribute to radiation. We denote K as the minimum set of modes satisfying

$$P_{rad}^c = \sum_{n \in K} p_{rad}^n \geq c P_{rad}, \tag{2.58}$$

where $c \in [0, 1]$ is the minimum fraction of P_{rad} accounted for by the set of modes in K. For c sufficiently close to 1, the set K represents the minimum

set of radiation modes responsible for the radiation due to the total current distribution $\mathbf{J}$. All factors relevant to radiation (total power, radiation resistance, field patterns, etc.) can be attributed to the weighted sum of radiation modes in a current. Thus by adding together the properly weighted radiation modes in K we obtain the radiating current

$$\mathbf{J}_r^c = \sum_{n \in K} \alpha_n \mathbf{J}_n. \tag{2.59}$$

In general we set $c \geq 0.95$ and drop the superscript notation. By this logic, the non-radiating component of $\mathbf{J}$ is obtained by summing the modes not contained in K, i.e.,

$$\mathbf{J}_{nr} = \sum_{n \notin K} \alpha_n \mathbf{J}_n. \tag{2.60}$$

Thus, using the eigenmode expansion in (2.47) with $\mathbf{L} = \mathbf{R}$ enables the decomposition in (2.54) by identifying the set K which satisfies (2.58). The exact same process can be followed using the energy storage operators $\mathbf{X}_m$ and $\mathbf{X}_e$ to determine the modal mechanisms on a structure available for storing magnetic and electric energy. The effectiveness of this technique is demonstrated and discussed in Chapter 3.

CHAPTER 3

NUMERICAL METHODS

3.1 Overview

Numerical methods used to calculate the method of moments impedance matrix $\mathbf{Z}$ and the energy storage matrix operators $\mathbf{X}_m$ and $\mathbf{X}_e$ are presented. Basis function selection is covered with a discussion comparing Rao-Wilson-Glisson (RWG) and rooftop functions. The procedure for calculating the elements of $\mathbf{Z}$, $\mathbf{X}_m$, and $\mathbf{X}_e$, including the special considerations required to treat singular terms and maintain matrix operator symmetry, is also discussed. Techniques for tracking the eigenvalues of a parameterized matrix is presented in the context of tracking eigenvalue solutions of frequency-dependent matrices over broad bandwidths.

3.2 Basis function expansion

In order to calculate the matrix operators $\mathbf{Z}$, $\mathbf{X}_m$, and $\mathbf{X}_e$ for a given surface S, we must first create a set of basis functions $\{\vec{\psi}_n\}$ capable of supporting any reasonable vector function confined to and tangential to S. The first step in generating $\{\vec{\psi}_n\}$ is to discretize S into N_s subdomains. The subdomains are joined by N_e edges, each of which contacts exactly two subdomains. Edges contacting more than two subdomains require a special treatment which decomposes them into superpositions of two-domain edges. The set of edges, subdomains, and joining vertices will be referred to as the mesh of S throughout this dissertation. The nature exact nature of the basis functions themselves will depend on the discretization method used, which is the primary difference between Rao-Wilson-Glisson (RWG) and rooftop basis functions.

3.2.1 RWG basis functions

Established in [38], the RWG basis functions are an extremely common choice of basis function for electromagnetic simulation [3, 19, 39]. Each RWG basis function, $\vec{\Lambda}_n$ exists over the two triangular subdomains T_n^+ and T_n^- contacting the associated edge e_n, as shown in Figure 3.1. The piecewise expressions for $\vec{\Lambda}_n$ are

$$\vec{\Lambda}_n(\mathbf{r}) = \begin{cases} \vec{\Lambda}_n^+ = \frac{l_n}{2A_n^+}\boldsymbol{\rho}^+ & \mathbf{r} \in T_n^+ \\ \vec{\Lambda}_n^- = \frac{l_n}{2A_n^-}\boldsymbol{\rho}^- & \mathbf{r} \in T_n^-, \end{cases} \tag{3.1}$$

where l_n is the common edge length and $A_n^\pm$ is the area of $T_n^\pm$. The vectors $\boldsymbol{\rho}^\pm$ are given by

$$\boldsymbol{\rho}^\pm = \pm\mathbf{r} \mp \mathbf{r}_f^\pm, \tag{3.2}$$

where $\mathbf{r}_f^\pm$ is the free vertex of $T^\pm$. The integrals within the elements of $\mathbf{Z}$, $\mathbf{X}_m$, and $\mathbf{X}_e$ also require the divergence of these basis functions, which has the convenient form

$$\nabla \cdot \vec{\Lambda}_n(\mathbf{r}) = \begin{cases} \frac{l_n}{A_n^+} & \mathbf{r} \in T_n^+ \\ -\frac{l_n}{A_n^-} & \mathbf{r} \in T_n^-. \end{cases} \tag{3.3}$$

The tapered nature of the RWG basis functions maintains continuity at edges and triangle corners. Furthermore, the formulation of $\vec{\Lambda}_n$ ensures that the outward component of a vector field goes to zero on the outer boundaries of S; a built-in way of enforcing conservation of current at the edges of objects. Using triangular subdomains, objects with curved surfaces or high length-scale contrast can be accurately and efficiently represented. However, this comes at the cost of requiring adaptive meshing tools to generate appropriate meshes for a given geometry (e.g., distmesh [40] and gmsh [41]). In addition, locating edges in a mesh associated with a specific region and field orientation can be difficult after the mesh has been created. While this is not an issue if locations of feeds, ports, or loads are specified on an object prior to meshing, it can create problems and extra overhead when working with source-agnostic methods which study potential properties of arbitrary feed locations (e.g., characteristic modes). In general, a new mesh must be created for each geometry in order to appropriately conform to the object's

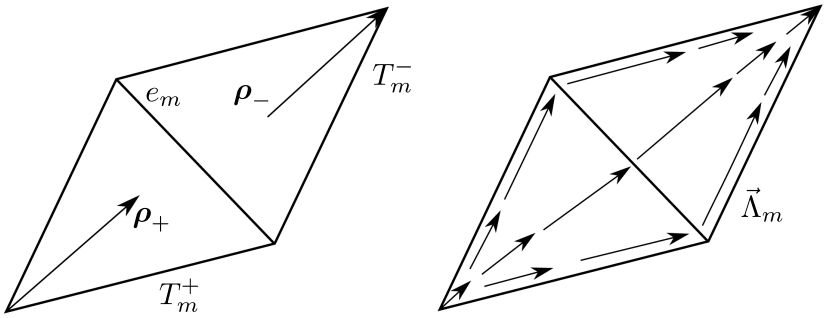

Figure 3.1: Schematic of an RWG basis function.

boundaries. That is, the mesh from one object cannot be truncated to synthesize an arbitrary secondary object (an exception to this is when triangle sizes are standardized and vertices restricted to a regular grid, as done in [16] and [42]).

3.2.2 Rooftop basis functions

In contrast to the triangular subdomains used in RWG basis functions, rooftop basis functions $\vec{\psi}_n$ are defined over two rectangles S_n^+ and S_n^-, joined by the edge e_n, as shown in Figure 3.2. The expressions defining $\vec{\psi}_n$ and its divergence are

$$\vec{\psi}_m(r) = \begin{cases} \vec{\psi}_m^+ = \left(1 - \frac{\mathbf{d}^+ \cdot \boldsymbol{\rho}^+}{|\mathbf{d}^+|}\right) \frac{\boldsymbol{d}^+}{|\mathbf{d}^+|} & r \in S_m^+ \\ \vec{\psi}_m^- = \left(1 + \frac{\mathbf{d}^- \cdot \boldsymbol{\rho}^-}{|\mathbf{d}^-|}\right) \frac{\boldsymbol{d}^-}{|\mathbf{d}^-|} & r \in S_m^- \end{cases} \tag{3.4}$$

$$\nabla \cdot \vec{\psi}_m(r) = \begin{cases} \frac{-1}{|\mathbf{d}^+|} & r \in S_m^+ \\ \frac{1}{|\mathbf{d}^-|} & r \in S_m^-. \end{cases} \tag{3.5}$$

The use of rectangular subdomains has several implications. First, one

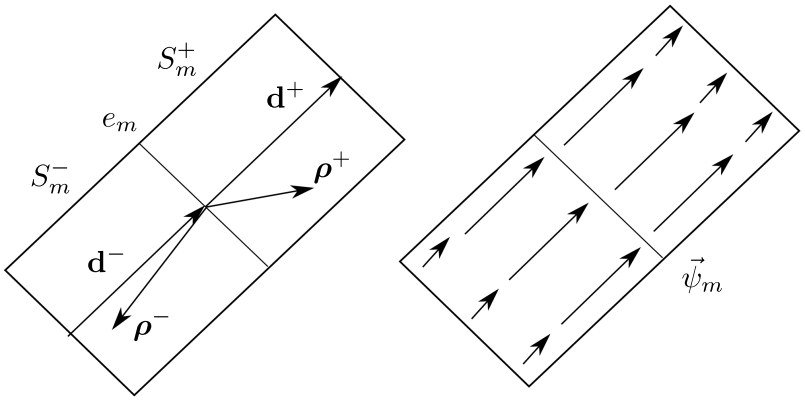

Figure 3.2: Schematic of a rooftop basis function.

must either restrict study to objects containing only right angles or accept pixelation errors at curved or oblique boundaries. Some curved objects can be synthesized accurately with rectangular domains (e.g., open cylinders, rings) but these are exceptional cases. Secondly, the rectangular grid requires uniform or quasi-uniform meshing over the entire object. For surfaces with high length-scale contrasts, this leads to unnecessarily large numbers of elements and is computationally inefficient. Rooftop functions do offer several advantages over RWG functions for certain problems. Uniform meshes can be generated using simple procedures and do not require adaptive meshing tools. Furthermore, once a large planar object is meshed, other regular planar shapes can be quickly created by truncating the mesh appropriately. Examples of this procedure are shown in Figure 3.3. This truncation is extremely efficient to implement in the calculation of EFIE-related matrix operators and is the basis of fast, efficient analysis of pixellated objects.

3.3 Calculation of matrix operators

The elements of $\mathbf{Z}$, $\mathbf{X}_m$, and $\mathbf{X}_e$ are given in (2.13), (2.33), and (2.32) respectively. Though we are also interested in $\mathbf{R}$ for performing radiation mode

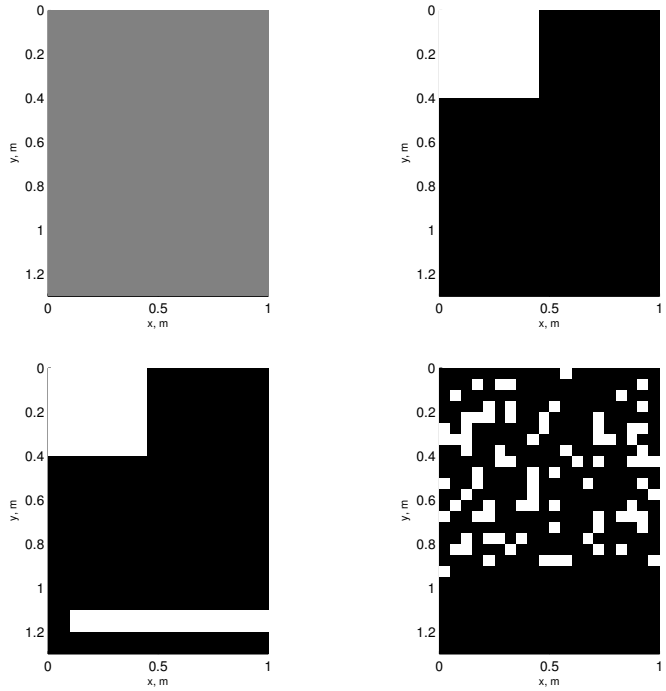

Figure 3.3: Examples of truncating a planar rectangular mesh (top left) to create other shapes (other frames).

analysis, separate calculation of the elements (2.34) is not required as they can be obtained via $R_{mn} = \mathrm{Re}(Z_{mn})$. Here the evaluation of these integrals is laid out for rooftop basis functions and is easily adaptable to RWG basis functions. Examining equations (2.13), (2.33), and (2.32), the following terms can be identified,

$$A_{mn} = k^2 \int_{S_m} \int_{S_n} \vec{\psi}_m(r) \cdot \vec{\psi}_n(r') G_0(r, r') dr' dr \tag{3.6}$$

$$\Phi_{mn} = \int_{S_m} \int_{S_n} \nabla \cdot \vec{\psi}_m(r) \nabla' \cdot \vec{\psi}_n(r') G_0(r, r') dr' dr \tag{3.7}$$

$$X_{em,mn} = -\frac{k}{2}\int_{S_m}\int_{S_n}\left[k^2\vec{\psi}_m(r)\cdot\vec{\psi}_n(r') - \nabla\cdot\vec{\psi}_m(r)\nabla'\cdot\vec{\psi}_n(r')\right]\sin\left(k|r-r'|\right)drdr'. \quad (3.8)$$

Elements of $\mathbf{Z}$, $\mathbf{R}$, $\mathbf{X}$, $\mathbf{X}_m$, and $\mathbf{X}_e$ consist of only these terms,

$$Z_{mn} = \frac{j\eta_0}{4\pi k}\left(A_{mn} + \Phi_{mn}\right) \quad (3.9)$$

$$R_{mn} = \mathrm{Re}\left(Z_{mn}\right) \quad (3.10)$$

$$X_{mn} = \mathrm{Im}\left(Z_{mn}\right) \quad (3.11)$$

$$X_{e,mn} = \frac{\eta_0}{4\pi k}\mathrm{Re}\left(\Phi_{mn}\right) + X_{em,mn} \quad (3.12)$$

$$X_{m,mn} = \frac{\eta_0}{4\pi k}\mathrm{Re}\left(A_{mn}\right) + X_{em,mn}. \quad (3.13)$$

When evaluating the interaction between the m^{th} and n^{th} edge elements, these integrals need only be evaluated over the support of $\vec{\psi}_m$ and $\vec{\psi}_n$. From the piece-wise expressions for $\vec{\psi}$ and $\nabla\cdot\vec{\psi}$ in (3.4) and (3.5) it is clear that both A_{mn} and Φ_{mn} will consist of four contributions from each combination of the S^+ and S^- rectangles from the m^{th} and n^{th} basis function, e.g.,

$$A_{mn} = A_{mn}^{+\tilde{+}} + A_{mn}^{+\tilde{-}} + A_{mn}^{-\tilde{+}} + A_{mn}^{-\tilde{-}}, \quad (3.14)$$

where the superscripts define the component of the m^{th} and n^{th} basis function being used. The choice of $\pm$ rectangle for the n^{th} basis function is denoted with a tilde. This allows for the components of A_{mn}, Φ_{mn}, and $X_{em,mn}$ to be written generally as

$$A_{mn}^{\pm\tilde{\pm}} = k^2\int_{S_m^{\pm}}\vec{\psi}_m^{\pm}(r)\cdot\int_{S_n^{\tilde{\pm}}}\vec{\psi}_n^{\tilde{\pm}}(r')\frac{e^{-jk|r-r'|}}{|r-r'|}dr'dr \quad (3.15)$$

$$\Phi_{mn}^{\pm\tilde{\pm}} = \int_{S_m^{\pm}}\nabla\cdot\vec{\psi}_m^{\pm}\int_{S_n^{\tilde{\pm}}}\nabla'\cdot\vec{\psi}_n^{\tilde{\pm}}\frac{e^{-jk|r-r'|}}{|r-r'|}dr'dr \quad (3.16)$$

$$X_{em,mn}^{\pm\tilde{\pm}} = -\frac{k}{2}\int_{S_m^{\pm}}\int_{S_n^{\tilde{\pm}}}\big[k^2\vec{\psi}_m^{\pm}(r)\cdot\vec{\psi}_n^{\tilde{\pm}}(r') - \nabla\cdot\vec{\psi}_m^{\pm}(r)\nabla'\cdot\vec{\psi}_n^{\tilde{\pm}}(r')\big]\sin\left(k|r-r'|\right)drdr'. \quad (3.17)$$

3.3.1 Quadrature evaluation of non-singular integrals

When $S_m^{\pm}$ does not overlap with $S_n^{\tilde{\pm}}$, the integrals in (3.15), (3.16) and (3.17) can be calculated using Gaussian quadrature by dividing $S_m^{\pm}$ and $S_n^{\tilde{\pm}}$ into K and L subrectangles, respectively. Denoting $\{r_i\}$ and $\{r_j\}$ as the set of subrectangle centers for $S_m^{\pm}$ and $S_n^{\tilde{\pm}}$, respectively, the integrals in (3.15), (3.16) and (3.17) become

$$A_{mn}^{\pm\tilde{\pm}} = k^2\sum_{i=1}^{K}\sum_{j=1}^{L} w_i w_j \vec{\psi}_m^{\pm}(r_i)\cdot\vec{\psi}_n^{\tilde{\pm}}(r_j)\frac{e^{-jk|r_i-r_j|}}{|r_i-r_j|} \quad (3.18)$$

$$\Phi_{mn}^{\pm\tilde{\pm}} = \sum_{i=1}^{K}\sum_{j=1}^{L} w_i w_j \nabla\cdot\vec{\psi}_m^{\pm}(r_i)\nabla\cdot\vec{\psi}_n^{\tilde{\pm}}(r_j)\frac{e^{-jk|r_i-r_j|}}{|r_i-r_j|} \quad (3.19)$$

$$X_{em,mn}^{\pm\tilde{\pm}} = -\frac{k}{2}\sum_{i=1}^{K}\sum_{j=1}^{L} w_i w_j\big[k^2\vec{\psi}_m^{\pm}(r_i)\cdot\vec{\psi}_n^{\tilde{\pm}}(r_j) - \nabla\cdot\vec{\psi}_m^{\pm}(r_i)\nabla\cdot\vec{\psi}_n\tilde{\pm}(r_j)\big]\sin\left(k|r_i-r_j|\right), \quad (3.20)$$

where $\{w_i\}$ are the appropriate weights for a chosen quadrature rule. To ensure matrix operator symmetry, we set $K = L$. This is in contrast to many procedures which set $K = 1$, $L > 1$ [39]. While using $K \neq L$ can provide computational speed up, it inherently breaks the symmetry condition $I_{mn} = I_{nm}$. For many applications, this asymmetry is of minimal consequence. However, when working with eigenvalue problems of matrix operators generated by these numerical methods, matrix symmetry is of the utmost importance as it maintains orthogonality and completeness of eigenmodes [43]. Throughout this dissertation wherever rooftop basis functions are selected, four point equal-area quadrature is used for each of the above non-singular integrals, that is $K = L = 4$ and $w_i = A/4$ (A being the area of the integration domain $S_m^{\pm}$ or $S_n^{\tilde{\pm}}$). Note that elements of $X_{em,mn}$ are always non-singular and

as such can always be calculated using the above quadrature technique.

3.3.2 Duffy integration for singular components

When $S_m^{\pm}$ overlaps with $S_n^{\bar{\pm}}$, the Green's function in $A_{mn}^{\pm\bar{\pm}}$ and $\Phi_{mn}^{\pm\bar{\pm}}$ becomes singular and must be treated with care. Here a Duffy transform technique [44] is used to evaluate the singular integral when $S_m^{\pm} = S_n^{\bar{\pm}}$. This rectangle will be denoted as S. The singular integrals then take the form

$$I = \int_S \int_S f(r)g(r')G_0(r, r')dsds', \tag{3.21}$$

where f and g are non-singular. To deal with the singularity at $r = r'$ in the free-space Green's function, G_0, the integrating rectangle is divided into four equal area subrectangles (the same as used in the non-singular 4×4 quadrature), i.e.,

$$I = \frac{A_S^2}{16} \sum_{i=1}^{4} \sum_{j=1}^{4} f(r_i)g(r_j)G_0(r_i, r_j). \tag{3.22}$$

In this form, issues only arise in the terms where $i = j$. These need to be integrated differently. Separating these the singular terms gives

$$I = \frac{A_S^2}{16} \left(\sum_{i=1}^{4} \sum_{j \neq i} f(r_i)g(r_j)G_0(r_i, r_j) + \frac{4}{A_S} \sum_k f(r_k)g(r_k)I_k \right), \tag{3.23}$$

where

$$I_k = \int_{S_k} G_0(r_k, r')ds'. \tag{3.24}$$

This can be evaluated by dividing S_k into four subtriangles $t_{k,p}$, each with a vertex at two bounding corners of S_k ($\mathbf{r}_1$ and $\mathbf{r}_2$) and its center, r_k. Equation (3.24) then becomes

$$I_k = \sum_{p=1}^{4} \int_{t_{k,p}} G_0(r_k, r')ds'. \tag{3.25}$$

Now each subintegration over $t_{k,p}$ has a singularity located at the vertex r_k. Using the Duffy transform the singularity can be removed via

$$I_k = \sum_{p=1}^{4} 2A_t \int_{u_1} \int_{u_2} u_1 G(r_k, r(u_1, u_2)) du_1 du_2 \tag{3.26}$$

with

$$A_t = |(\mathbf{r}_1 - \mathbf{r}_k) \times (\mathbf{r}_2 - \mathbf{r}_k)| \tag{3.27a}$$

$$r(u_1, u_2) = u_1(1 - u_2)\mathbf{r}_1 + u_1 u_2 \mathbf{r}_2 + (1 - u_1)\mathbf{r}_k. \tag{3.27b}$$

In the above equations, $\mathbf{r}_1$, $\mathbf{r}_2$, and $\mathbf{r}_k$ are the same as r_1, r_2, and r_k in (3.26) with bold notation to explicitly show their vector properties. The integral in (3.26) must, in general, be evaluated using adaptive quadrature in order to ensure good removal of the singularity. However, because the Green's function and integration domain are usually the same (here we assume uniform area rectangular basis functions) in each evaluation of (3.26), it suffices to study the convergence of I_k with respect to domain size and quadrature order. For basis function domain size on the order of $\lambda/12$, the integration area in (3.26) is a triangle with side length on the order of $\lambda/25$. With this size of integration area and using a two-dimensional Gaussian quadrature rule [45] in u_1, u_2 space, nine integration points ($m = 3$ quadrature) was observed to be sufficient for evaluation of (3.26). This mesh size is therefore used as a guideline with $m = 3$ quadrature used throughout. Similar convergence can be studied for RWG basis functions.

3.4 Eigenvalue tracking

In order to examine the behavior of any modal solutions (e.g., characteristic modes, radiation modes) as functions of frequency, care must be taken in order to properly sort and track individual modes between discrete frequency points where the method of moments calculations are performed. One can think of the the eigenvalue problem in (2.47) with $\mathbf{L} = \mathbf{R}$ as a single instance of a problem involving a parameterized matrix. In this case, the parameter is frequency, ω. This dependence can be written explicitly as

$$[\mathbf{RJ} = \nu \mathbf{PJ}]_\omega \,. \tag{3.28}$$

Using an eigenvalue solver at each ω gives eigenvector / eigenvalue pairs sorted according to some scheme. For example, the MATLAB functions `eigs` or `eig` [46] sort based on eigenvalue magnitude. Problems arise when, in neighboring frequency steps, eigenvectors exchange rank in the sorting scheme. Using `eigs` or any other sorted-output routine, this occurs when eigenvalues or their absolute values cross. If the goal is to track how a single modal current distribution changes over frequency it is necessary to adopt some eigenmode tracking procedure to maintain continuity through these crossings. This problem is well-documented in the characteristic mode literature, where it is also prevalent. Procedures using matrix integration [47], orthogonality of modes [48], correlation matrices [49], far-field patterns [50], and Pearson correlations [51] have all been reported with mixed success. All of these methods, in some way or another, depend on closely-spaced values of ω to provide satisfactory results. Here we follow an equivalent method as presented in [48], but tailored for radiation and energy storage modes. We start by making assuming the frequency step $\Delta\omega$ is small enough that the current distribution of a given mode changes very little in each step, allowing the approximation

$$(\mathbf{J}_i(\omega + \Delta\omega))^T \mathbf{P} \mathbf{J}_j(\omega) \approx \delta_{ij} \tag{3.29}$$

based on (2.48). To track a single modal current distribution, a mode is selected from the output of an eigenvalue solver at some starting frequency. We denote the eigenvector of this mode as $\mathbf{x}_n$ and its eigenvalue as λ_n. At the next frequency, K eigenvectors are obtained using the same solver. These eigenvectors are written $\{\mathbf{y}_k\}$ and are assembled as columns in $\mathbf{Y}$. All vectors are normalized as in (2.48). The orthogonality relation in (3.29) can be used to form a vector containing errors between $\mathbf{x}_n$ and $\{\mathbf{y}_k\}$

$$\boldsymbol{\epsilon} = \begin{bmatrix} \epsilon_1 \\ \vdots \\ \epsilon_K \end{bmatrix} = (1 - |\mathbf{Y}^T \mathbf{P} \mathbf{x}_n|)^2. \tag{3.30}$$

Finding the minimum ϵ_k gives the index of the mode in $\{\mathbf{y}_k\}$ corresponding to $\mathbf{x}_n$. An upper threshold should be set on acceptable ϵ to stop tracking when the mode being tracked is no longer present in the K eigenvectors obtained from `eigs`. Repeating this orthogonality check procedure gives

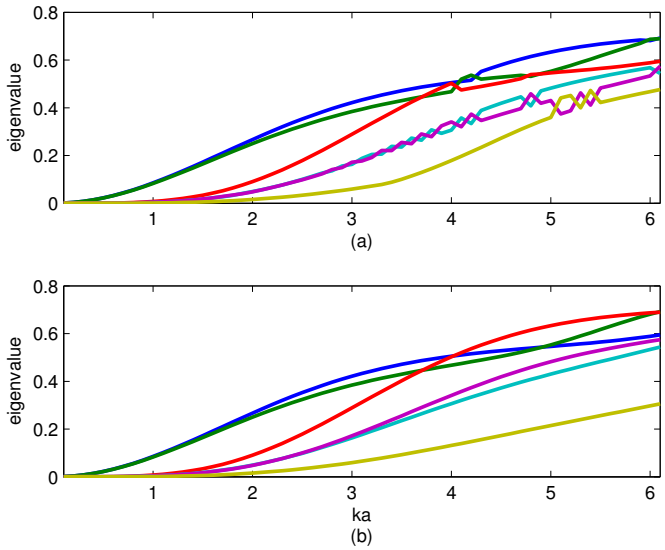

Figure 3.4: Unsorted (a) and sorted (b) radiation modes of a rectangular plate (aspect ratio 1.3) over a range of frequencies $0.1 < ka < 6$.

continuous tracking of a current distribution and its eigenvalue as it changes with frequency. Figure 3.4 compares the unsorted and sorted eigenvalues of radiation modes from a small rectangular plate (aspect ratio 1.3) over a broad range of frequencies.

This method has proven robust in situations where eigenvalue crossings and avoidances are ambiguous, as discussed in the context of characteristic modes in [35]. However, this technique is not well suited to discerning individual eigenmodes when many elements of the eigenspectra have nearly equal eigenvalues over broad frequency ranges, as is frequently encountered in energy storage analysis. This is discussed further in Chapter 6.

CHAPTER 4

ANALYSIS EXAMPLES

4.1 Overview

Radiation and energy storage modal analyses are demonstrated on two example antenna types. The formulation in Chapter 2 for these eigenvalue problems is implemented using numerical results from the methods developed in Chapter 3. Decomposition of a current into radiating and non-radiating components is demonstrated using radiation mode expansion. Numerical results show that energy storage mode expansion does not allow for such a separation. Radiation modes are demonstrated to be relatively invariant to small geometry changes.

4.2 Problems studied

The two examples studied here using radiation and energy storage modal expansions are a simple dipole and an antenna designed for digital television signals (DTV) mounted to a tablet-sized L-shaped ground plane. The dipole example is intended to ground the results obtained from these analyses in a well-known, well-understood example. We examine results from the dipole over a broad range of frequencies in order to gain some insight into the general behavior of radiation and energy storage modes on this canonical structure. The DTV antenna is a more complex example and is examined in detail only at its design frequency. It represents an embedded antenna; i.e., an small driven antenna element mounted to a larger conducting ground structure. Antennas of this type are often designed by rote optimization of heuristic topologies due to the complex interaction between the designed antenna element and the finite ground plane. This example shows how radia-

tion and energy storage modal analysis can inform and quantify some of these interactions in novel ways. Analysis of both examples originally appeared in [37].

4.2.1 Dipole antenna

A thin strip dipole with length-to-width ratio of $L/w = 500$ is simulated over the frequency range $l = \lambda/30$ to $l = \lambda$. Over all frequencies, 200 uniform rectangular mesh subdomains are used to represent the surface. Feeding is implemented using delta-gap excitation at the center of the dipole.

4.2.2 Tablet-sized DTV antenna

An antenna designed for digital television (DTV) signals is simulated within its operating band at 569 MHz. The antenna geometry is represented by uniform rectangular basis functions with subdomain size on the order of $\lambda/100$. The geometry consists of two main components: an L-shaped ground plane and a bent monopole antenna element. The bent monopole measures 0.171λ and the entire structure is bounded by a $0.342\lambda \times 0.262\lambda$ rectangle. Feeding is implemented by a delta-gap source located at the base of the antenna element. The system is shown in Figure 4.1, with the feed location drawn in blue with an orange arrow indicating the feed field orientation.

4.3 Radiation mode analysis

4.3.1 Separation of $\mathbf{J}_r$ and $\mathbf{J}_{nr}$

The radiation mode expansion of the thin strip dipole is presented first. The inversion problem in (2.15) is solved to obtain the driven current $\mathbf{J}$. Note that this inversion and subsequent manipulations of currents, matrices, and expansions are implicitly done at each frequency in the simulated band. The radiation modes of the dipole are found by solving (2.47) with $\mathbf{L} = \mathbf{R}$, i.e.,

$$\mathbf{RJ} = \nu\mathbf{PJ}. \tag{4.1}$$

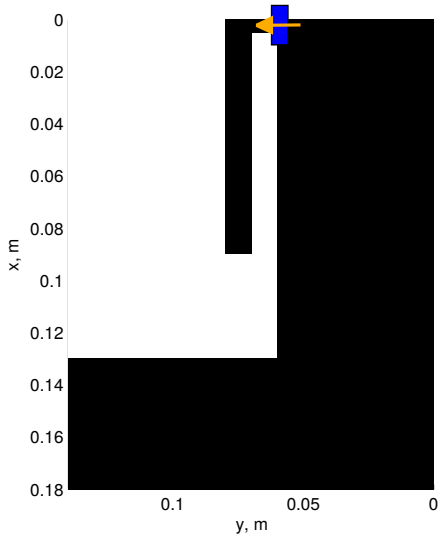

Figure 4.1: DTV antenna system geometry. The bounding rectangle of the system measures $0.342\lambda \times 0.262\lambda$ and the monopole length is 0.171λ at 569 MHz. The delta-gap feed location is shown in blue, with the field orientation of the feed indicated by an orange arrow.

Once the modes are found, the excitation coefficients are calculated via (2.50). Modal radiated powers are then given by (2.51). For clarity, all total current distributions (e.g., the driven current $\mathbf{J}$) are normalized to radiate unit power. The radiation mode eigenvalues, excitation coefficients, and modal powers for the center-driven thin strip dipole are shown at $l = \lambda/30, \lambda/3$, and λ in Figures 4.2, 4.3, and 4.4, respectively.

From these calculations, several points are apparent. First, only a few radiation modes at each frequency have non-trivial eigenvalues. Second, at each frequency many radiation modes are present in the total driven current distributions. Finally, across all frequencies only the lowest-order mode ($n = 1$) contributes to radiation, i.e., $p^1_{rad} \approx 1$ or equivalently using the notation of (2.58), $K = \{1\}$. Furthermore, this implies that across all frequencies examined here, $\mathbf{J}_r \approx \alpha_1 \mathbf{J}_1$ and $\mathbf{J}_{nr} \approx \mathbf{J} - \alpha_1 \mathbf{J}_1$. Using these relations, the driven current and its radiating and non-radiating components are plotted at $l = \lambda/30, \lambda/3$, and λ in Figure 4.5. There we observe that at each frequency, radiation is due to the uniform component of the total driven current. The non-radiating component, consisting of radiation modes with small eigenvalues and/or small excitation coefficients, appear to enforce the boundary

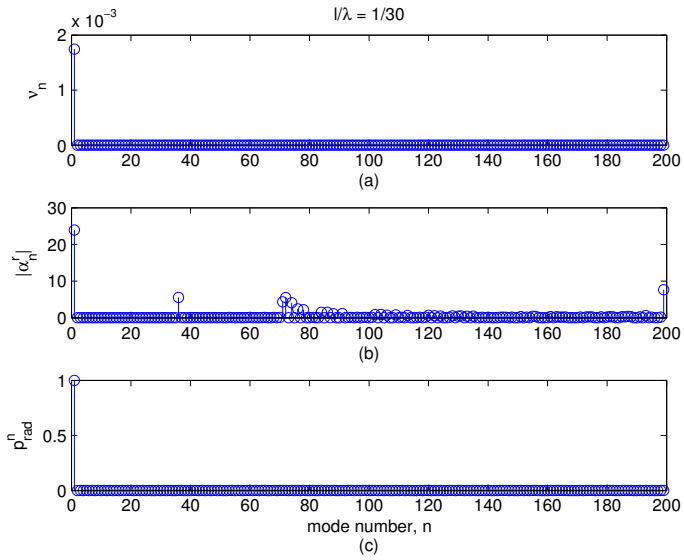

Figure 4.2: Radiation eigenvalues (top), excitation coefficients (middle) and modal powers (bottom) obtained by radiation mode expansion of the driven current on a thin-strip dipole at $l/\lambda = 1/30$.

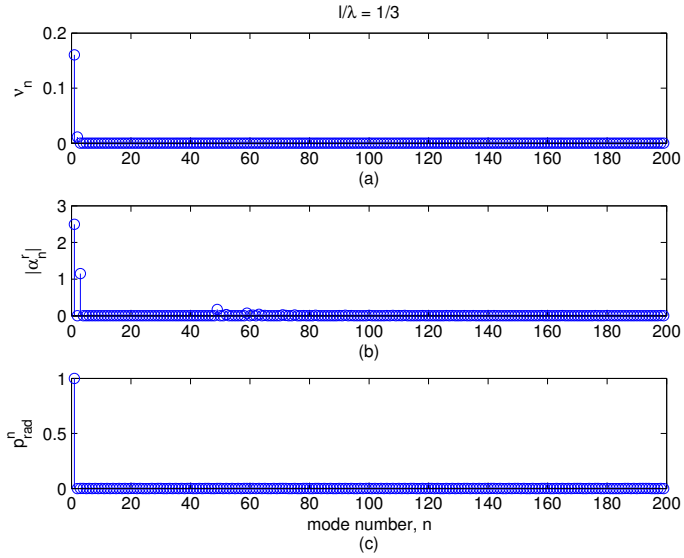

Figure 4.3: Radiation eigenvalues (top), excitation coefficients (middle) and modal powers (bottom) obtained by radiation mode expansion of the driven current on a thin-strip dipole at $l/\lambda = 1/3$.

conditions at the end of the dipole while not significantly contributing to the radiated power.

Using the same methodology, the DTV system is analyzed at its design

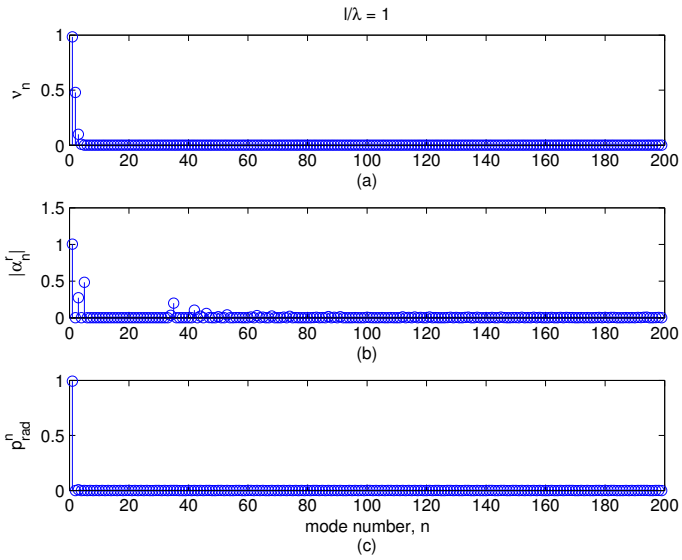

Figure 4.4: Radiation eigenvalues (top), excitation coefficients (middle) and modal powers (bottom) obtained by radiation mode expansion of the driven current on a thin-strip dipole at $l/\lambda = 1$.

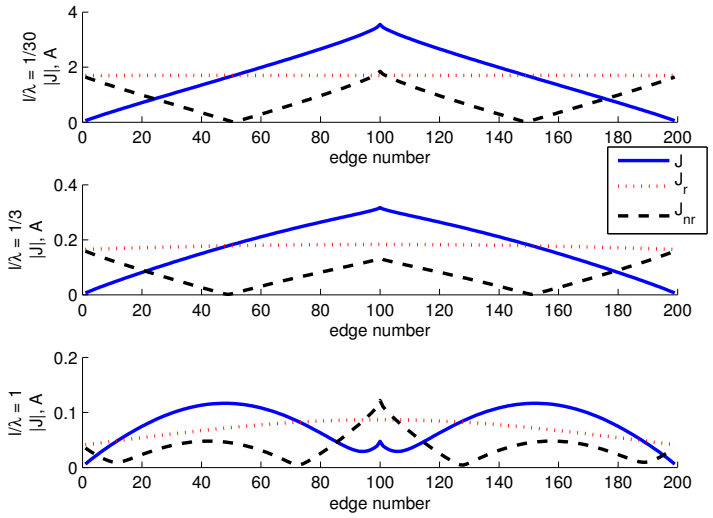

Figure 4.5: Driven current (solid) and its radiating (dotted) and non-radiating (dashed) components on a thin strip dipole at $l/\lambda = 1/30$ (top), 1/3 (middle), and 1 (bottom).

frequency of 569 MHz. The total driven current is shown in Figure 4.6. The current maximum is near the feed location while lower amplitude currents exist over the support of the ground plane. Calculating the radiation modes

of this structure we can obtain the modal eigenvalues, excitation coefficients, and modal powers, shown in Figure 4.7

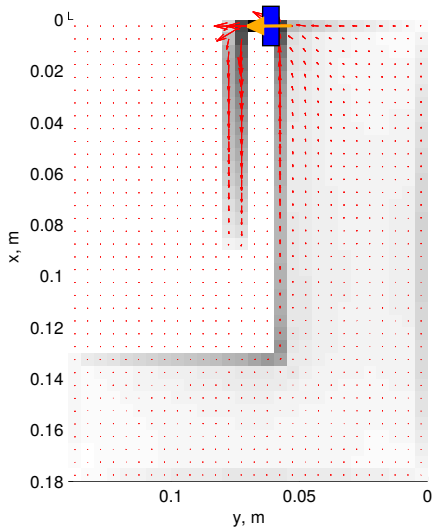

Figure 4.6: Total driven current at 569 MHz. The delta-gap feed location is shown in blue, with the field orientation of the feed indicated by an orange arrow.

These results show similar characteristics as those observed in the dipole data. It is observed that only a few radiation modes have non-trivial eigenvalues. While there are many radiation modes present in the total current, the inclusion of ν in the expression for modal powers effectively masks out all radiation modes except for those with significant eigenvalues. This is seen in the bottom pane of Figure 4.7, where it is clear that only the first three radiation modes contribute significantly to the system's radiation, accounting for 99.3% of the total power radiated. Of those three modes, the $n = 1$ mode is the most dominant, contributing 86% of the radiated power. Using this result, we can set $K = \{1, 2, 3\}$ and calculate the radiating and non-radiating components of the driven current according to (2.59) and (2.60). The three dominant radiation modes are displayed in Figures 4.8-4.10 while the radiating and non-radiating current components are shown in Figures 4.11 and 4.12. Similar to the dominant radiation mode in the dipole example, the main radiation mechanisms on this structure, $\mathbf{J}_1$ and $\mathbf{J}_2$, appear to be uniform current distributions across the support of the object differing only in their orientation. These two modes also have similar eigenvalues, as seen in

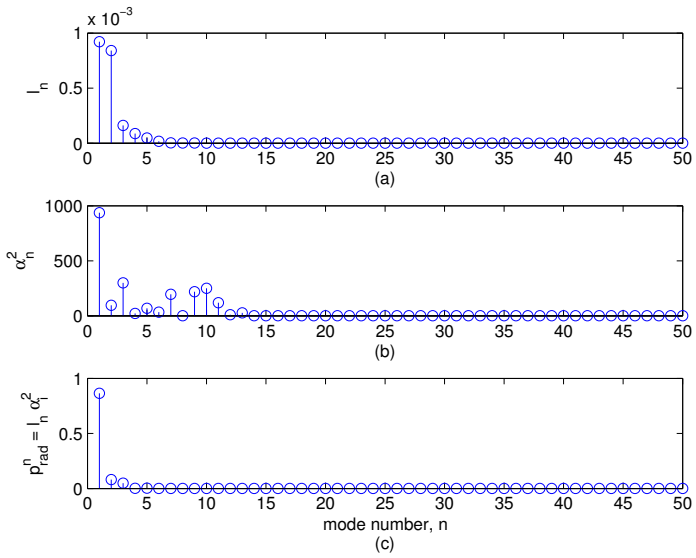

Figure 4.7: Radiation eigenvalues (top), excitation coefficients (middle) and modal powers (bottom) obtained by radiation mode expansion of the driven current on the DTV antenna system at 569 MHz.

Figure 4.7. The third radiation mode, $\mathbf{J}_3$, has spatial variation resembling a loop and a significantly lower eigenvalue than the uniform modes. These two classes of modes are found on every planar object of this electrical size and typically constitute the main sources of radiation. The forms of these types of modes are studied in more detail in Chapter 5.

4.3.2 Radiation mode contributions to radiation patterns

The radiation pattern due to a current distribution $\vec{J}$ can be written in the following operator forms

$$\vec{E}_\gamma(\theta,\phi) = F_\gamma\left(\vec{J}\right)(\theta,\phi) = \int_{S'} \hat{\gamma}\cdot\vec{J}(\mathbf{r}')e^{-jk|\mathbf{r}-\mathbf{r}'|}ds', \tag{4.2}$$

where γ represents the choice of θ or ϕ polarization and $\vec{E}_\gamma(\theta,\phi)$ is the far-zone electric field at the angle (θ,ϕ). Some constants are omitted for clarity. Note that $\mathbf{r}$ is located on an infinite sphere. These operators are linear and can easily be discretized as

$$\mathbf{E}_\gamma = \mathbf{F}_\gamma\mathbf{J}. \tag{4.3}$$

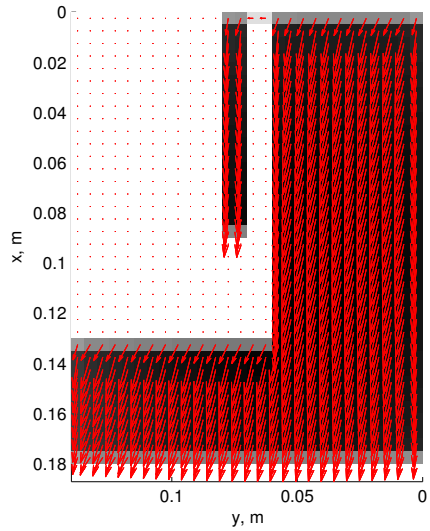

Figure 4.8: First radiation mode $\mathbf{J}_1$, $p^1_{rad} = 86.4\% P_{rad}$.

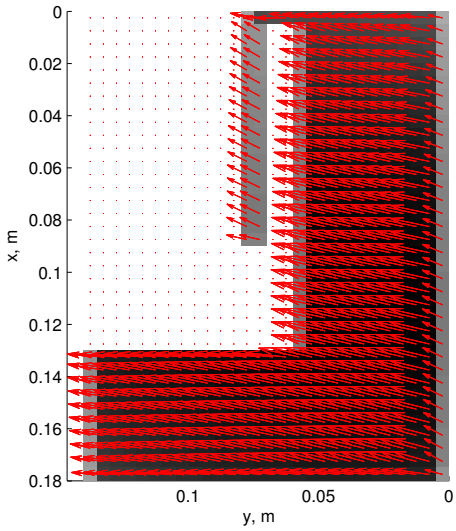

Figure 4.9: Second radiation mode $\mathbf{J}_2$, $p^1_{rad} = 8.08\% P_{rad}$.

The linear nature of F_γ further leads to an expression of the far-field in terms of the patterns due to weighted sums of current distibutions, i.e.,

$$\mathbf{E}_\gamma = \mathbf{F}_\gamma \sum_n^N \alpha_n \mathbf{J}_n = \sum_n^N \alpha_n \mathbf{F}_\gamma \mathbf{J}_n. \tag{4.4}$$

In the antenna literature, far-field radiation patterns are typically reported

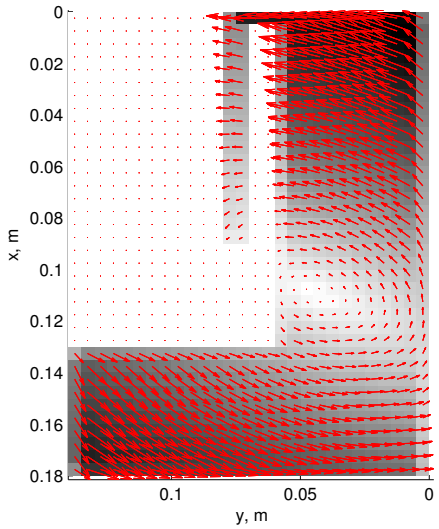

Figure 4.10: Third radiation mode $\mathbf{J}_3$, $p^1_{rad} = 4.82\% P_{rad}$.

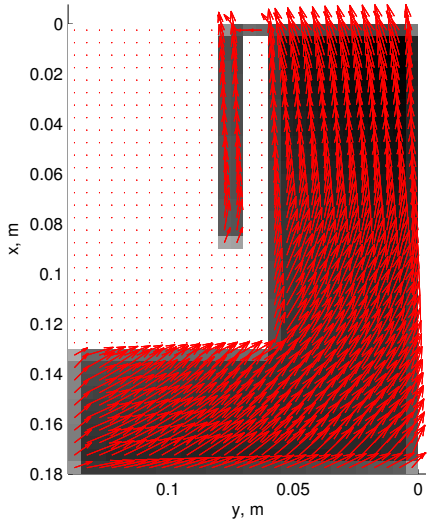

Figure 4.11: Radiating component of the driven current in Figure 4.6.

in terms of radiated power of one or both polarizations. For a single polarization, we denote this power

$$\mathbf{g}_\gamma = \mathbf{E}_\gamma \circ \mathbf{E}_\gamma, \tag{4.5}$$

where $\circ$ is the Hadamard product. For the total power pattern we use

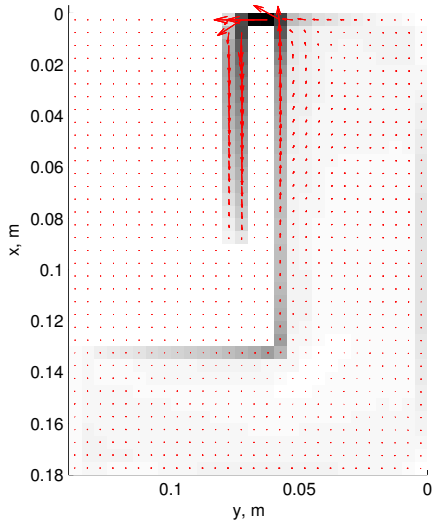

Figure 4.12: Non-radiating component of the driven current in Figure 4.6.

$$\mathbf{g} = \mathbf{E} \circ \mathbf{E}, \tag{4.6}$$

where

$$\mathbf{E} = \sqrt{\mathbf{E}_\theta \circ \mathbf{E}_\theta + \mathbf{E}_\phi \circ \mathbf{E}_\phi}. \tag{4.7}$$

Clearly, the power patterns of one or both polarizations is non-linear and cannot be written in the sum form given in (4.4). However, owing to the properties of radiation modes and their orthogonality in $\mathbf{R}$, the total power radiated by a set of radiation modes is the sum of the individual modal powers. Therefore, while the power patterns $\mathbf{g}_\gamma$ and $\mathbf{g}$ behave non-linearly in their appropriating of the radiated power to the far-field, the total power present in the far-field due to a collection of radiation modes will be the sum of the powers present in the modal far-fields.

We now test the following concept using radiation modes: currents which do not radiate do not affect far-field radiation. In the Section 4.3.1, the radiating component of the driven current distribution on a DTV antenna system was identified. The radiating component, $\mathbf{J}_r$, consisted of a weighted set of three radiation modes. The power radiation patterns $\mathbf{g}_\gamma$ for these three current modes are shown individually in Figure 4.13.

Summed and properly weighted, these three current modes account for 99.3%

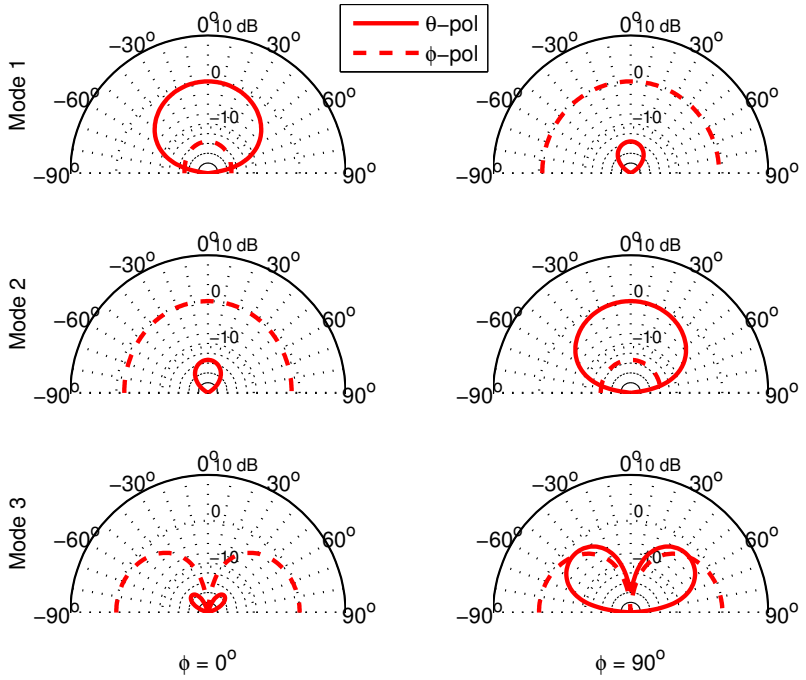

Figure 4.13: Radiation patterns of the three dominant radiation modes on the DTV antenna system.

of the radiated power by the system. Thus we expect that the radiation pattern of the system is due only to the sum of these three modes as well. Figure 4.14 shows partial weighted sums of the dominant radiation modes as well as the radiation pattern of the total current. The pattern due to the sum of modes 1, 2, and 3 is nearly identical to that of the total current distribution. Hence we have demonstrated that $\mathbf{J}_r$ not only accounts for nearly all of the radiated power of the system, but it also determines the radiation pattern of the driven current. Conversely, the non-radiating modes present in the total current distribution do not contribute to the radiation pattern.

4.3.3 Comparison to characteristic mode analysis

The novelty of the radiation mode expansion technique demonstrated here is the ability to identify the radiating and non-radiating components of an arbitrary current distribution. In short, this is accomplished by identifying

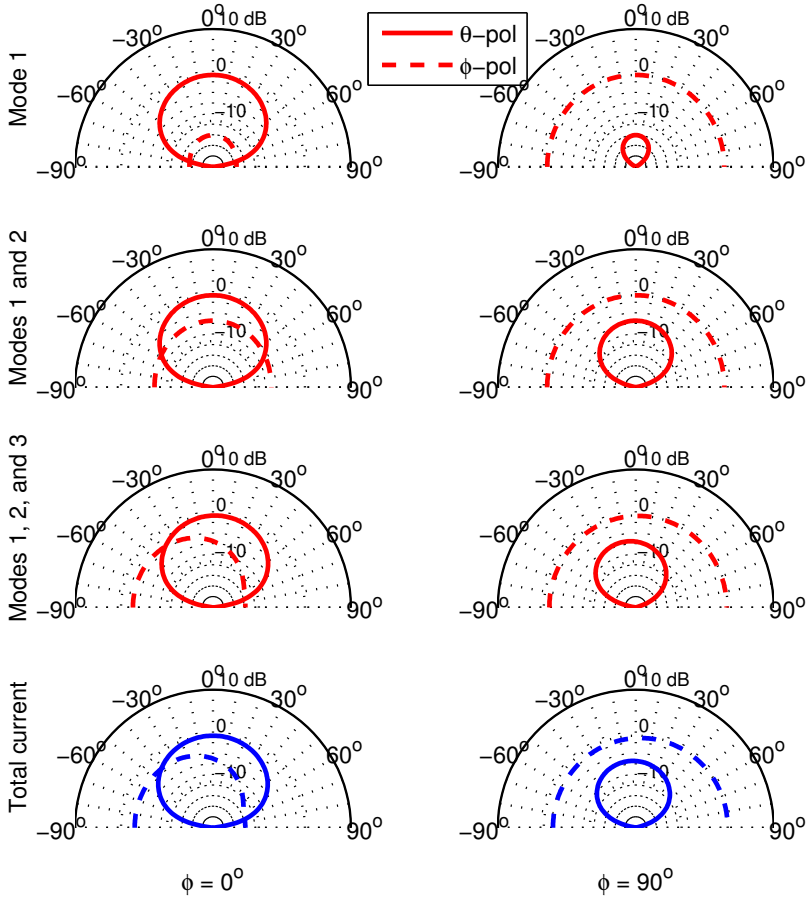

Figure 4.14: Patterns of partial sums of weighted radiation mode currents. The third and fourth rows of patterns are those of $\mathbf{J}_r$ and $\mathbf{J}$, respectively.

the set of radiation modes contributing to the total power output. A similar procedure is commonly applied using characteristic modes. In this section the two techniques are compared, highlighting some of the advantages of radiation mode analysis in identifying radiation mechanisms. Characteristic modes are solution to the eigenvalue problem

$$\mathbf{XJ} = \lambda \mathbf{RJ}, \tag{4.8}$$

where $\mathbf{R}$ and $\mathbf{X}$ are the real and imaginary parts, respectively, of the impedance matrix $\mathbf{Z}$ [7, 8]. For clarity, quantities associated with characteristic modes will be labeled ^{cm}. By the assumed symmetry of $\mathbf{R}$ and $\mathbf{X}$, the modal solu-

tions $\{\mathbf{J}_n^{cm}\}$ can be normalized in the following ways,

$$\mathbf{J}_i^{cm,T}\mathbf{R}\mathbf{J}_j^{cm} = \delta_{ij} \tag{4.9}$$

$$\mathbf{J}_i^{cm,T}\mathbf{X}\mathbf{J}_j^{cm} = \lambda_i\delta_{ij}. \tag{4.10}$$

Any current on the object described by $\mathbf{Z}$ can be expanded into characteristic modes via

$$\mathbf{J} = \sum_n^N \beta_n \mathbf{J}^{cm}, \tag{4.11}$$

where the expansion coefficients are commonly written in terms of the current's driving voltage, $\mathbf{V}$, as,

$$\beta_n = \frac{\mathbf{V}^T\mathbf{J}_n^{cm}}{1 + j\lambda_n}. \tag{4.12}$$

Using these expressions, the modal contributions to radiation and energy storage are written

$$P_{rad} = \sum_n^N |\beta_n|^2 \tag{4.13}$$

$$2\omega\left(W_m - W_e\right) = \sum_n^N \lambda_n|\beta_n|^2. \tag{4.14}$$

Note that, because $\mathbf{X}_e$ and $\mathbf{X}_m$ were not used, only the reactive energy difference of characteristic modes can be studied. Comparing the radiation mode and characteristic mode contributions to the total power in (2.51) and (4.13) we see an important distinction: radiation modal powers are proportional to both the modal eigenvalue ν and the excitation coefficient α. This allows for radiation modes to be present (large α) while not radiating (small ν). Clearly this is not the case for characteristic modes, where the modal power contributions depend solely on β. Thus, all characteristic modes radiate according to their excitation. Attempting to form constructions analogous to (2.59) and (2.60) is therefore much more difficult using characteristic modes, especially since characteristic modes include high-magnitude non-radiating currents on low-order modes. This highlights the utility and uniqueness of

radiation mode expansion in its ability to separate the radiating and non-radiating components of a current distribution. Intuition and physical understanding regarding systems with small, reactive antenna elements mounted to finite ground planes (such as the DTV antenna described in Section 4.2.2) are greatly enhanced by the process of separating the high-magnitude, non-radiating currents from the low-amplitude radiating mechanisms.

4.4 Energy storage analysis

Examining energy storage mechanisms using the eigenmodes of $\mathbf{X}_m$ and $\mathbf{X}_e$ follows the same procedure used with $\mathbf{R}$ to investigate radiation. Here we cover the results of energy storage analysis of the dipole and DTV antenna examples. Of particular interest is the vastly different nature of the data obtained from energy storage analysis compared with those calculated by radiation mode expansion.

The electric energy storage modal expansion is performed on the thin strip dipole at the same frequencies used in the radiation mode analysis. The eigenvalues, expansion coefficients, and modal electric energies for these three frequencies are shown in Figures 4.15-4.17. Several features distinguish this expansion from the radiation mode analysis. First, the entire eigenspectrum is non-trivial. This alone indicates that the masking effect exploited to isolate the radiating currents in the previous section may not apply to the energy storage operators. Second, we note that only a few capacitive modes are required to synthesize the total current distribution. This is in contrast to the radiation mode expansion where many modes were required. Because of the fully populated eigenspectrum, the excitation coefficients correspond more or less directly to the modal stored energy quantities. In light of this, the electric energy mode expansion allows for the identification of a sparse set of capacitive current mechanisms while not allowing for the separation of capacitive and non-capacitive components as was done in the radiation problem. Though the eigenspectrum of $\mathbf{X}_m$ shows a slightly different character, the inductive mode expansion shares many of the features seen in the electric energy problem. The eigenspectrum, expansion coefficients, and modal energies from the magnetic energy expansion of the three dipole calculations are shown in Figures 4.18-4.20.

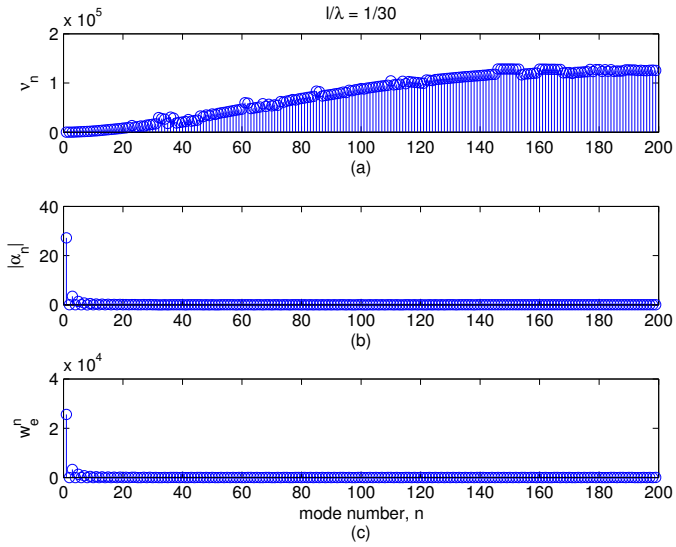

Figure 4.15: Electric energy eigenvalues (top), excitation coefficients (middle) and modal powers (bottom) obtained by electric energy mode expansion of the driven current on a thin-strip dipole at $l/\lambda = 1/30$.

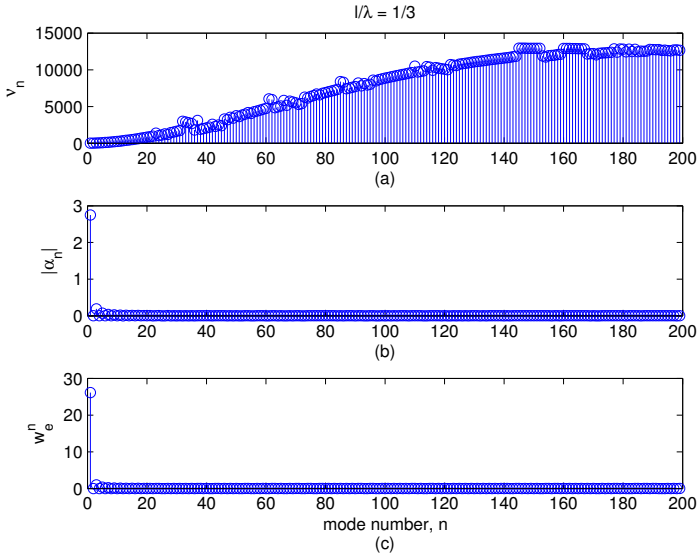

Figure 4.16: Electric energy eigenvalues (top), excitation coefficients (middle) and modal powers (bottom) obtained by electric energy mode expansion of the driven current on a thin-strip dipole at $l/\lambda = 1/3$.

We also apply the electric and magnetic energy storage expansion to the DTV antenna example. There we see the same trends as observed in the analysis of the thin strip dipole. However, the added complexity of the

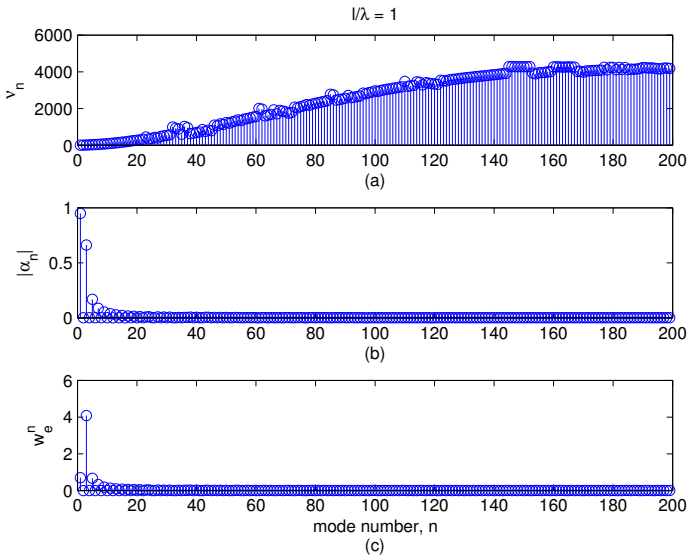

Figure 4.17: Electric energy eigenvalues (top), excitation coefficients (middle) and modal powers (bottom) obtained by electric energy mode expansion of the driven current on a thin-strip dipole at $l/\lambda = 1$.

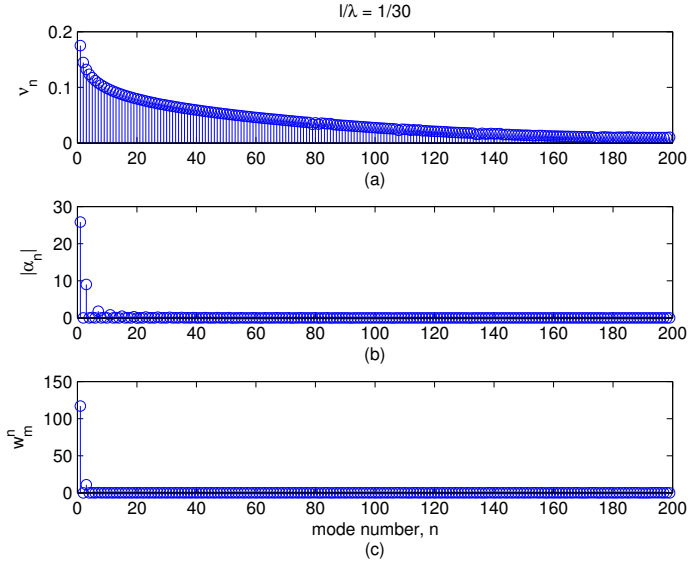

Figure 4.18: Magnetic energy eigenvalues (top), excitation coefficients (middle) and modal powers (bottom) obtained by magnetic energy mode expansion of the driven current on a thin-strip dipole at $l/\lambda = 1/30$.

DTV antenna system results in some interesting effects. Two of the prevailing capacitive modes are shown in Figures 4.21 and 4.22. Each of these modes contributes a significant amount of the stored electric energy in the

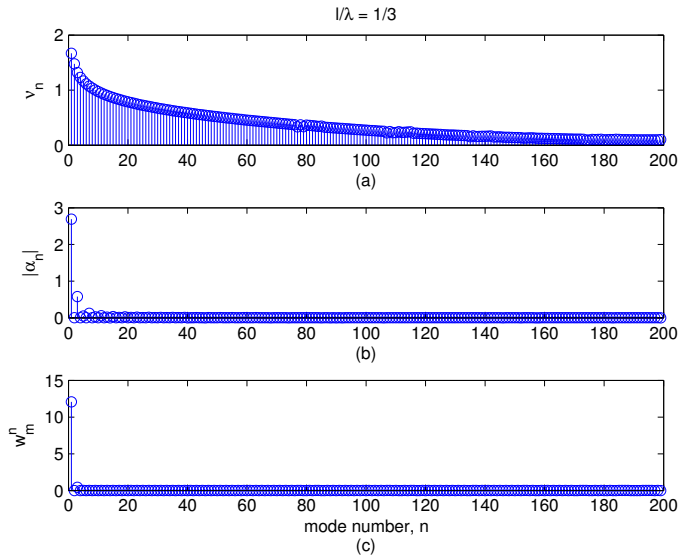

Figure 4.19: Magnetic energy eigenvalues (top), excitation coefficients (middle) and modal powers (bottom) obtained by magnetic energy mode expansion of the driven current on a thin-strip dipole at $l/\lambda = 1/3$.

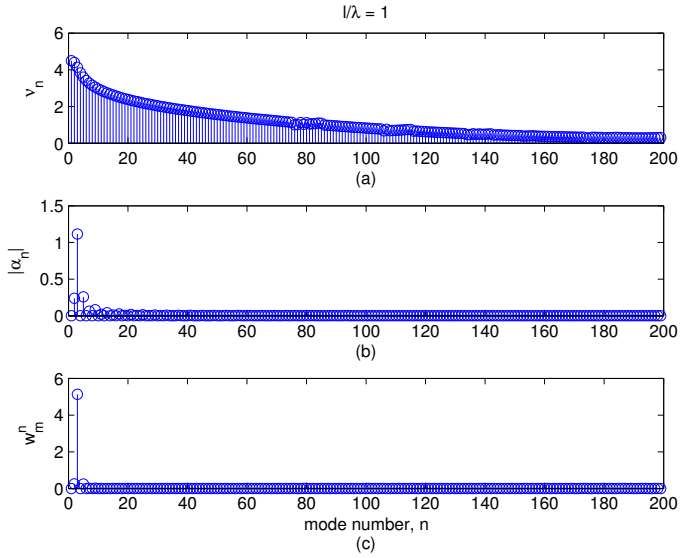

Figure 4.20: Magnetic energy eigenvalues (top), excitation coefficients (middle) and modal powers (bottom) obtained by magnetic energy mode expansion of the driven current on a thin-strip dipole at $l/\lambda = 1$.

system, though each can be roughly defined as existing primarily on the ground plane or on the driven antenna element. While summing all of the capacitive (or inductive) modes to separate the current into contributing

and non-contributing components is less effective here than in the radiation problem, there is still information to be gained by examining the distinct energy-storing current mechanisms which are excited on this structure. The fact that in both the electric and magnetic energy problems there exist modes whose support is one substructure or the other corroborates the intuition that a small antenna element can act as a non-radiating matching network which couples power from the feed to the radiating ground plane. The classification used here in deeming a mode either ground-plane- or element-localized is done by visual inspection and in future work a more robust criterion should be established. For now, however, we can examine the contributions to radiated power and stored energies on an approximate level using the results from the previous modal expansions. Contributions to these quantities are shown in Figure 4.23. Note that modes which weren't easily classified are labelled "mixed".

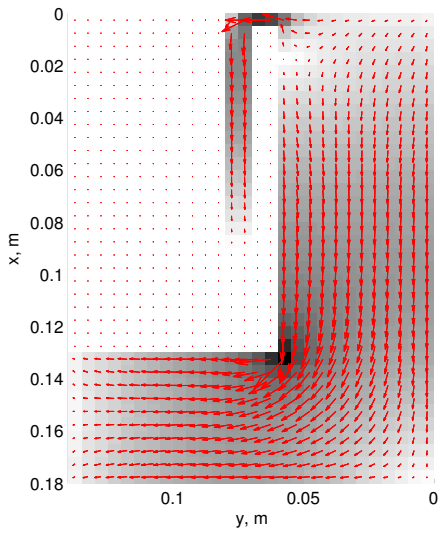

Figure 4.21: Capacitive mode accounting for 56.3% of the stored electric energy due to the driven current in Figure 4.6. While currents appear on both the ground plane and the antenna element, the high-magnitude ground plane currents are the key distinguishing feature of this mode, contrasted for example with the driven current.

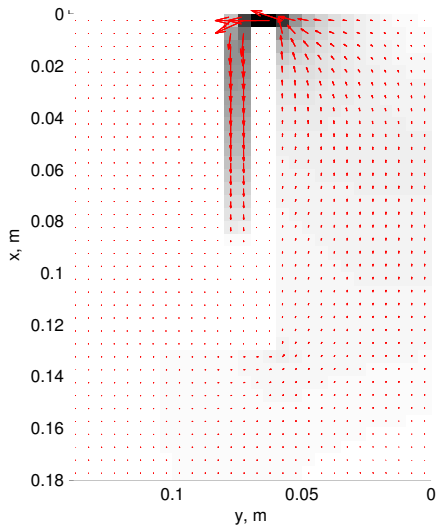

Figure 4.22: Capacitive mode accounting for 39.0% of the stored electric energy due to the driven current in Figure 4.6. Most of the currents in this mode are confined to the driven element.

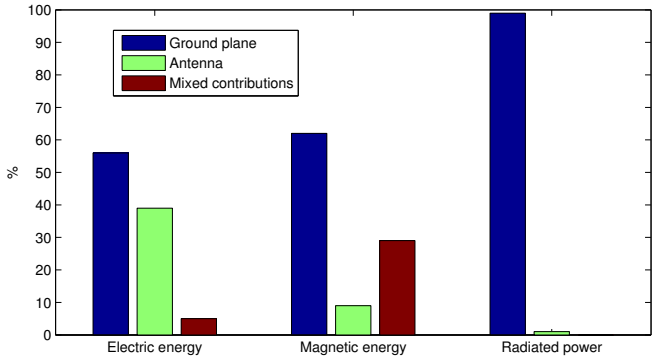

Figure 4.23: Estimated substructure contributions to radiation and energy storage.

4.5 Effect of antenna element on radiation modes

In this section, the effect of the antenna element on the radiation modes of the DTV system's ground plane are examined. Because the dominant radiation mode in this example are very simple in their structure, we hypothesize that the eigenmodes of the radiation matrix are tolerant to changes in geometry. To test this, the bent monopole element is removed from the DTV antenna system. The radiation modes of this ground-plane-only geometry are

calculated then in the usual manner. The eigenvalues of the dominant radiation modes are compared to the original, full DTV antenna system in Table 4.1. The current distributions associated with these modes are also shown in Figures 4.24-4.26. The difference in eigenvalues is small, less than 6% for all three modes. Further, the modal current distributions appear relatively unchanged by the removal of the antenna element. This is important as it suggests that the radiation modes (and hence available mechanisms governing radiated power, far-field patterns, and polarization) of a finite ground plane can be analyzed and understood before the design of a mounted antenna. In addition, these results imply that there exist a common set of modes for planar objects, relatively independent of geometry. This is explored analytically in Chapter 5.

Table 4.1: Radiation mode eigenvalues for a ground plane with and without an attached monopole element

	Ground plane	Ground plane and monopole	Δ
l_1	8.73 x 10^{-4}	9.22 x 10^{-4}	5.6 %
l_2	8.12 x 10^{-4}	8.42 x 10^{-4}	3.6 %
l_3	1.53 x 10^{-4}	1.61 x 10^{-4}	4.5 %

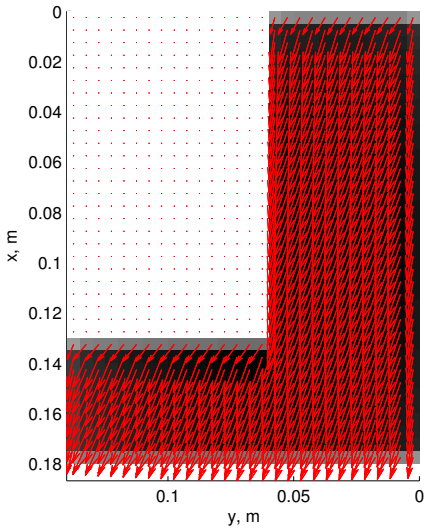

Figure 4.24: First radiation mode of the DTV antenna system with the antenna element removed.

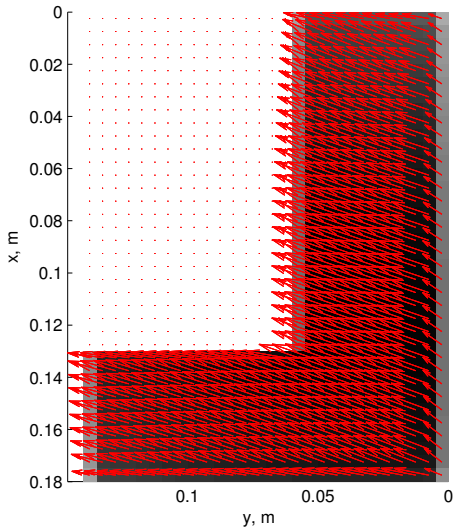

Figure 4.25: Second radiation mode of the DTV antenna system with the antenna element removed.

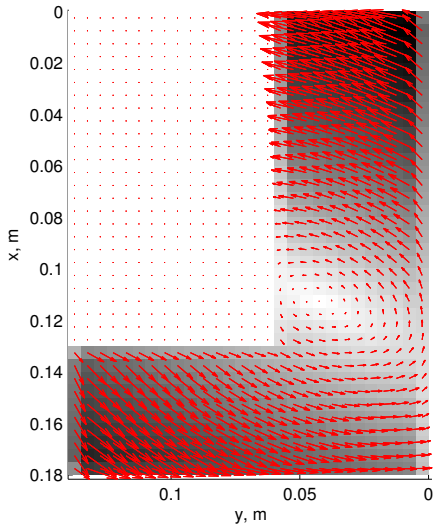

Figure 4.26: Third radiation mode of the DTV antenna system with the antenna element removed.

4.6 Summary of findings

The results from this chapter's examples of radiation and energy mode expansions yield several key points. First, the radiation mode spectrum for electrically small objects appears to be sparse. This enables the splitting of

radiating and non-radiating components of arbitrary current distributions. Furthermore, the most significant radiation modes are smooth current distributions over the entire support of an object and are relatively invariant to small perturbations to the object geometry. The spectra obtained by energy mode expansions are not as sparsely populated and this encroaches on the ability to split contributing and non-contributing current components. In light of this, it appears that the actual excited energy storage modes still form a relatively sparse set, enabling the decomposition of energy storage into a few primary current mechanisms. By examining the relative support of modes from these different expansions, the contributions for different substructures within a complex object can be examined. Furthermore, radiation modes are observed to be simple current distributions with only very loose dependence on the fine details of the object under consideration.

CHAPTER 5

RADIATION MODES OF CANONICAL CONDUCTING SURFACES

5.1 Overview

Closed-form solutions to the radiation mode eigenvalue problem are derived based on small-antenna approximations. The resulting solutions represent simple radiation sources (e.g., dipoles, loops) with simple behavior over frequency. Numerical validation shows that these solutions are valid for objects with size up to $ka = 1.0$ (largest dimension on the order of $\lambda/3$). This demonstrates that solving the discrete radiation mode eigenvalue problem is a fast, intuitive method for understanding the classical multipole expansion method of small radiating sources.

5.2 Introduction

In Chapter 4, radiation and energy storage modal expansions were demonstrated on two objects. In terms of radiation, several observations were made regarding the structure and sparseness of the active modes. In general, the radiating modes were simple in nature and had support over the entire object under consideration. This is in line with observations that small objects generally radiate via simple equivalent sources [20, 16, 52]. From this it was further concluded, in the case of the embedded DTV antenna, that the ground plane was the dominant source of radiation in the system and that its radiation properties were relatively unaffected by the driven antenna element. This implies that the antenna element simply acted to excite radiation mode currents on the ground plane. This conclusion is in line with many studies regarding the effects of finite ground planes on antenna performance (e.g., [5, 53, 54]) while providing novel quantitative understanding of the source

of radiation in the system. In light of this, it appears that when designing an embedded antenna it may be worthwhile to analyze and understand the radiation modes of the finite ground plane; as those will be the mechanisms primarily responsible for the radiation properties of the system. In this chapter, we generalize the analysis of small antennas and finite ground planes by deriving analytic solutions to the radiation eigenvalue problem on simple conducting structures. Electrically small assumptions are used to derive solutions to the continuous eigenvalue problem, though it is then shown that the two lowest-order classes of solutions maintain their derived character for structures with maximum dimension up to $\lambda/3$.

5.3 The continuous and discrete radiation eigenvalue problem

In previous chapters, radiation mode analysis was carried out using the discrete eigenvalue problem

$$\mathbf{RJ} = \nu\mathbf{PJ}. \tag{5.1}$$

Using the notation in (2.40) and (2.43), the analogous continuous eigenvalue problem is

$$\hat{R}\vec{J}(r) = \nu\vec{J}(r), \tag{5.2}$$

where

$$\hat{R}\vec{J}(r) = \frac{\eta k}{4\pi}\int_{S'}\left[\mathbf{I} + \frac{\nabla\nabla}{k^2}\right]\frac{\sin(kR)}{R}\cdot\vec{J}(r')dr'. \tag{5.3}$$

It is important to note that (5.1) and (5.2) are analogous but not the same, as $\mathbf{RJ}$ and $\hat{R}\vec{J}(r)$ are related in ways discussed in Section 2.3.3.

For electrically smaller objects ($ka < 3$), it has been observed that the eigenmodes of $\mathbf{R}$ tend to be simple, full-support current distributions with predictable structures independent of surface geometry [37, 55]. In subsequent sections we examine the continuous problem in (5.2) in order to derive closed-form expressions for radiation eigenmodes on small, canonical structures.

5.3.1 Special forms of $\hat{R}$

The operator $\hat{R}$ takes on two special forms in the electrically small limit. First, we examine the zeroth-order approximation to the real component of the dyadic Green's function in (5.3). Expanding $\sin kR/R$ into its Taylor series representation gives

$$\frac{\sin(kR)}{R} = \sum_{n}^{\infty} (-1)^n \frac{k^{2n+1} R^{2n}}{(2n+1)!}. \tag{5.4}$$

Keeping only the first two terms gives

$$\frac{\sin(kR)}{R} \approx k - \frac{k^3 R^2}{3!}. \tag{5.5}$$

This truncation is accurate to 10% for $kR < 1.66$ ($ka = 0.83$, largest dimension on the order of $\lambda/4$). We apply the first gradient operator in (5.3) to this approximation and get

$$\nabla \frac{\sin(kR)}{R} \approx -\frac{k^3}{3} \left(\hat{x}(x - x') + \hat{y}(y - y') + \hat{z}(z - z') \right). \tag{5.6}$$

Applying an outer multiplication with the second ∇ operator we arrive at the dyad form

$$\nabla\nabla \frac{\sin(kR)}{R} \approx -\frac{k^3}{3} \mathbf{I}. \tag{5.7}$$

We can insert this approximation into (5.3) to obtain a greatly simplified approximate form for $\hat{R}\vec{J}$ applicable in the small antenna limit,

$$\hat{R}\vec{J}(r) = \frac{\eta k^2}{6\pi} \int_{S'} \vec{J}(r') dr'. \tag{5.8}$$

Alternatively, the integrand in (5.3) can be rearranged as follows using integration by parts,

$$\hat{R}\vec{J}(r) = \frac{\eta k}{4\pi} \int_{S'} \left[\vec{J} + \frac{1}{k^2} \nabla'\nabla' \cdot \vec{J} \right] \frac{\sin kR}{R} dr'. \tag{5.9}$$

Assuming a divergence-free current (such as that of a small loop), the second special form of $\hat{R}$ is obtained as

$$\hat{R}\vec{J}(r) = \frac{\eta k}{4\pi} \int_{S'} \vec{J}(r') \frac{\sin kR}{R} dr'. \tag{5.10}$$

.

5.4 Solutions to the continuous radiation eigenvalue problem on simple shapes

This section is organized in three parts examining solutions to (5.2) on different choices of canonical surfaces for S.

5.4.1 Planar objects

Inserting (5.8) into (5.2) and restricting S to a planar surface yields the eigenvector / eigenvalue pair

$$\vec{J} = \hat{a} J_0 \tag{5.11}$$

$$\nu = \frac{\eta A k^2}{6\pi}. \tag{5.12}$$

These modes are predicted to be uniform in nature over the support of S, independent of the particular geometry, and have eigenvalues proportional to the area, A, of S. On any two-dimensional object, two such modes would form a quasi-degenerate two-dimensional eigenspace. In light of the uniform, linear nature of this class of modes, we associate them as electric dipole moments. This designation is consistent with the classic multipole expansion in [56].

Using the alternate special form of $\hat{R}$ given in (5.10) requires a specific choice of geometry. Suppose S to be a disk of radius a, centered at the origin with a normal vector in the $\hat{z}$ direction. Assuming a divergence-free current, we guess the following form for an eigenmode:

$$\vec{J} = \hat{\phi} f(\rho), \tag{5.13}$$

where f is an unknown function of radial distance ρ. Inserting this into (5.10) leads to

$$\hat{R}\vec{J}(r) = \frac{\eta k}{4\pi} \int_0^a \int_0^{2\pi} \hat{\phi}' f(\rho') \frac{\sin kR}{R} \rho' d\phi' d\rho', \tag{5.14}$$

where, in terms of radial coordinates,

$$R = \sqrt{(\rho - \rho' \cos\phi')^2 + (\rho' \sin\phi')^2}. \tag{5.15}$$

By taking advantage of symmetry in the angle ϕ of the chosen geometry, r can be assigned the $\hat{x}$-axis. Applying this to the above expression and rearranging terms gives

$$\hat{R}\vec{J}(r) = \hat{\phi}\frac{\eta k}{4\pi}\int_0^a f(\rho')g(\rho,\rho')\rho' d\rho', \tag{5.16}$$

where

$$g(\rho,\rho') = \int_0^{2\pi} \cos\phi' \frac{\sin kR}{R} d\phi'. \tag{5.17}$$

The function $g(\rho,\rho')$ can be interpreted as the scaled $\hat{\phi}$-directed field at distance ρ produced by a uniform current ring of radius ρ'. We examine the behavior of $g(\rho,\rho')$ by plotting it over ρ for various ring sizes ρ'. In Figure 5.1 we see that the generated field differs only by a scaling factor when the ring radius is small ($\rho' < 0.3\lambda$). However, as the ring size becomes greater ($\rho' > 0.5\lambda$), the profile of the generated field becomes highly dependent on ring size, as shown in Figure 5.2.

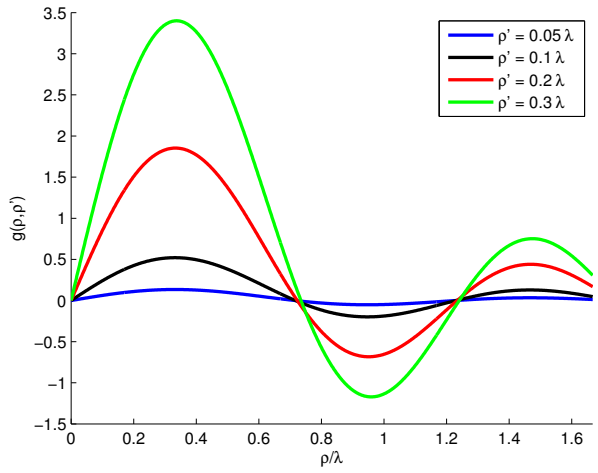

Figure 5.1: $g(\rho,\rho')$ evaluated as a function of ρ for several small values of ρ'. This is related to the real field produced by a uniform current ring of radius ρ' at an observation distance ρ in the same plane as the ring.

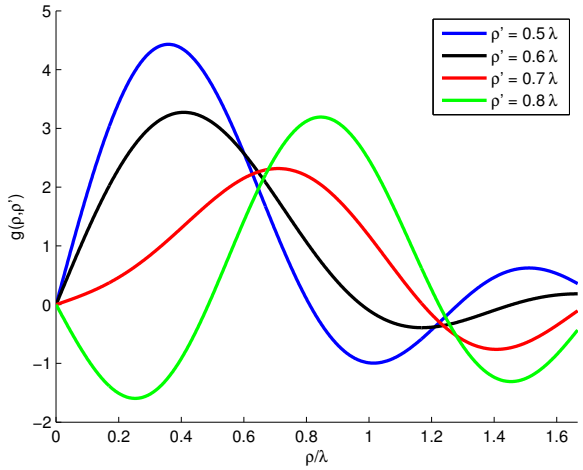

Figure 5.2: $g(\rho, \rho')$ evaluated as a function of ρ for several larger values of ρ'. This is related to the real field produced by a uniform current ring of radius ρ' at an observation distance ρ in the same plane as the ring.

The similar nature of g in Figure 5.1 suggests that g may be written as two separable functions of ρ and ρ' when ρ' is small, i.e.,

$$g(\rho, \rho') = g_1(\rho) g_2(\rho'), \tag{5.18}$$

which could greatly simplify the eigenvalue problem in (5.16). To obtain the form of g for small ρ' we apply the Taylor series for sine with small argument kR to the general expression of g,

$$g(\rho, \rho') = \int_0^{2\pi} \cos\phi' k \sum_{n=0} \frac{(-1)^n (kR)^{2n}}{(2n+1)!} d\phi'. \tag{5.19}$$

Here we keep the first two ($n = 0, 1$) terms in order to have a non-vanishing right-hand side. Assuming $kR < 1.5$ ($a < \lambda/4$), keeping only these first two terms maintains reasonable accuracy. Truncating the series in (5.19) in this way gives

$$g(\rho, \rho') = \int_0^{2\pi} \cos\phi' d\phi' - \int_0^{2\pi} \cos\phi' k \frac{(kR)^2}{3!} d\phi'. \tag{5.20}$$

The first integral is identically zero, leaving

$$g(\rho, \rho') = -\int_0^{2\pi} \cos\phi' k \frac{(kR)^2}{3!} d\phi', \tag{5.21}$$

which is separable in the way predicted in 5.18. Inserting the expression for R and rearranging we have

$$g(\rho,\rho') = -\frac{k^3}{3!}\int_0^{2\pi} \cos\phi' \left(\rho^2 + \rho'^2 - 2\rho\rho'\cos\phi'\right) d\phi'. \tag{5.22}$$

Two of the three integral terms vanish leaving

$$g(\rho,\rho') = \frac{\rho\rho'\pi k^3}{3}. \tag{5.23}$$

Inserting this approximation for g into the eigenvalue problem in (5.16) gives

$$\nu f(\rho) = \frac{\rho\eta k^4}{12}\int_0^a f(\rho')\rho'^2 d\rho'. \tag{5.24}$$

Guessing the form

$$f(\rho) = f_0\rho \tag{5.25}$$

and substituting into the above equation yields

$$\nu f(\rho) = \frac{f_0\rho\eta k^4}{12}\int_0^a \rho'^3 d\rho' \tag{5.26}$$

$$\nu f(\rho) = \frac{f_0\rho\eta a^4 k^4}{48}. \tag{5.27}$$

Thus the eigenmode / eigenvalue pair for this solution is

$$\vec{J} = \hat{\phi}\rho J_0 \tag{5.28}$$

$$\nu = \frac{\eta k^4 a^4}{48}. \tag{5.29}$$

This divergence-free mode is $\hat{\phi}$ directed and grows linearly with radial distance form the origin of the disk. Its eigenvalue grows with frequency as k^4a^4. While the choice of a disk for S was mathematically convenient for this derivation, this mode exists on all small planar geometries, regardless of shape as demonstrated in [55]. When S is not a disk, the eigenvalue of this mode still roughly follows a k^4a^4 trend, (here a is the radius of the circumscribing circle around S), though it is also scaled by the relative area of S. Because this mode is loop-like in nature, we associate it as a magnetic dipole moment.

5.4.2 Cylinders

In this subsection, S is chosen to be an open cylindrical surface (no top or bottom) of height h and radius b. The cylinder is centered at the origin oriented along the $\hat{z}$-axis. In studying planar objects, the role of the $\hat{n}\times$ operation in the continuous eigenvalue problem played no part in determining the eigenmodes of the system. In the cylindrical case, however, this operation gives rise to two distinct classes of modes associated with the electric dipole moment.

Applying (5.8) with this choice of S gives

$$\hat{n} \times \hat{R}\vec{J}(r) = \hat{n} \times \frac{\eta k^2}{6\pi} \int_{-h/2}^{h/2} \int_0^{2\pi} \vec{J}(r') b d\phi' dz'. \tag{5.30}$$

We can break $\vec{J}$ into its $\hat{z}$ and $\hat{\phi}$ components and use $\hat{z}' \cdot \hat{\phi} = 0$ to examine the individual tangential components of $\hat{R}\vec{J}$, i.e.,

$$\hat{z} \cdot \hat{R}\vec{J}(r) = \frac{\eta k^2}{6\pi} \int_{-h/2}^{h/2} \int_0^{2\pi} \hat{z} \cdot \hat{z}' J_z b d\phi' dz' \tag{5.31}$$

$$\hat{\phi} \cdot \hat{R}\vec{J}(r) = \frac{\eta k^2}{6\pi} \int_{-h/2}^{h/2} \int_0^{2\pi} \hat{\phi} \cdot \hat{\phi}' J_\phi b d\phi' dz'. \tag{5.32}$$

Clearly there is no coupling between the mismatched components of $\vec{J}$ and $\hat{R}\vec{J}$. Therefore each of the above equations could potentially lead to solutions of (5.2). Inserting (5.31) into the continuous eigenvalue problem quickly leads to another electric dipole moment eigenvector / eigenvalue pair

$$\vec{J} = \hat{z} J_0 \tag{5.33}$$

$$\nu = \frac{\eta k^2 b h}{3}. \tag{5.34}$$

Like the electric dipole modes of planar surfaces, this mode is uniform over the support of the cylinder, linearly directed, and proportional to the surface area of the cylindrical surface. Using (5.32) in (5.2) requires a few more steps. Noticing that $\hat{\phi} \cdot \hat{R}\vec{J}(r)$ has ϕ dependence owing to the $\hat{\phi} \cdot \hat{\phi}'$ within its integrand, any eigenvector must also have ϕ dependence. Specifically, by using $\hat{\phi} \cdot \hat{\phi}' = \cos(\phi - \phi')$, we see from

$$\hat{\phi} \cdot \hat{R}\vec{J}(r) = \frac{\eta k^2}{6\pi} \int_{-h/2}^{h/2} \int_0^{2\pi} (\cos\phi \cos\phi' + \sin\phi \sin\phi') J_\phi b d\phi' dz'. \tag{5.35}$$

that for any eigenmode J_ϕ must have a $\sin\phi$ or $\cos\phi$ dependence. Inserting a simple hypothesis form of $J_\phi = C\cos\phi + D\sin\phi$ into (5.35) yields

$$\hat{\phi} \cdot \hat{R}\vec{J}(r) = \frac{\eta k^2 bh}{6} \left(C\cos\phi + D\sin\phi\right). \tag{5.36}$$

Once again inserting this into result and our hypothesis for J_ϕ into the eigenvalue problem in (5.2) gives an eigenvector / eigenvalue pair

$$\vec{J} = \hat{\phi}\left(C\cos\phi + D\sin\phi\right) \tag{5.37}$$

$$\nu = \frac{\eta k^2 bh}{6}. \tag{5.38}$$

This class of modes also resembles an electric dipole polarization in the directions perpendicular to the axis of the cylinder. The modes have ϕ dependence and have eigenvalues following the same k^2bh trend seen in the $\hat{z}$-directed electric dipole modes, though with an added factor of $1/2$. Thus in contrast with planar surfaces, this cylindrical topology yields two distinct classes of electric dipole eigenmodes, owing to the behavior of the $\hat{n}\times$ operator in the continuous eigenvalue problem.

We construct a divergence-free current distribution of the form

$$\vec{J} = \hat{\phi} p(z) \tag{5.39}$$

and insert it into the alternative special form in (5.10). Here the derivation of the associated eigenvector / eigenvalue pair follows a similar path as taken with the study of the magnetic dipole mode on the planar disk. Though the distance R in this case has z'-dependent components, all of those terms vanish in the integration over ϕ'. The implication of this is that $p(z)$ is necessarily a constant, leading to the eigenvector / eigenvalue pair

$$\vec{J} = \hat{\phi} J_0 \tag{5.40}$$

$$\nu = \frac{\eta b^3 h}{12}. \tag{5.41}$$

This divergence-free eigenmode shares several properties with the magnetic dipole moment mode derived for planar objects, including its loop appearance and invariance in ϕ. Because the cylindrical surface exists at only one radial coordinate but has finite height, the dependence on the relative dimensions of S here is $k^4 b^3 h$ as opposed to $k^4 a^4$ in the planar disk case.

5.4.3 Spheres

Here S is assigned as a sphere of radius a centered at the origin. Because both components of any tangential vector on the sphere must have coordinate dependence (e.g., $\hat{\phi}\cdot\hat{\phi}'$ depends on r and r'), we expect that the uniform electric dipole modes seen on planar surfaces and cylinders will not be present. We begin by hypothesizing a general form for an electric dipole mode

$$\vec{J} = \hat{\theta} f(\theta). \tag{5.42}$$

Inserting this into (5.8) with our particular choice of S yields

$$\hat{n} \times \hat{R}\vec{J}(r) = \hat{n} \times \frac{\eta k^2}{6\pi} \int_0^{2\pi} \int_0^{\pi} \hat{\theta}' f(\theta') a^2 \sin\theta' d\theta' d\phi'. \tag{5.43}$$

Because our guess of $\vec{J}$ is symmetric in ϕ, we can place r at $\phi = 0$ without loss of generality. Thus the two tangential components become

$$\hat{\phi} \cdot \hat{R}\vec{J}(r) = \frac{\eta k^2}{6\pi} \int_0^{2\pi} \int_0^{\pi} f(\theta') a^2 \cos\theta' \sin\phi' \sin\theta' d\theta' d\phi' \tag{5.44}$$

$$\hat{\theta} \cdot \hat{R}\vec{J}(r) = \frac{\eta k^2}{6\pi} \int_0^{2\pi} \int_0^{\pi} f(\theta') a^2 (\cos\theta \cos\theta' \cos\phi' + \sin\theta' \sin\theta) \sin\theta' d\theta' d\phi'. \tag{5.45}$$

Working through the integrations shows that the $\hat{\phi}$ component is identically zero, while the $\hat{\theta}$ component reduces to

$$\hat{\theta} \cdot \hat{R}\vec{J}(r) = \frac{\eta k^2 a^2}{3} \sin\theta \int_0^{\pi} f(\theta') \sin^2\theta' d\theta'. \tag{5.46}$$

Using this in (5.2) necessitates $f(\theta) = \sin\theta$, giving rise to the eigenvector / eigenvalue pair

$$\vec{J} = \hat{\theta}\sin\theta \tag{5.47}$$

$$\nu = \frac{4\eta k^2 a^2}{9}. \tag{5.48}$$

Repeating the procedure with the aim of finding a mode analogous to the perpendicular polarization mode found on a cylinder shows that this type of mode is not supported. Thus, the electric dipole moments of the sphere are represented by three degenerate eigenmodes of the above form.

Deriving a divergence-free mode on the sphere again follows the same procedure as the magnetic dipole moments on the disk and cylinder. Guessing a form

$$\vec{J} = \hat{\phi} f(\theta) \tag{5.49}$$

and using (5.10) in (5.2) with lengthy manipulations leads to the eigenvector / eigenmode pair

$$\vec{J} = \hat{\phi}\sin\theta \tag{5.50}$$

$$\nu = \frac{\eta k^4 a^4}{9}. \tag{5.51}$$

Hence the magnetic dipole moment mode of a sphere also follows the k^4a^4 eigenvalue dependence observed for the planar disk.

5.5 Comparison with numerical results

The radiation eigenvalue problem in (5.1) is simple to implement with existing method of moments code. Calculating the matrix $\mathbf{P}$ is the only additional difficulty, which is simple enough to accomplish provided the basis function data used in simulation are available. In this section we calculate the matrices $\mathbf{R}$ and $\mathbf{P}$ for the objects studied in the previous section and solve the general eigenvalue problem in (5.1). Note that the standard eigenvalue problem (omitting $\mathbf{P}$) from [37] can also be solved, however those solutions will

have mesh-dependent eigenvalues which cannot be directly compared to the analytic forms derived in this paper. For planar objects, a rectangle of aspect ratio $\xi = \{1, 2, 10\}$ is used. The open cylinder is also simulated at these three values of ξ. Each geometry is sized according to its circumscribing sphere radius, a (drawn in Figure 5.3), and simulated over the range $0.1 < ka < 6.1$. The broad bandwidth is specifically chosen to examine the electrical sizes at which the assumptions used to derive (5.8) and (5.10) break down. Each mesh contains approximately 1500 edge elements.

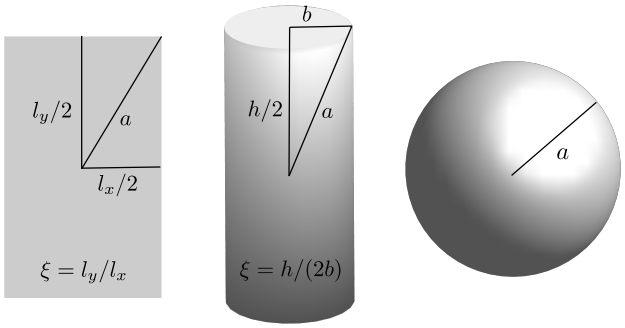

Figure 5.3: Relevant dimensions of the rectangular plate, cylinder, and sphere examined.

For each object, (5.2) is solved and the modes corresponding to the lowest-order solutions derived in this chapter are selected. The eigenvalues of these modes are compared with their derived forms and the error is quantified by three metrics. First, the error as $ka \to 0$ is calculated as the difference in eigenvalues at the smallest simulated electrical size, $ka = 0.1$. Second, the electrical size where the method of moments eigenvalue differs from the analytic solution by 10% and 25% are assigned to ka_{10} and ka_{25}, respectively. A sample plot of the eigenvalue of electric dipole moment of a rectangular plate of aspect ratio $\xi = 1$ is shown in Figure 5.4, along with the aforementioned error metrics. The general trends seen in Figure 5.4 hold for all of the geometries examined. The error metrics for each geometry, aspect ratio, and mode are listed in Table 5.1. For the rectangular plate, electric dipole modes along the short and long axes of the plate are listed as x and y, respectively, while

the magnetic dipole moment is labeled l. Similarly, the electric dipole mode on the cylinders are labeled as z and ϕ, depending on the current orientation. There the same l designation is used for the magnetic dipole modes. On the sphere, the modes are labeled simply as electric, e, and magnetic, m.

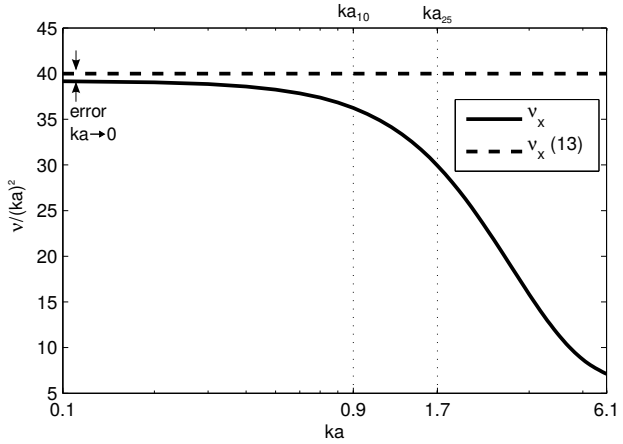

Figure 5.4: Eigenvalue of the x-directed uniform electric dipole mode on a rectangular plate of aspect ratio $\xi = 1$. Values obtained from solving (5.1) (solid) and the asymptotic analytic form in (5.12) (dashed) are drawn.

For all of the geometries examined, the solutions to (5.1) closely match those derived by (5.2) for electrical sizes $ka < 1$. All numerical eigenvalues are less than predicted by the analytic forms derived in this chapter using the $ka \to 0$ limit. Not all modes diverge from their asymptotic derived forms at the same pace, as shown by varying values of ka_{10} and ka_{25}. Because the rectangular plate is not the geometry used to derive the magnetic loop mode on planar objects, this mode is labeled with a *, as we expect the analytic solution to be potentially less well-fit. The eigenvalue for this mode is calculated using (5.29) with $b = 1/\sqrt{2}$. This approximate comparison holds well for the $\xi = 1, 2$ cases, but breaks down at the higher aspect ratio $\xi = 10$. The mode predicted by (5.12) as a quasi-degenerate pair of electric dipole moments associated with the short (x) and long (y) dimensions of the rectangular plate. As low frequencies and near-unity aspect ratios, the eigenvalues are nearly the same. At higher frequencies and at high aspect ratios, the eigenvalues diverge.

The data in Table 5.1 show that different shapes, aspect ratios, and radiation mechanisms have different persistence of their "electrically small" behavior. By examining ka_{10} and ka_{25} values, we see that different modes

Table 5.1: Comparison of analytic and numerical eigenvalues

Geometry	ξ	mode	equation	error ($ka = 0.1$)	ka_{10}	ka_{25}
plate	1	x	(5.12)	-2.13%	0.9	1.7
		y	(5.12)	-2.13%	0.9	1.7
		l*	(5.29)	1.20%	2.6	3.0
	2	x	(5.12)	-1.53%	1.1	1.9
		y	(5.12)	-3.67%	0.8	1.5
		l*	(5.29)	4.61%	2.4	2.8
	10	x	(5.12)	-0.74%	1.3	2.2
		y	(5.12)	-8.50%	0.4	1.3
		l*	(5.29)	-235.00%	0.2	0.2
cylinder	1	z	(5.34)	-6.22%	0.5	1.0
		ϕ	(5.38)	-0.39%	0.7	1.1
		l	(5.41)	-0.42%	1.0	1.6
	2	z	(5.34)	-4.24%	0.8	1.6
		ϕ	(5.38)	-0.52%	1.0	1.6
		l	(5.41)	-0.75%	1.4	2.3
	10	z	(5.34)	-1.78%	2.1	3.9
		ϕ	(5.38)	-1.05%	1.6	2.8
		l	(5.41)	-1.06%	2.3	4.1
sphere	1	e	(5.48)	-1.02%	0.5	0.8
		m	(5.51)	-1.57%	0.7	1.2

keep their similarity with their small-scatterer limit up to much higher frequencies than others. This brings into question the validity of a single limit (e.g., $ka < 1$) to define an electrically small object. For instance, from Table 5.1 we observe that a high aspect ratio ($\xi = 10$) cylinder radiating mainly in the electric dipole mode with polarization along its long axis (z mode) loses its low-frequency behavior at much higher frequency than a square ($\xi = 1$) rectangular plate operating in the analogous (x) mode.

The radiation modes associated with electric dipoles on planar objects have no dependence on the particular geometry, rather they depend only on the total surface area A. Similarly, while a circularly symmetric geometry was used to derive the planar loop moment, this radiation mode also shows very

weak dependence on the specific geometry under study, as demonstrated in Figure 5.5 (from [55]) where a rectangular plate is subjected to two kinds of modifications. Hence for small planar objects, the lowest-order radiation modes maintain their character regardless of particular geometry and have eigenvalues that scale predicable with total surface area. This makes them ideal candidates for describing the radiation properties of optimized embedded antennas, where each design iteration is some small modification of the previous iteration's geometry [42]. This concept is used in Chapter 8 to perform pattern specification on a two-element null-steering embedded antenna system.

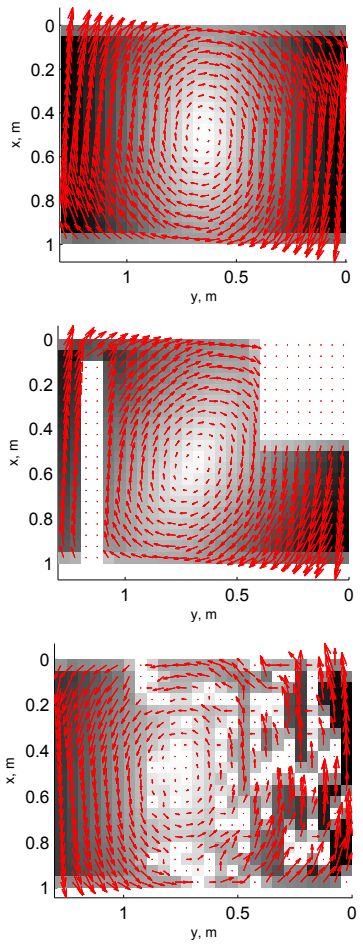

Figure 5.5: The magnetic dipole (electric loop) radiation mode on a solid plate (top), the same plate with two major regions removed (middle), and the same plate with random pixels removed (bottom).

5.6 Conclusions

The solutions to the continuous radiation eigenvalue problem for a given surface represent simple current distributions which add their powers linearly while not enforcing any orthogonality in energy storage. As demonstrated in this chapter, the lowest-order forms of these modes on electrically small objects take the form of electric and magnetic dipole moments. Hence the solutions to the radiation eigenvalue problem correspond with the low-order multipole expansion terms native to the object under consideration. Using data from existing method of moments code, the discrete form of the radiation eigenvalue problem can be solved to obtain the discretized version of these fundamental radiation mechanisms. Here we have introduced the scaling matrix $\mathbf{P}$ to ensure that solutions to the discrete problem are not mesh dependent. For objects smaller than $ka = 1$, the analytic solutions obtained using small-scatterer approximations match very well with those obtained by solving the discrete problem. At higher frequencies, the numerically calculated eigenvalues diverge from the low-frequency asymptotes, though at rates which depend on the type of mode, geometry, and aspect ratio being examined.

A key distinction between this and other modal analyses (e.g., characteristic modes [7, 8]) is the lack of coupling between radiation mechanisms and energy storage. This has the effect of reducing the variability of modal currents when small changes to geometry are made. For example, the electric dipole modes of a planar object in the small antenna limit were shown to have no dependence on geometry, rather depending only on total area. This suggests that, in problems where tailoring of radiation properties is desired, that specification of design parameters in terms of radiation eigenmodes may make for a more consistent comparison between an initial geometry and an altered design iteration. For example, comparing the radiation modes of a finite ground plane before and after a driven antenna element has been added may be a more one-to-one comparison than the same analysis performed with characteristic modes due to the lack of high-magnitude reactive currents introduced near the element in characteristic modes. If both specified resonance (or otherwise specified impedance) and radiation properties are required in a design, a hybrid design and analysis procedure making use of the strengths of both characteristic modes and radiation eigenmodes may

be the logical solution.

Additionally, the derived forms for the radiation mode eigenfunctions closely resemble those of the classic multiple moment calculations found in [56]. This connection demonstrates how the readily available method of moments impedance matrix can be used to calculate those radiating moments in a straightforward manner without resorting to the continuous integrals usually used to define them.

CHAPTER 6

A MODAL VIEW OF THE BREAKDOWN OF $\mathbf{X}_E$ AND $\mathbf{X}_M$

6.1 Overview

The loss of positive-semi-definiteness in the matrices $\mathbf{X}_e$ and $\mathbf{X}_m$ is systematically studied via eigenmode expansion. Simple current distributions with positive eigenvalues are observed to transition into negative eigenvalue modes as frequency is increased. The frequency at which negative value eigenmodes first appear depends on the particular structure being studied. Negative value eigenmodes are observed on structures as small as $ka = 1.5$ (largest dimension on the order of 0.4λ). Current distributions associated with negative value eigenmodes at lower frequencies are generally simple current distributions, likely to be excited in a driven antenna.

6.2 Introduction

The matrices $\mathbf{X}_e$ and $\mathbf{X}_m$, defined in Chapter 2, provide a simple method for calculating the Q of arbitrary currents. Useful as they are, the loss of a matrix property, *positive-semi-definiteness*, in $\mathbf{X}_e$ and $\mathbf{X}_m$ under certain conditions inhibits their use in bounding Q on electrically larger objects. In a physical context, a non-positive-semi-definite $\mathbf{X}_e$ or $\mathbf{X}_m$ implies that currents must exist which produce non-physical "negative energy". In contrast to the energy matrices, the radiation matrix $\mathbf{R}$ is always positive-semi-definite; i.e., a current never radiates "negative power". In this chapter, a modal approach is taken to methodically demonstrate the breakdown of $\mathbf{X}_e$ and $\mathbf{X}_m$ in order to better understand the limitations of these matrices in calculating stored energy and antenna Q.

6.3 Observations of non-positive-semi-definite energy operators

6.3.1 Expectations of positive-semi-definiteness

A positive-semi-definite matrix has entirely non-negative eigenvalues [57]. For any positive-semi-definite matrix $\mathbf{A}$,

$$\mathbf{x}^H \mathbf{A} \mathbf{x} \geq 0, \quad \forall \mathbf{x}. \tag{6.1}$$

Conversely, any matrix satisfying the above condition must be positive-semi-definite. Examining the quadratics in (2.29)-(2.31) and assuming that physical quantities such as radiated power and stored energy due a causal, passive system must be inherently positive, it follows that $\mathbf{R}$, $\mathbf{X}_e$, and $\mathbf{X}_m$ should be always positive-semi-definite. Small errors introduced by the numerical calculation of these matrices commonly create extremely small negative eigenvalues which can be numerically removed without substantial changes to the matrix itself. In this chapter, these kinds of negative eigenvalues are not considered and are assumed to be removed from the matrices before discussion of systematic loss of positive-semi-definiteness.

In [58] it is stated that certain structures produce non-positive-semi-definite $\mathbf{X}_e$ and $\mathbf{X}_m$ when the maximum dimension exceeds approximately $\lambda/3$. Thus an eigenmode of one of these matrices which has a negative eigenvalue represents a current distribution which stores "negative energy". Such a current distribution will be discussed in this chapter as a *negative energy mode*. From a physical perspective, this type of current is quite perplexing. Several questions arise:

- First, what kinds of currents are represented by negative energy modes; are they simple or exotic, systematic or highly-variable?
- Second, what is the physical interpretation of negative energy modes? Do they represent a true physical state or an inaccurate calculation?
- Finally, does the frequency (or electrical size) at which $\mathbf{X}_e$ or $\mathbf{X}_m$ lose positive-semi-definiteness indicate a hard threshold up to which Q calculated via (2.20) is accurate? If a current distribution produces both

negative electric and magnetic stored energy, is there a proper interpretation of negative Q or is this completely inaccurate?

In the following subsection, the second question regarding the physical explanation of negative energy modes is addressed with the most recent theories from the literature. Later in the chapter, the accuracy of Q and nature of negative energy modes is examined by novel eigenmode analysis.

6.3.2 Explanations of negative energy current distributions

The physical interpretation of negative, time harmonic stored energies is still a matter of debate, but it is generally believed to be an artifact of working strictly in the steady-state frequency domain and neglecting transient effects [59, 60, 61]. One explanation is that positive energy is required to start and stop the steady-state currents which produce negative energy in the frequency domain. In [60], it was shown that incorporation of these positive "setup" and "shutdown" energies always results in net positive stored energy. In light of this explanation, it is still important to understand when issues with positive-semi-definiteness affect Q calculations. For example, the method for using convex optimization to bound Q on arbitrary objects given in [58] ceases to work when one or both energy matrices are non-positive-semi-definite. Additionally, a current which produces negative electric and magnetic energy would necessarily have a negative quality factor. From either a bandwidth or time-constant interpretation, negative Q does not make physical sense. The work in this chapter avoids discussing the physical implication of negative energy modes, but rather investigates the occurrence and behavior of such modes to inform the use of the energy matrix operators in calculations of Q.

6.4 Modal analysis of the loss of positive-semi-definiteness in $\mathbf{X}_e$ and $\mathbf{X}_m$

6.4.1 Experimental procedure

Several canonical shapes are studied over wide a wide frequency range in order to determine the electrical size at which positive-semi-definiteness is lost

in $\mathbf{X}_e$ and $\mathbf{X}_m$. For each object, the energy storage matrices $\mathbf{X}_e$ and $\mathbf{X}_m$ are generated at 101 logarithmically-spaced points over the range $ka \in [0.1, 10]$. The shapes selected for this study represent common antenna topologies as well as those of finite ground planes. Each geometry and its relative dimensions are shown in Figure 6.1. The eigenmodes of $\mathbf{X}_e$ and $\mathbf{X}_m$ were calculated at each frequency point in order to obtain frequency-dependent eigenspectra of the energy operators. Within these spectra, eigenmodes with negative eigenvalues were identified and singled out for examination. In studying the eigenspectra of $\mathbf{X}_e$ and $\mathbf{X}_m$, it became apparent that both matrices display high number of eigenmodes with nearly degenerate eigenvalues which cross and avoid in complex ways over frequency. With this kind of data even well-tuned eigenmode tracking algorithms, such as the one described in Section 2.4, have difficulty tracking individual eigenvalue traces over frequency. In light of this, the eigenspectra presented in this study are given in unsorted form. To examine a given eigenmode over frequency, manual tracking was employed and shift-and-invert techniques [62] were used to isolate particular eigenmodes at specific frequencies.

The objects selected for study consist of basic geometries, rather than specific antenna types. The details of the strip dipole and elliptical ring are elaborated on in the following section. The plate and perturbed plate are chosen to examine the effect of small structural changes on energy storage matrix behavior. Similarly, a cube is chosen to highlight the effect of higher dimensionality on the appearance of negative energy modes.

6.4.2 Results

The eigenspectra of $\mathbf{X}_e$ and $\mathbf{X}_m$ for each geometry are presented and negative energy modes are identified. The simplest geometry is that of the strip dipole, the eigenspectra of which is shown in Figure 6.2. The strip a rectangle with a length / width ratio of 1000. The spectrum of $\mathbf{X}_e$ is simple in nature, with all modes showing generally decreasing eigenvalues with increasing frequency. Two modes, labeled Modes 1 and 2 in Figure 6.2 become negative energy modes within the studied frequency range. All eigenmodes of the magnetic energy storage matrix generally show increasing eigenvalues with increasing frequency and no negative energy modes are observed.

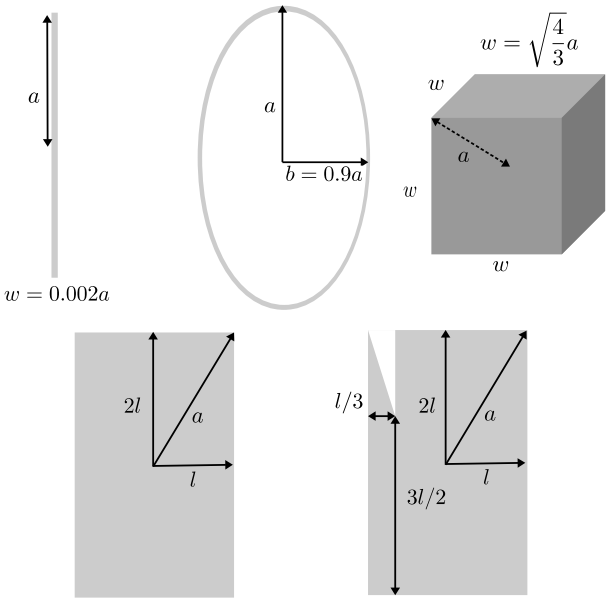

Figure 6.1: Geometries studied in this chapter. Top row, left to right: strip dipole, elliptical loop, and cube. Bottom row, left to right: rectangular plate and perturbed rectangular plate.

To examine the nature of the negative energy modes on this structure the modal currents of Modes 1 and 2 (as identified in Figure 6.2) are plotted near their zero-crossings in Figure 6.3. Neither modal current distribution changes significantly with frequency as its eigenvalue crosses zero. The two modes are the first- and second-order dipole-like current distributions over the length of the dipole. Mode 1, the first-order dipole mode, has a zero crossing near $ka = 4.4$, or equivalently $l = 1.4\lambda$. The second-order mode crosses near $ka = 8.2$ or $l = 2.6\lambda$. From these data it's clear that negative energy modes can be basic current distributions which do not necessarily undergo significant changes as they transition to storing "negative energy".

A loop is examined to continue study of canonical radiating structures. To avoid degeneracies among axially-symmetric eigenmodes, a slight eccentricity is applied such that the loop is actually elliptical. The major and minor axes are $a = 1$ and $b = 0.9$, respectively. Both sets of energy storage eigenmodes of the ellipse are shown in Figure 6.4. In this example, the eigenspectra of $\mathbf{X}_e$ shares some features with that of the strip dipole. Most modes appear to

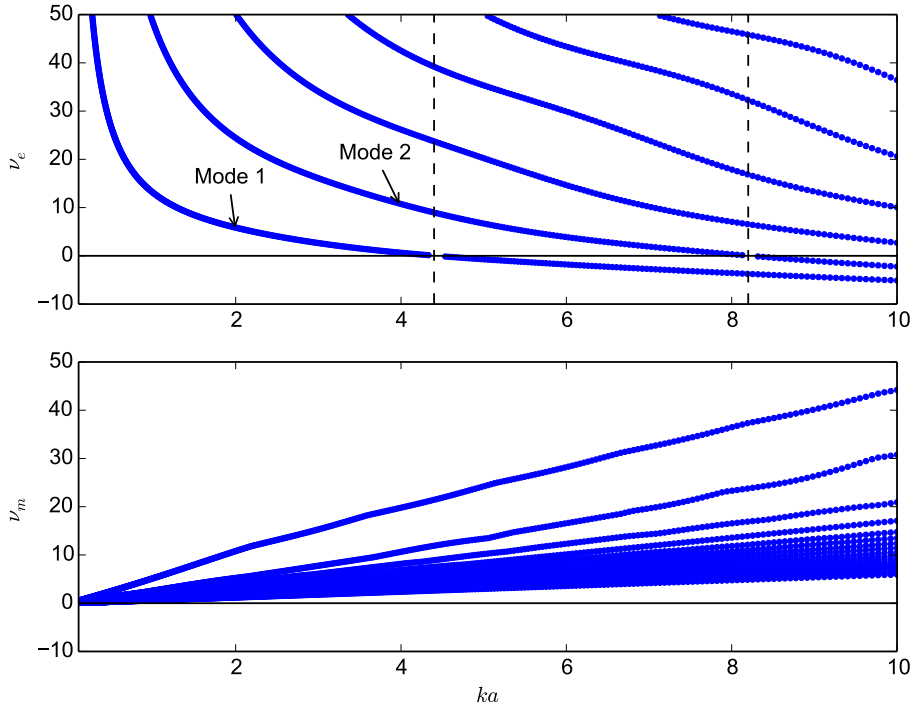

Figure 6.2: Eigenspectra of the energy storage matrices $\mathbf{X}_e$ (top) and $\mathbf{X}_m$ (bottom) for a strip dipole.

have decreasing eigenvalues with increasing frequency, and several of these transition to negative energy modes within the studied spectrum. In addition to these, there are also many eigenmodes with eigenvalues which oscillate around zero as functions of frequency. One mode sharing similar eigenvalue characteristics with those previously seen is labeled Mode 2 on Figure 6.4. The zero-crossing of this mode's eigenvalue occurs at $ka = 3.26$, or $a = 0.52\lambda$. Additionally, the first observed mode with an oscillating eigenvalue is labeled as Mode 2. The first zero-crossing of Mode 1 is at $ka = 1.4$, or $a = 0.23\lambda$. The current distributions of both modes are plotted near their zero-crossings in Figure 6.5.

The dipole moment represented by Mode 2 changes little through its zero crossing. Mode 1 is a uniform loop moment which changes minimally through its first zero-crossing. Slight irregularity is apparent in the current distribution of Mode 2 after its zero crossing, but this is likely due to coupling effects with Mode 1 near their eigenvalue crossing avoidance [35].

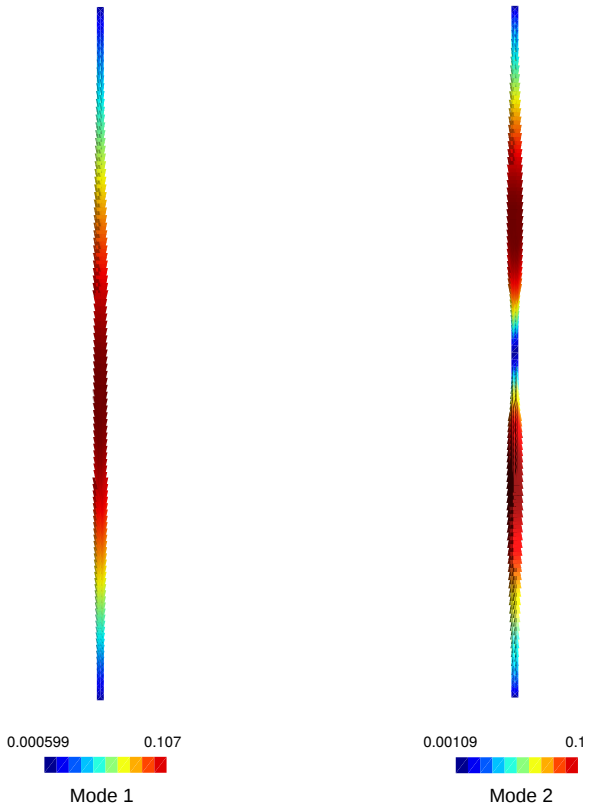

Figure 6.3: Negative energy modal current distributions of a strip dipole near their eigenvalue zero crossings, as labeled in Figure 6.2.

Unlike the strip dipole, whose magnetic energy matrix stays positive-semi-definite throughout the studied frequency range, the matrix $\mathbf{X}_m$ of the ellipse admits negative energy modes at higher frequencies. One such mode is labeled as Mode 3 on Figure 6.4. The modal current distributions associated with Mode 3 near its zero crossing, as shown in Figure 6.5, shows that this particular negative energy mode has two features which makes it unlikely to be encountered in physical radiating currents on this structure. First, the currents of Mode 3 have extremely high spatial variation, with several sign changes around the perimeter of the ellipse. Second, the currents are oriented radially along the width of the ellipse, suggesting that this mode could only be excited by excitation normal to that typically used to feed such a ring. Other negative energy modes appearing in $\mathbf{X}_m$ at high frequencies share these features.

The other geometries previously shown in Figure 6.1, are also studied in this manner. The results from the dipole and ellipse represent the consistent

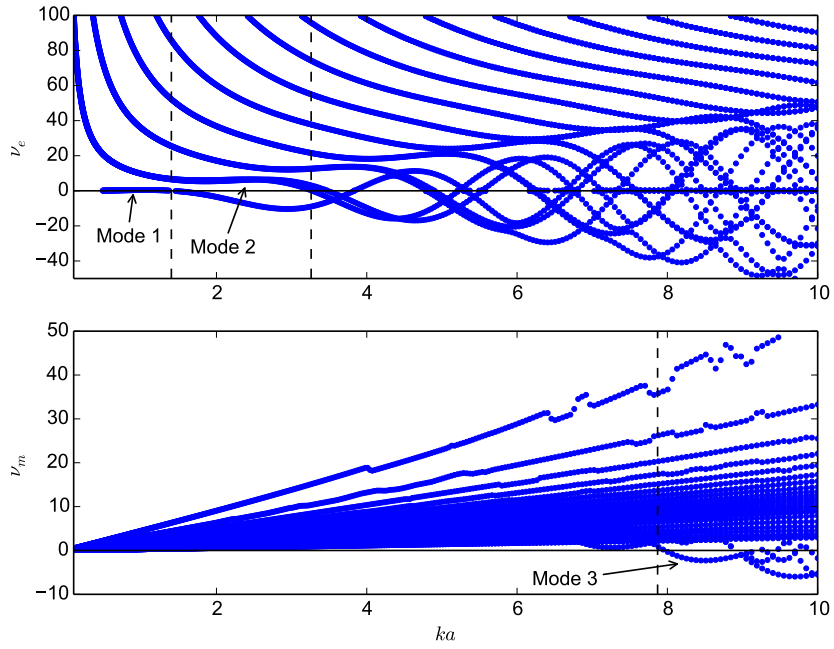

Figure 6.4: Eigenspectra of the energy storage matrices $\mathbf{X}_e$ (top) and $\mathbf{X}_m$ (bottom) for an elliptical ring.

features seen in all examples. In most of the examples, the electric energy storage matrix loses positive-semi-definiteness at lower frequencies than the electric energy storage matrix. The only exception to this is the three dimensional box model. The frequency at which the first negative energy mode in each matrix appears is reported for each geometry in Table 6.1. Negative energy modes from both matrices resemble simple dipole- and loop-type currents which change little through their transition from positive to negative energy storage. For objects which support loop-type currents, uniform circulating current modes represent the first negative energy mode appearing in either energy storage matrix. The geometry of the object under study plays a large role in when negative energy modes occur, though the small differences in the plate and perturbed plate analyses show that the general structure of an object, not its fine details, determine the frequency at which the energy storage matrices lose positive-semi-definiteness.

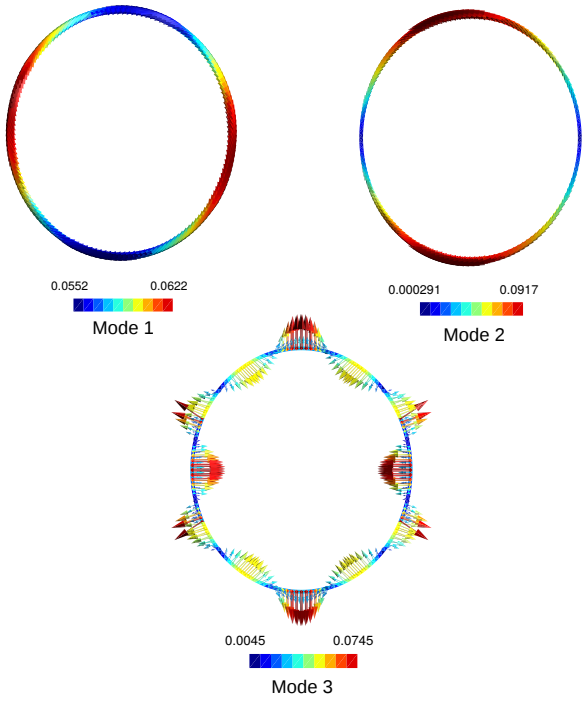

Figure 6.5: Negative energy modal current distributions of an elliptical ring near their eigenvalue zero crossings, as labeled in Figure 6.4.

6.4.3 Characteristic modes as negative energy modes

In Section 6.4.2, current distributions which yield negative stored energies were isolated by eigenmode expansions in energy storage matrices. To further test the idea that simple, easily realizable currents, the negative energy properties of characteristic modes (see Section 4.3.3 for formulation) are examined. Data in [35] suggests that the characteristic modes of a strip dipole produce negative energy above their resonant frequencies. Similar data is presented here using the shapes studied in this chapter. The stored electric and magnetic energies of the i^{th} characteristic mode are

$$2\omega \bar{W}_e^i = \mathbf{J}_i^T \mathbf{X}_e \mathbf{J}_i \tag{6.2}$$

and

$$2\omega \bar{W}_m^i = \mathbf{J}_i^T \mathbf{X}_m \mathbf{J}_i. \tag{6.3}$$

The spectral properties of the characteristic mode problem are much more conducive to broadband frequency tracking than the energy storage modes.

Table 6.1: Summary of first negative energy modes on several objects

Geometry	First $\mathbf{X}_e$ NEM ka $(2a/\lambda)$	First $\mathbf{X}_m$ NEM ka $(2a/\lambda)$
Strip dipole	4.40 (1.40)	n/a
Elliptical loop	1.40 (0.44)	n/a
Plate	1.84 (0.56)	2.90 (0.92)
Perturbed plate	1.84 (0.56)	3.08 (0.98)
Box	1.45 (0.46)	1.30 (0.41)

Because of this, the characteristic modes' energies can be plotted easily as functions of frequency. Figure 6.6 shows the modal energies of the first several characteristic modes of the strip dipole studied earlier in the chapter. Negative energies in characteristic modes can only occur when the energy storage matrices are non-positive-semidefinite. Comparing Figure 6.6 with the energy storage eigenspectra in Figure 6.2, it appears that the characteristic modes of this simple system become negative energy current distributions as soon as negative energy modes are present. Because $\mathbf{X}_m$ does not support negative energy modes on this structure, characteristic modes with both negative electric and negative magnetic energies do not exist. This means that no characteristic modes within this frequency range would broach the difficult result of negative Q, which as stated before is difficult to interpret in either a bandwidth or time-constant perspective.

A contrasting case exists for the rectangular plate. Table 6.1 shows that both energy matrices lose positive-semi-definiteness on this geometry. Examination of the characteristic modal energies in Figure 6.7 shows that indeed there exist characteristic modes which produce both negative electric and magnetic energies. The negative Q modes here are three dipole moments (Modes 1, 2, and 4) and a loop moment (Mode 3). Because characteristic modes are commonly thought of as an approachable, realizable set of current distributions supported on an object, the presence of negative Q characteristic modes is even more concerning than the loss of positive-semi-definiteness of the energy storage operators. Reporting of Q values of a similar strip dipole in [34] using several methods suggests that the energy storage approach to Q calculations may be accurate even when one energy storage matrix is non-positive-semi-definite. These calculations have been validated using the code used in this dissertation as well. However, in that paper, no negative Q val-

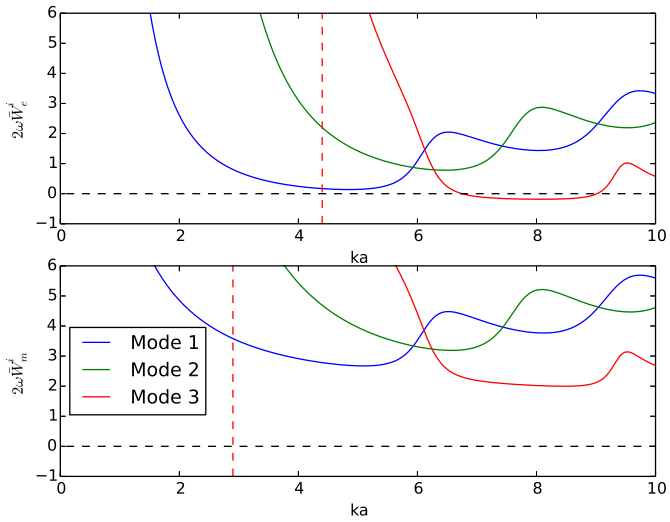

Figure 6.6: Individual stored electric (top) and magnetic (bottom) energies of the three lowest-order characteristic modes of the previously studied strip dipole. The vertical red dashed line indicates where the associated energy storage matrix loses positive-semi-definiteness.

ues are reported. It should be noted that, as discussed in [34, 35, 63], the orthogonality conditions imposed on characteristic modes do not imply linear addition of individual stored energies. While these non-linear effects are generally small compared to individual modal energies, the net energy storage determining Q of a total current may not be perfectly represented by the Q properties of its constituent characteristic modes. Study of large plate-like objects in Chapter 7 shows that, for high Q systems, the presence of negative Q modes may not be detrimental to the calculation of total system Q.

6.5 Conclusions

The purpose of the study in this chapter was to add further specification to the nature of the eigenvalue components responsible for the loss of positive-semi-definiteness in the energy storage matrices $\mathbf{X}_e$ and $\mathbf{X}_m$. The loss of positive-semi-definiteness was previously understood in two regards: first, it represents an interesting physical scenario that indicates a lack of completeness in frequency-domain calculations; second it clouds the applicability of the energy storage matrices to the calculation and bounding of Q. In terms of

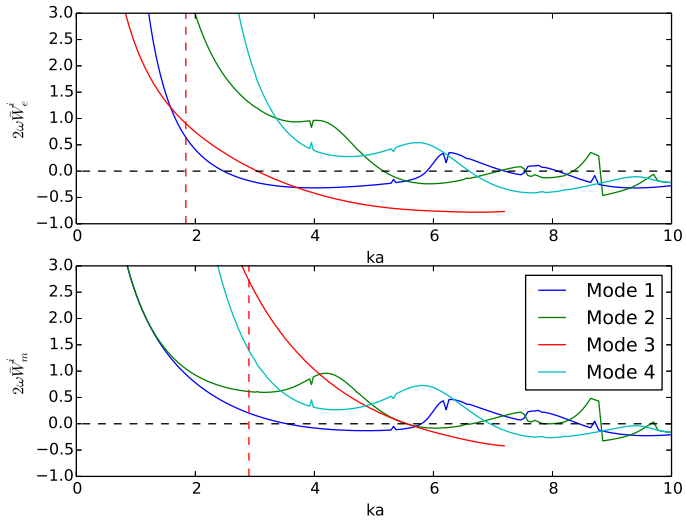

Figure 6.7: Individual stored electric (top) and magnetic (bottom) energies of the three lowest-order characteristic modes of the previously studied rectangular plate. The vertical red dashed line indicates where the associated energy storage matrix loses positive-semi-definiteness.

the first point, this study adds little to the physical understanding of negative energy modes and what they represent. To understand the balance of transient and steady state calculations of energies, certainly more research along the line of [59, 60] and [34, 64] is required. On the second point, the existing knowledge, summarized in [14], was that objects larger than $\lambda/3$ should be avoided when using this method for the calculation and bounding of Q, with the added note that loops were observed to lose positive-semi-definiteness, a fact first exposed in [31].

The results from this chapter indicate that the frequency (or electrical size) at which an object loses positive semi-definiteness is dependent on the shape of the object under test. Indeed, of the objects studied the loop-type structure shows one of the earliest appearances of negative energy modes, corroborating the analytic work in [31]. Small perturbations to geometry appear to have minimal effect on negative energy modes, rather it is the overall shape and dimensional support which dictates their appearance. The data also indicate that many simple radiating current distributions become negative energy modes at high frequencies. In fact, all of the first appearing negative energy modes (i.e., the first causes of loss of positive-semi-definiteness)

are such simple mechanisms. This provides the insight that negative energy modes (and whatever their interpretation is in a complete physical picture) arise not from exotic current distributions, but rather from currents of a type frequently encountered in antenna systems. This notion is further reinforced by the observation that characteristic modes themselves may become negative energy modes. The uncovering of these new aspects of negative energy modes were largely enabled by the energy storage eigenvalue expansion utilized in this chapter.

Using optimization methods to bound Q using the energy storage matrices clearly breaks down when positive-semi-definiteness is lost, as currents with zero or negative energy storage can be readily synthesized. However, this says nothing of the actual accuracy of Q as calculated by these means when negative energy modes are present. In fact, several sources in the literature (e.g., [34]) report accurate Q calculations using the energy storage matrix method on electrically large objects. The comparative accuracy of Q on larger objects is discussed further in Chapter 7.

CHAPTER 7

CONVERGENCE OF PHYSICAL RADIATION MECHANISMS WITH RESPECT TO GROUND PLANE SIZE

7.1 Overview

The effects of ground plane size are studied in the context of Q and radiation mode expansion. Using the results from this study, saturation of Q is associated with the transition from single-mode radiation to multi-mode radiation. Thus the size of the finite ground plane only affects the potential bandwidth of the entire antenna system when it itself supports the low-order radiation mode moments over most of its surface. Using square ground planes of varied sizes and a variety of antenna elements with fixed maximum dimensions on the order of $\lambda/5$, this transition in radiation mechanisms was observed to occur as ground plane side length approached $\lambda/2$.

7.2 Introduction

Though many analysis problems in antenna theory begin with an assumed infinite ground plane, in practice all ground planes are of finite size. The effects of this truncation are small in some cases, e.g., when the finite ground plane is large enough compared to both the operating wavelength and the antenna element. In other cases, the effects are drastic; particularly when the ground plane (or generally, ground structure) is reduced to the order of a wavelength and when the driven antenna is electrically-small. In this scenario, radiation patterns tend to be highly dependent on the relative positioning of the antenna element with respect to the ground plane [5]. Similarly, the size of a finite ground plane plays a key role in the antenna's matched impedance [54] and bandwidth [65, 66, 53]. For these reasons, when an electrically-small antenna is mounted to a finite ground structure it is colloquially said that

the ground plane is a radiating part of the antenna. When discussing these kinds of systems in terms of Q or electrical size, it is understood that the electrical size needs to encompass part or all of the ground plane to give an accurate prediction of system performance informed by size-based metrics, e.g, those in [20]. This inclusion makes sense for systems which have small ground planes: the larger the ground plane, the larger the effective electrical size. However, in the case of an ever-increasing ground plane size, we expect the effective electrical size of the system to converge to that of the electrically-small driven antenna element. This expected behavior is drawn schematically in Figure 7.1 where ka, kb, and kc are the electrical-size of the antenna element, ground plane, and total system, respectively.

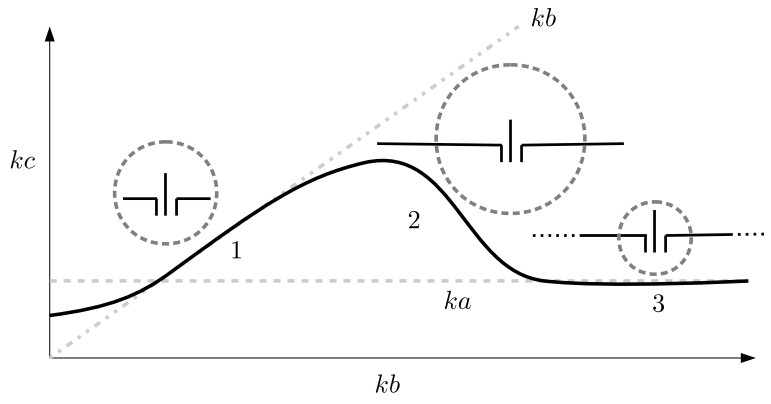

Figure 7.1: Schematic of proposed behavior of "effective electrical size" kc as a function of ground plane size kb (solid). Also drawn are the ground plane size kb and antenna element size ka (labeled, dashed). Points 1, 2, and 3 are accompanied by sketches of the antenna / ground plane system and its effective circumscribing circle of radius kc (dashed circle).

We propose three key regions to be identified in Figure 7.1. Near point 1, the ground plane size kb is on the order of the electrical size of the antenna element ka. We expect from a radiation point of view that the ground plane size should be taken into account to the effective system size kc, i.e., as the ground plane size kb grows, the system size kc grows also. At a certain point this trend should end, as in the infinite ground plane limit ($kb \to \infty$) the system size kc must converge to a size on the order of the antenna element

ka. We denote this transition region by point 2 while point 3 represents convergence to the infinite ground plane limit. The hypothesized trends in Figure 7.1.

In this chapter, several measures are examined as functions of ground plane size for small antenna systems. These measures include input impedance, Q, and the modal analyses introduced in previous chapters. Through these studies, the hypothesized model in Figure 7.1 is tested and operating regions (in terms of ground plane size) are classified. The framework of the experments in this chapter originally appeared in [67].

7.3 Design examples

In all of the following examples, a small antenna structure is near or attached to a square ground plane of side-length L. The orientation, placement, and design of the examples studied here were chosen to represent both canonical radiating systems (e.g., a dipole current over a conducting plane) as well as practical antenna designs (e.g., an edge-mounted planar monopole). For the purposes of drawing general conclusions regarding the physical effects associated with ground plane size, emphasis is placed on studying many different antenna configurations and topologies as opposed to the detailed parametric treatment of one particular design.

7.3.1 Canonical systems

A slot within an infinite ground plane and a small electric dipole above an infinite ground plane are examples of simple radiating systems whose nature is most commonly analyzed using equivalence principle techniques. In the case of the slot, the problem is typically converted to one of an equivalent radiating magnetic current using the equivalence principle on the infinite ground plane. For the radiating current above a ground, the infinite conducting plane is typically removed and replaced with an equivalent image current. In these examples, convergence to the asymptotic infinite ground plane scenario is studied as the finite ground plane size is varied. Both the slot and dipole are assigned lengths of $l = \lambda/5$ and widths $w = \lambda/55$. The dipole is center-fed using a delta-gap source while the slot is fed using a cen-

trally located pin of width $w_f = \lambda/100$. The dipole is oriented parallel to and at height $h = \lambda/15$ above the ground plane. Both examples are drawn schematically in Figures 7.2 and 7.3.

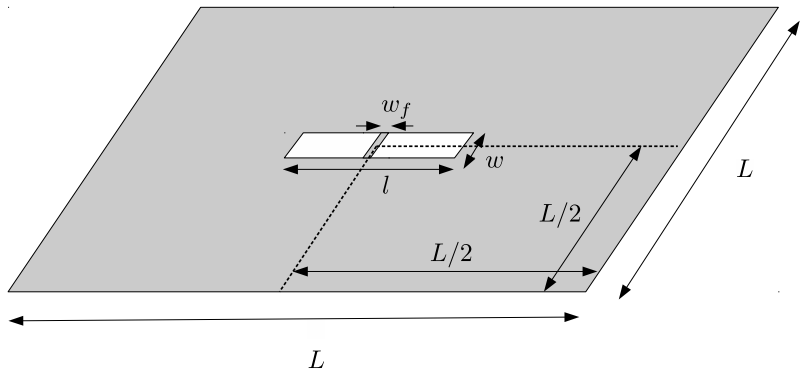

Figure 7.2: Schematic of slot antenna in a square finite ground plane of dimension L. The slot has length l, width w and is fed by a centrally located feed pin of width w_f.

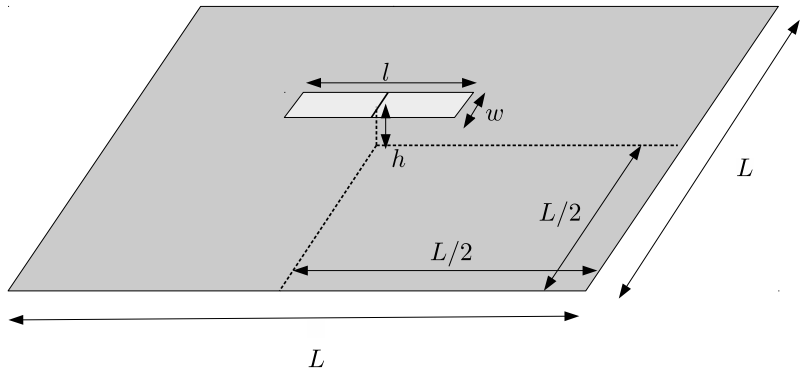

Figure 7.3: Schematic of dipole antenna above a square finite ground plane of dimension L. The dipole has length l, width w and is fed by a centrally located delta-gap source.

7.3.2 Edge-mounted antennas

In mobile devices, antennas are frequently mounted on or near the edge of the conducting chassis acting as a ground plane [4]. In contrast to the

previously discussed examples, intuitive forms for the asymptotic behavior with respect to ground plane size are not, in general, available for edge-mounted topologies. The examples of edge-mounted antennas studied in this chapter can be classified by the following features: placement along the ground plane edge and dimensionality. Several of the examples studied have feeds located at the center of a ground plane edge. Thus as the ground plane becomes larger, it extends away from the antenna feed point evenly in three directions leading to a quasi-infinite half-plane. In contrast, antennas mounted on the corner of a ground plane experience ground plane growth in only two directions, giving rise to a quasi-infinite quarter plane. These configurations are drawn schematically in Figure 7.4. The dimensionality of particular examples refers to whether the designs are exist entirely in the same plane as the ground plane or whether they extend into the third dimension.

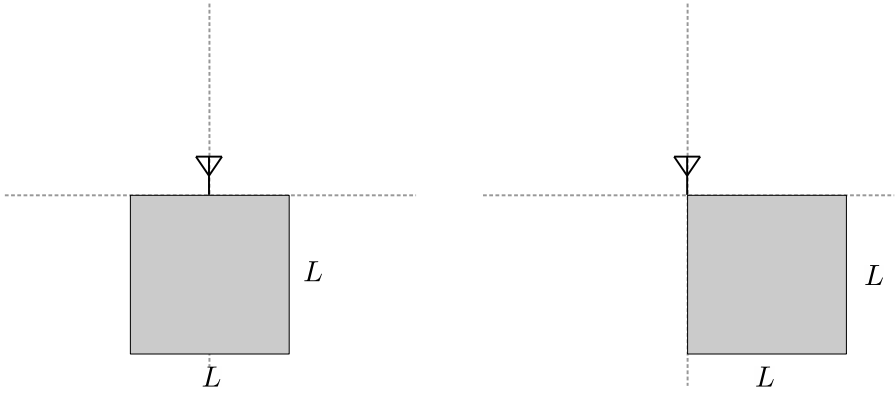

Figure 7.4: Schematic of center (left) and corner (right) locations for edge-mounted antennas on a square ground plane of side-length L.

All of the edge-mounted antennas studied here are variations of a monopole. Three straight monopoles are shown in the top row of Figure 7.5 in *planar*, *corner-planar*, and *folded* configurations. Three bent monopoles, or L-monopoles are also studied as shown in the bottom row of Figure 7.5 in *planar*, *vertical*, and *folded* configurations. In all of these designs, the antenna has a total length $\lambda/5$ and is fed at its junction with the ground plane by a delta-gap source. In both folded models, the antenna has a height $\lambda/40$ over the ground plane.

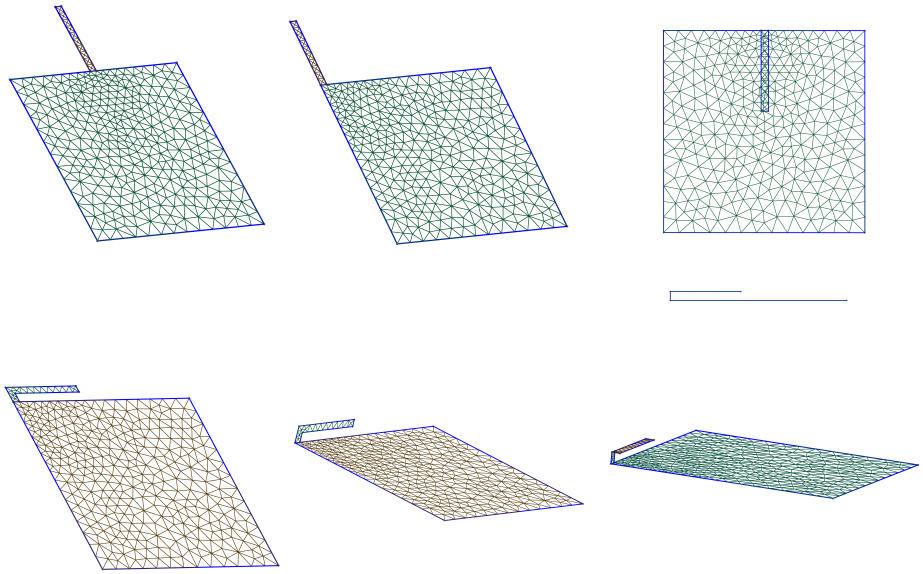

Figure 7.5: Geometries of the six edge-mounted antennas studied. All antennas are displayed on 0.5λ square ground planes. Top row left to right: planar monopole, corner planar monopole, folded monopole (top and side views). Bottom row left to right: planar L, vertical L, folded L. All antennas have dimension on the order of $\lambda/5$. Folded models have height $\lambda/40$ above the ground plane.

7.4 Input impedance convergence

The input impedance, Z_{in}, is a logical first step in analyzing antenna performance as a function of ground plane size. Figures 7.6 and 7.7 show the input resistance, R_{in}, and input reactance, X_{in}, of each antenna design as it varies with ground plane size L.

All antenna models' input resistances, R_{in}, converge or show signs of converging by $L/\lambda = 2$. Trends in R_{in} increasing or decreasing with L in the small L limit are not consistent. Models with the same feed location (e.g. planar monopole and folded monopole) share many similarities in the shape of R_{in} as a function of L/λ, though the relative scales are very different.

With the exception of the slot antenna, all input reactances, X_{in} are negative (overall capacitor-like behavior) and become more positive with increasing L/λ. Unlike the input resistances, very few similarities can be observed

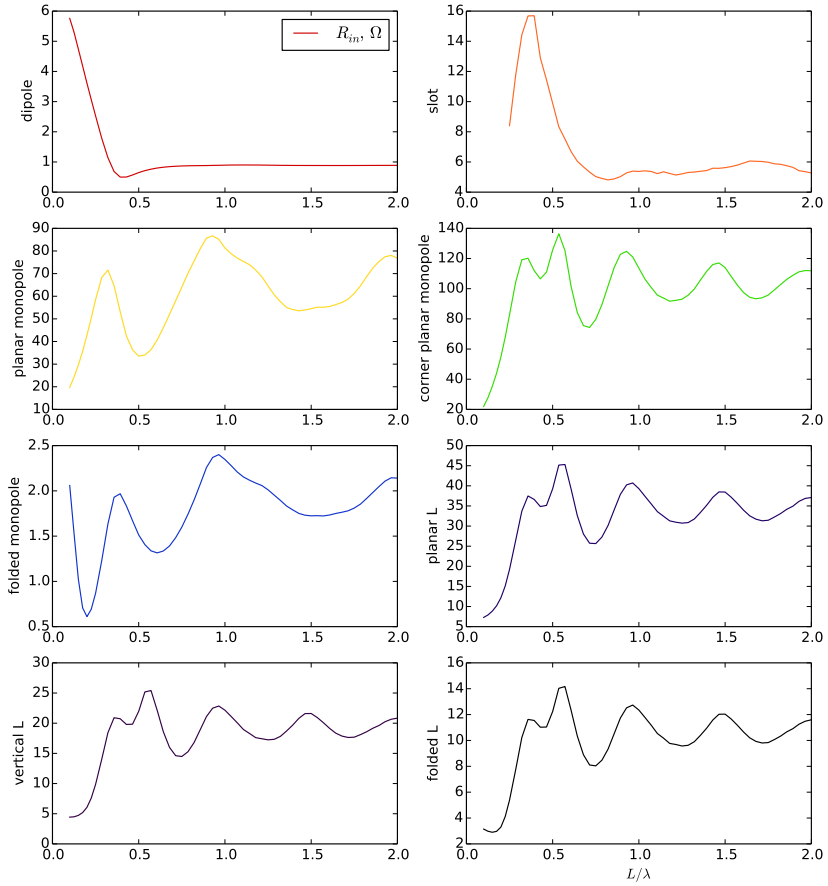

Figure 7.6: Input resistance, R_{in}, of each antenna type as a function of ground plane size L. All x-axes are L/λ.

between models' input reactances. Examining the input impedances in this way gives clues as to the general convergence behavior of the system as a function of ground plane size. It appears that the convergence behavior of input resistance depends heavily on feed location, while input reactance is dependent on the specifics of the model being examined. Both real and imaginary components of the input impedance appear to begin convergence (i.e., oscillating about some asymptotic value) between $L/\lambda = 0.5$ and $L/\lambda = 0.75$. While X_{in} represents the net energy storage difference as seen by the feed, it gives no information as to the individual electric and magnetic stored energies without multi-frequency sampling. Similarly, the input resistance converges,

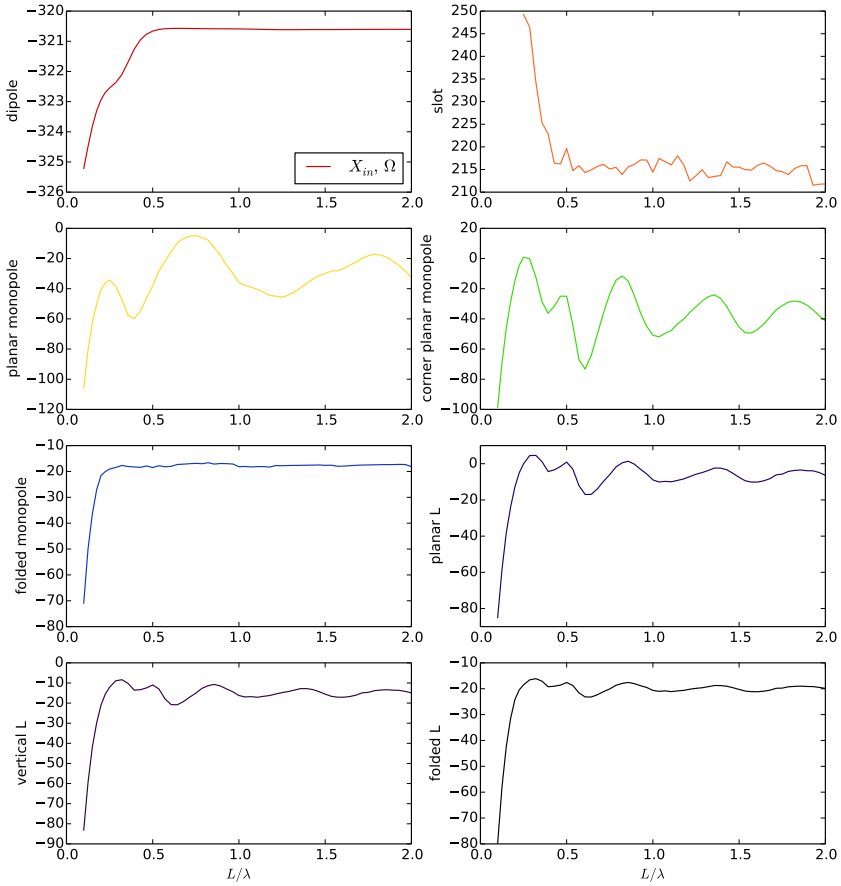

Figure 7.7: Input reactance, X_{in}, of each antenna type as a function of ground plane size L. All x-axes are L/λ.

but examination of that alone doesn't elucidate the roles that the ground plane and driven antenna element play in manifesting radiation.

7.5 Q convergence

To investigate the role of the ground plane in "adding electrical size" to the small antenna element, the quality factor Q is calculated for each model as a function of L/λ. As studied in previous chapters, the accuracy of Q as calculated by the matrices $\mathbf{X}_e$ and $\mathbf{X}_m$ may be compromised as the object

under study becomes electrically large. Interestingly, in the limit of an infinite ground plane, two of the antennas (the dipole and slot) should converge to effective electrical sizes on the order of $\lambda/5$. In the case of the dipole, the infinite ground plane system can be substituted for one containing the dipole and its image. For the slot, the infinite ground plane system can be replaced by a magnetic radiator with dimensions equal to those of the slot. Hence the study of these two examples will not only aid in the testing of the trends proposed in Figure 7.1, but also will examine the behavior of the energy storage matrices for electrically large objects with small effective electrical size.

Two other quality factor calculations are use as baseline comparisons for the accuracy of Q as calculated by $\mathbf{X}_e$ and $\mathbf{X}_m$. The first, commonly denoted Q_Z in the literature, is calculated using the input impedance differentiated with respect to frequency. Derived in [26], this derivative method is given by

$$Q_Z = \frac{\omega}{2R_{\text{in}}} \left| \frac{\partial Z_{in}}{\partial \omega} \right|. \tag{7.1}$$

In [26], several conditions are listed as necessary for the accuracy of Q_Z; though throughout the authors' several antenna examples no exceptions to these conditions are found. As discussed in Chapter 2, the practical importance of Q is its functional relation to tuned impedance bandwidth. In general, this functional relation can be quite complex [21], though for sufficiently narrowband systems, the inverse relation $Q \sim 1/FBW$ approximates the relationship well. Here fractional bandwidth, FBW, about a center frequency ω_0 is defined as

$$FBW = \frac{\omega_+ - \omega_-}{\omega_0}, \tag{7.2}$$

where ω_+ and ω_- are the upper and lower band edges, respectively, for a given impedance mismatch. Defining the maximum tolerable VSWR as s, the quality factor of a narrowband system is given by [26],

$$Q_B = \frac{2\sqrt{\beta}}{FBW}, \quad \sqrt{\beta} = \frac{s-1}{2\sqrt{s}}. \tag{7.3}$$

Both Q_B and Q_Z assume relatively narrowband signals, i.e., $FBW < 1$. The quality factor, as calculated by the energy matrices and the two aforementioned methods, is shown in Figure 7.8 as a function of ground plane size.

The bandwidth-based calculation Q_B, is very computationally expensive to compute and is only shown at two points for the planar monopole, vertical L, and corner planar monopole models. In calculating Q_B, a maximum VSWR of $s = 1.5$ ($\sqrt{\beta} = 0.2041$) was selected following the convention described in [26].

For high values of Q (> 20), all methods agree very well. For values lower than this, the energy matrix method consistently over-estimates Q, while Q_Z an Q_B stay in agreement except in cases of extremely low Q, when the narrowband assumptions break down. With the exception of the dipole and folded monopole, all example antenna systems have consistent $\partial Q/\partial L < 0$ in the low L/λ limit. This indicates that, in this regime, adding more material to the system increases radiated power faster than stored energies. This behavior ends for most models near $L/\lambda = 0.4$. With the exception of the slot and dipole models, Q remains in the vicinity of its minima reached at $L/\lambda = 0.4$ for increasing L/λ. This suggests that, for antennas of this size, the ground plane contributions to radiation and energy storage saturate once $L > 0.4\lambda$. It appears that the ground plane stops increasing the effective electrical size of the antenna system past this point. Ideally, bounds on Q as a function of ground plane size with fixed antenna volume could be used to corroborate this statement. However, as demonstrated here and in Chapter 6, the current state-of-the-art technique for bounding Q using the energy storage matrices breaks down due to the loss of positive-semi-definiteness in the energy storage matrices for structures larger than $\lambda/3$. Although Q can be calculated for currents on large structures, Q bounds can't be calculated for antenna volumes greater than this size using these kinds of techniques.

The asymptotic forms of the slot and dipole models can be made electrically small using equivalence principles. Interestingly, these two models show very different behavior of Q with respect to ground plane size, particularly in the small ground plane limit. The dipole is a much higher-Q system and shows increasing Q for small ground plane sizes, suggesting that the dominant radiation mechanism on this particular model carries with it high energy storage properties. On the other hand, the Q of the slot is lowered with increasing ground plane size in the small ground plane limit, indicating that the dominant radiation mechanism (i.e., the dipole moment of the ground plane) is able to radiate more per stored unit of energy as more material is added to the ground plane in this regime. Both models show convergence

toward the asymptotic infinite ground plane Q as L approaches 2λ.

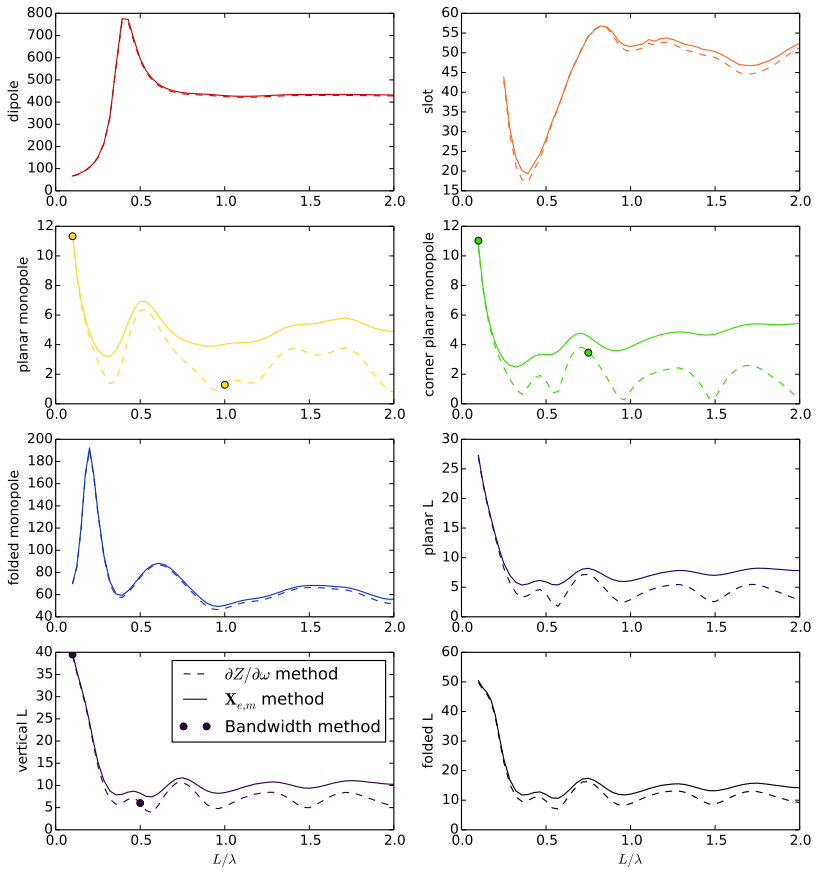

Figure 7.8: Radiation Q of each antenna type as a function of ground plane size L. All x-axes are L/λ.

7.6 Radiation mode convergence

Using the radiation mode eigenvalue problem

$$\mathbf{R}\mathbf{J}_i = \nu_i \mathbf{P}\mathbf{J}_i, \tag{7.4}$$

the total radiated power by a driven current distribution can be broken into modal contributions. By examining the (usually very sparse) set of modes

which contribute to radiated power, the radiating component of the driven current can be separated from the non-radiating component. The details of this procedure were previously described in Chapter 4. For each model, the modal radiated powers were calculated using this method. Because the physical geometry of each model changes as a function of L/λ, comparing individual radiation modes over this parameter is very difficult. In light of this, the modal radiated powers are presented in Figure 7.9 without association across L/λ. In Figure 7.9, each driven current was normalized to radiate unit power. Each dot represents the fractional power radiated by a given mode within the driven current distribution.

All of the models studied share several distinguishing features in their modal power spectra. In the small L/λ limit, one or two radiation modes account for nearly all of the radiated power. These modes gradually lose dominance as the ground plane size is increased. For most of the models studied here, this event occurs in the vicinity of $L/\lambda = 0.5$. In the corner-mounted models, two radiation modes are present in the extreme low L/λ limit. These are the two degenerate dipole modes acting as one diagonal dipole moment across the ground plane. Comparing the single-mode behavior with the Q in Figure 7.8, we see that the initial lowering (or raising, in the case of the dipole and folded monopole) of Q in the small L/λ limit appears to end as more radiation modes come into play, i.e., Q follows a monotonic trend while only one radiation mode represents most of the radiated power. In each model, the number of radiation modes continues to increase after one mode loses dominance, suggesting more complex and localized radiation mechanisms at at work. As more modes contribute to radiation, the statement that the ground plane is the dominant source of radiation becomes invalidated. With many modes present, the total radiating current begins to more closely resemble the driven current localized to the driven antenna element.

7.7 Summary and discussion

Though the actual lower bound on Q is not calculated, the above study of Q as a function of ground plane size demonstrates the consistency of a cutoff where adding more volume to the antenna ceases to improve bandwidth.

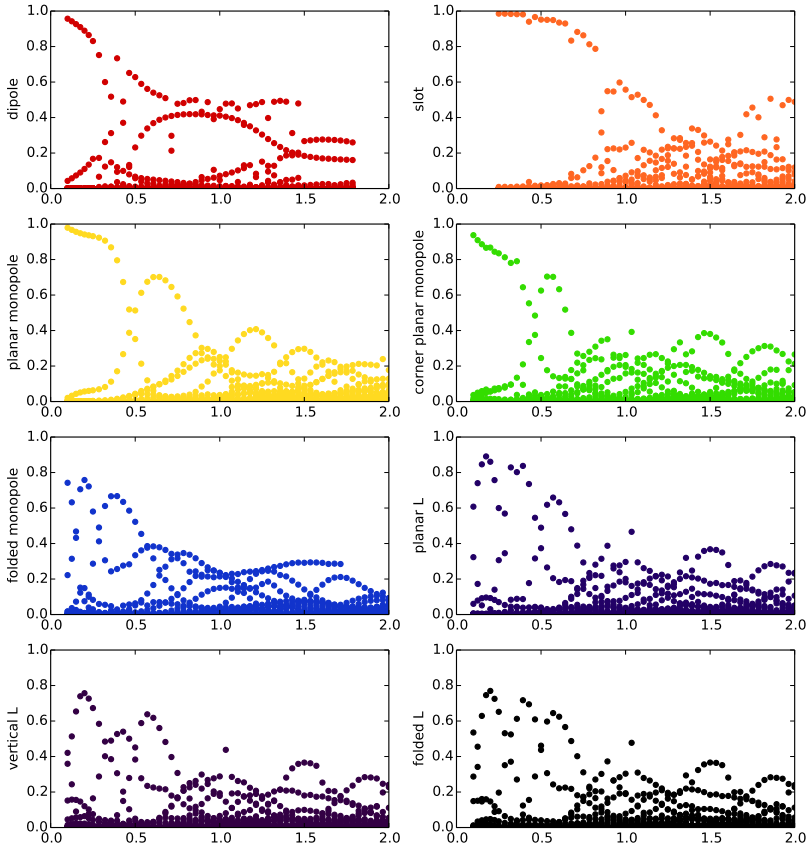

Figure 7.9: Radiation modal powers of each antenna type as a function of ground plane size L. All x-axes are L/λ.

This addresses the notion that electrically small elements on finite ground planes have effective electrical sizes encompassing some or all of the finite ground plane. Taking Q as a proxy for electrical size, this study shows that ground plane contributions to lowering bandwidth typically saturate between $L/\lambda = 0.4$ and $L/\lambda = 0.6$. These numbers may be specific to the square ground plane and base electrical size of the elements used here and further studies with general rectangular ground planes and varying sizes of antenna elements may return slightly different ranges.

The physical mechanism causing this saturation is clearly elucidated by the study of the modal radiated powers. In many of the examples studied, the saturation of Q with ground plane size correlates strongly with the loss

of single radiation mode behavior, suggesting that further increasing the ground plane size past this saturation point does not continue to increase the effective area of the simple radiating sources. Rather, the high number of radiation modes appearing after the saturation point represent the more complex modal currents required to synthesize the radiating current which is more and more localized (in comparison to the increasing scale of the ground plane) to the region near the driven antenna element. Thus, the ground plane only acts to directly modify the Q of the antenna system when the low-order radiation modes are being excited over the full support of the ground plane, i.e., when the ground plane effectively radiates like a simple dipole moment.

In many instances, the ground plane size or shape are not parameters which can be influenced by the antenna designer. Rather, a ground plane or conducting chassis is assigned to a device onto which an antenna must be mounted within an allocated design volume. Though the data from the Q and radiation mode analyses will change based on the specific antenna and ground plane geometries at hand, the data from this chapter can be used to develop *a priori* intuitions as to the physical mechanisms governing radiation and bandwidth for a given embedded antenna design template. For example, a small corner mounted planar L antenna on a cell-phone sized device will have a ground plane (in the form of the conducting phone chassis) of approximately $0.3\lambda \times 0.2\lambda$ at 850 MHz. From the data in Figures 7.8 and 7.9, it is apparent that we can expect the dipole moment of the ground plane to be the dominant source of radiation and that the bandwidth of the system will depend heavily on both the antenna element and the given ground plane size. In a different scenario, the same antenna may be placed on a tablet sized device and tuned for operation near 2.45 GHz. In this setup, the ground plane on the order of 2λ. Again, referring to Figures 7.8 and 7.9 we would expect that the localized currents on and around the antenna element will be the primary effective radiators and determinants of bandwidth. In this way, the study in this chapter provides guidelines for physical mechanisms governing embedded antenna systems which may inform both their design and specification expectations.

CHAPTER 8

BEAMFORMING USING THE RADIATION MODES OF FINITE GROUND PLANES

8.1 Overview

Radiation modes are used as a basis for determining the optimum current for a pattern-specification problem. Using this technique and leveraging the invariance of radiation modes with respect to geometry perturbations, a straightforward parametric study is used to design a two-element null steering array mounted on a $0.3\lambda \times 0.18\lambda$ rectangular plate.

8.2 Pattern specification methods

An pattern specification problem is one in which an antenna is designed such that its realized power pattern, $|f^\gamma|^2$ best approximates some desired power pattern $|g^\gamma|^2$. Throughout this chapter, the superscript γ denotes a particular choice of polarization. Many metrics can be constructed to quantify the relative error between the realized and specified patterns. One simple metric is a weighted squared-error integration over the farfield sphere, i.e.,

$$\epsilon = \int_\Omega (|f^\gamma|^2 - |g^\gamma|^2) w d\Omega, \tag{8.1}$$

where Ω denotes the farfield sphere and w is a weighting function. In (8.1), f is the field radiated by the designed antenna. Abstractly, a pattern-specification design procedure should be an ordered set of steps laid out to minimize ϵ within some constraints. There are many existing approaches to this type of problem, each with strengths and weaknesses. Two such methods are discussed here, along with proposed modifications for the use of the radiation mode set developed in previous chapters.

8.2.1 Array perspective

Consider an array designed with N elements, each with active element field patterns f_n^γ and driven with an excitation coefficient β_n. Assuming the array design itself is fixed, the set of excitation coefficients $\boldsymbol{\beta}$ which minimizes the design error term ϵ can be obtained by solving the optimization problem

$$\tilde{\boldsymbol{\beta}} = \arg\min_{\boldsymbol{\beta}} \int_\Omega (|\sum_n^N \beta_n f_n^\gamma|^2 - |g^\gamma|^2) w d\Omega. \tag{8.2}$$

In this problem, there are $2N$ unknowns in the real and imaginary components of $\boldsymbol{\beta}$. Assuming a global solution to the above problem is found, the design procedure is finished. If the solution has insufficiently low design error (i.e., the designed array pattern does not sufficiently match the specified pattern), then some changes must be made to the physical design of the array in order to alter the active element patterns f_n^γ. From this approach, little insight is gained by the solution of the above problem which could inform which design modifications would enable or inhibit improvement of the design error. This detriment is offset by the simple nature of the above optimization problem and its relatively low number of unknowns.

8.2.2 Full current optimization

As discussed in previous chapters, the mapping between a current and its radiated field is linear. Denoting the map from a current onto its farfield pattern in a given polarization as $\hat{F}^\gamma$, the current which best approximates the specified pattern is given by the optimization

$$\tilde{J} = \arg\min_{\vec{J}} \int_\Omega (|\hat{F}^\gamma \vec{J}|^2 - |g^\gamma|^2) w d\Omega. \tag{8.3}$$

Assuming some surface is specified as the support of the current, $\vec{J}$, the discrete method of moments notation for this problem is

$$\tilde{\mathbf{J}} = \arg\min_{\mathbf{J}} \sum_m^M (|\mathbf{F}^\gamma \mathbf{J}|_m^2 - |g^\gamma|_m^2) w_m, \tag{8.4}$$

where $\mathbf{F}^\gamma$ is the matrix mapping a current to its farfield pattern at M sampling locations. In the above expressions g and w are also assumed to be

sampled at those same locations, denoted by the subscript m. Written in this way, the above problem closely resembles the class of problems studied in [13], where bounds on certain antenna parameters were studied in terms of the structure on which current was allowed to exist. There however, variants of the above current optimization were used such that the problem was tightly constrained by energy storage and pattern specification was limited to single directions and polarizations. These modifications have the advantage of linearizing the power pattern fitting cost, but come at the expense of limited applicability to multi-angle pattern specification. As written above, the design error function is unbounded in the sense that the current deemed optimum could be arbitrarily complex within the K basis functions used to express $\mathbf{J}$. This high number of unknowns ($2K$) as well as the lack of any guarantee that the optimum $\mathbf{J}$ would be physically realizable makes this form of the pattern specification problem very ill-posed. However, a redeeming quality of this approach is that the optimization is done in terms of physical currents, which could conceivably inform the iterative design alterations required to realize those currents on an antenna.

8.2.3 Sparse modal current representations

The array approach to pattern specification is well constrained and has a small number of unknowns. However, the lack of feedback or useful insight from the optimization of excitation coefficients makes it weak when the array itself (elements, spacings, etc.) need to be designed from scratch. In contrast, the full current optimization technique returns currents on a predetermined surface which a designer may then try to match to the driven currents on a physical antenna through informed design iterations. The main disadvantage of the full current optimization technique is its lack of constraints and arbitrarily high number of unknowns.

Using a modal current model, the advantages of both methods are leveraged. Starting with the full current optimization method, the number of unknowns can be reduced by restricting the current $\mathbf{J}$ to a linear combination of a set of P predefined modal currents, i.e.,

$$\mathbf{J} = \sum_{p}^{P} \alpha_p \mathbf{J}_p = \mathbf{\Phi}\boldsymbol{\alpha}, \tag{8.5}$$

where $\mathbf{\Phi}$ is a matrix containing the P modal currents $\mathbf{J}_p$ as columns and $\boldsymbol{\alpha}$ is a vector containing the complex modal excitations α_p. Inserting this form of $\mathbf{J}$ into the full current optimization problem yields

$$\tilde{\boldsymbol{\alpha}} = \arg\min_{\boldsymbol{\alpha}} \sum_{m}^{M} (|\mathbf{F}^{\gamma}\mathbf{\Phi}\boldsymbol{\alpha}|_m^2 - |g^{\gamma}|_m^2) w_m. \tag{8.6}$$

With this modification the problem is still one of optimizing a current but with added constraints on which types of currents can be used. The advantage of this is twofold. First, the number of unknowns can be greatly reduced, forcing the system to look more like that of the array coefficient optimization method. Second, the complexity of the current synthesized can be directly controlled by choice of the modal basis $\{\mathbf{J}_p\}$. By choosing a modal basis consisting of well-behaved, potentially realizable currents, the designer can automatically exclude optimized current distributions which, though they may generate very low pattern match error, are completely unattainable.

8.3 Selection of modal basis

To use the modal basis form of the pattern matching optimization problem, a set of basis currents must be chosen. Previously these were referred to as *modal currents*, though in reality the basis need not be constructed of any truly modal quantities. In order to best take advantage of the modal form of the pattern matching problem, the basis set should be chosen such that the basis currents do the following:

- Represent unique radiation characteristics. Full pattern orthogonality is not necessary, but it does ensure linear addition of powers radiated by the individual currents.
- Can constrain the complexity of the total optimized currents. Ideally the basis would be chosen such that the number of modes used, P, has direct control over the complexity of the optimized currents, e.g., raising P allows for more complex solutions.
- Change little with perturbations to the starting surface. In practice, antennas are modified through each design iteration, effectively perturbing the surface over which the current optimization is performed.

Ideally, the modal basis would change little through each of these perturbations.

Two candidate basis sets studied here are characteristic modes and radiation modes. Other modal sets, such as Inagaki modes [68, 69] may also be used but their discussion is omitted here. Both sets are generated by eigenvalue problems governed by the surface on which current is allowed to exist, i.e., a conducting design. Within each eigenvalue problem, both sets of modes have the property

$$\mathbf{J_i}^T \mathbf{R} \mathbf{J_j} = \delta_{ij}, \tag{8.7}$$

meaning that the powers radiated by each mode add linearly. By this property, it follows that the modal farfields must be orthogonal as well, i.e.,

$$(\mathbf{F}^\gamma \mathbf{J})_i^T \, \mathbf{F}^\gamma \mathbf{J}_j \approx \delta_{ij}, \quad \forall \gamma. \tag{8.8}$$

The approximation in the above expression becomes exact as the number of sampling points in the farfield matrix $\mathbf{F}^\gamma$ becomes infinite. Thus, both characteristic modes and radiation modes satisfy the condition of having unique radiation patterns. Similarly, it is well known (e.g., [9, 70]) that characteristic modes typically form a sparsely-excited set and represent relatively simple current distributions. In the previous chapters, this was also shown to be true of radiation modes. The key distinction between the two modal sets is the inclusion or omission of energy storage properties. Characteristic modes include the matrix operator related to net reactive energy, $\mathbf{X}$, while the radiation mode problem does not. The inclusion of $\mathbf{X}$ in the characteristic mode eigenvalue problem gives rise to several important features of that expansion technique, such as the convenient forms of modal impedances and excitation coefficients. However, this inclusion also ties the solutions of the characteristic mode problem to the highly-geometry dependent mechanisms of energy storage. This leads to characteristic modal currents changing drastically with small perturbations to the surface being studied. In Chapter 4, it was shown that radiation modal currents and eigenvalues have very weak dependence on the fine-scale features of an object, depending mainly on the total support or surface area. This difference in geometry sensitivity is demonstrated in Figure 8.1, where a characteristic mode and radiation mode are shown

for a rectangular plate before and after the addition of a small geometrical perturbation. The radiation mode is largely unchanged by the perturbation whereas the characteristic mode is significantly altered in the region near the change in geometry.

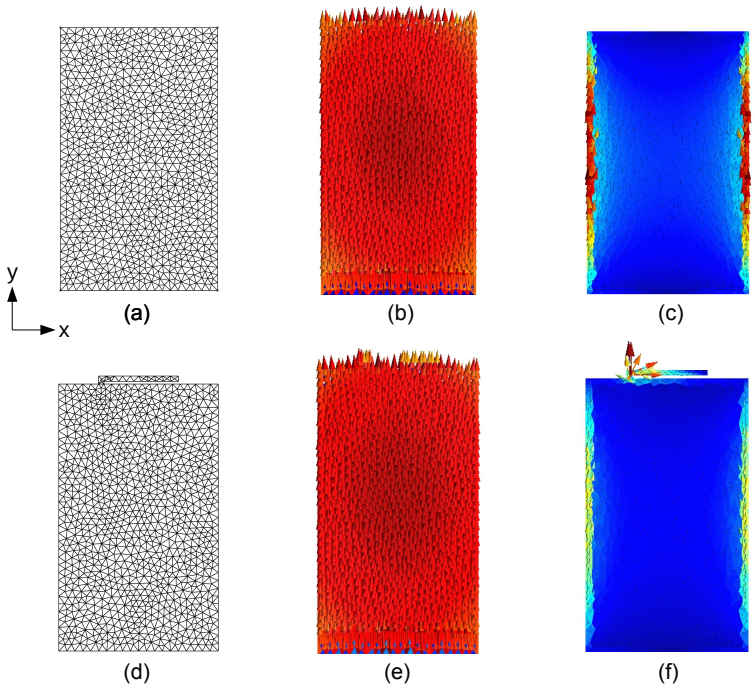

Figure 8.1: Mesh (left), example radiation mode (middle), and example characteristic mode (right) of a $0.3\lambda \times 0.18\lambda$ rectangular plate with (bottom row) and without (top row) a small perturbation.

With these considerations of the conditions outlined above, radiation modes seem best fit for the pattern specification optimization problem. If, in addition to pattern specification, impedance or resonance properties were also required, then a hybrid technique involving both characteristic modes and radiation modes may be necessary.

8.4 Solving the modal pattern specification optimization problem

To demonstrate the procedure, an example is constructed where the goal is to create a two-element null-steering array mounted on a cell-phone-sized

rectangular conducting plate. This example is motivated by the scenario where a desired link (e.g., between a mobile user and a base station) is governed by Raleigh scattering [71]. In this mobile scenario, link performance is typically improved by adding antenna diversity to statistically reduce the number of outages caused by destructive interference or shadowing [72, 73]. Analysis and design of diversity antennas has been explored through many means; popular methods include optimization of pattern envelope correlation coefficients [74], though measurements often show drastically different enhancements in performance depending on the specific scattering milieu, e.g., [75, 76]. While this diversity approach works well to improve the base-station/mobile link, the mobile user may be susceptible to interference by other users on the same band by predominately line-of-sight, or Rician, mechanisms [71]. In this example, the goal is to create a null steering array on a small mobile platform to selectively reduce this kind of line-of-sight interference. This example was first presented in [77].

The rectangular plate, or chassis, is 0.06 m $\times$ 0.1 m. At the cellular communications band near 900 MHz, the chassis is $0.18\lambda \times 0.3\lambda$. Using the impedance matrix of the chassis and the radiation eigenvalue problem

$$\mathbf{R}\mathbf{J}_i = \nu_i \mathbf{P}\mathbf{J}_i, \tag{8.9}$$

the radiation modal currents and eigenvalues are calculated. The leading-order radiation modes of the chassis are shown in Figure 8.2. As predicted by the expressions derived in Chapter 4, the dominant three radiation modes are two quasi-degenerate dipole modes (labeled Modes 1 and 2) and an electric loop, or magnetic dipole moment (labeled Mode 3). Higher-order modes resemble multipoles. Because the radiation mode spectrum is very sparse, only a few modes should realistically be included in the basis for the modal optimization problem. This does not imply that the total current on a finished design must match the optimized linear combination exactly. Rather, the radiating component of the total current must match the optimized linear combination of radiation modes. The non-radiating component is defined as consisting of currents lying in or near the null-space of $\mathbf{R}$ and will not affect the overall radiation pattern.

In this example, the desired radiation pattern $|g^\gamma|^2$ depends on the null steering parameter Ω_{null}. For simplicity, only the yz-cutplane and θ polar-

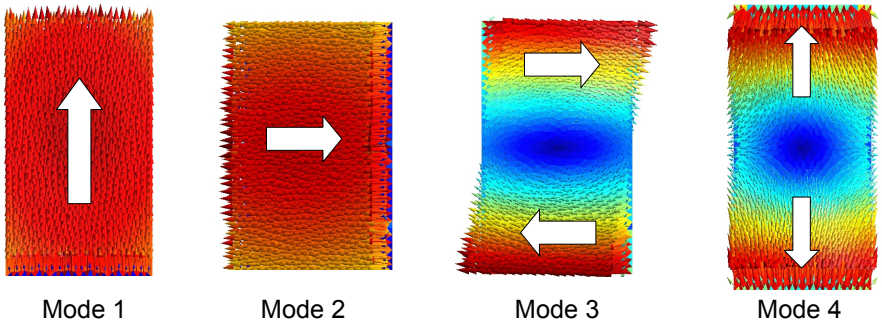

Figure 8.2: First four radiation modes of a 0.18 x 0.3 λ rectangular plate.

ization is considered, such that $\Omega_{\text{null}} = \theta_{\text{null}}$ and $\gamma = \theta$. Taking advantage of the symmetry of the problem, Ω_{null} ranges from 0^o (endfire direction) to 90^o (broadside direction). To specify a null at Ω_{null} while maintaining a uniform pattern elsewhere, the following goal function is used,

$$|g^{\theta}|^2(\Omega, \Omega_{\text{null}}) = 1 - \delta(\Omega - \Omega_{\text{null}}). \tag{8.10}$$

To enforce priority of the null as opposed to an unrealistic isotropic pattern, the weight function w is chosen as

$$w(\Omega, \Omega_{\text{null}}) = 1 + 100\delta(\Omega - \Omega_{\text{null}}). \tag{8.11}$$

Thus we expect to obtain a set of optimized radiation mode coefficients $\tilde{\boldsymbol{\alpha}}(\Omega_{\text{null}})$ by solving at (8.6) each null steering angle Ω_{null} using the above goal and weight functions. The matrix $\mathbf{F}^{\theta}$ is constructed to map currents on the chassis to a radiated farfield in the θ polarization at 91 evenly spaced angles between 0^o and 90^o within the yz-cutplane. The null-steering angle is swept through all 91 of these values, leading to 91 instances of $\tilde{\boldsymbol{\alpha}}$ from the same number of optimizations of (8.6).

The non-linear optimization problem in (8.6) can be solved by a number of methods. Here a basic gradient-descent algorithm [57] is used. To avoid local minima and to assess the repeatability of the optimization solution, multiple random initializations of $\boldsymbol{\alpha}$ are used at each instance of Ω_{null}. Regularization is done *post hoc* by iteratively removing modes whose presence in the optimized solution minimally affects the minimal error value ϵ. In this example, P was initially set to 10, but through regularization the basis was reduced

such that only Modes 1 and 4 (see Figure 8.2) remained. To account for the arbitrary normalization of the excitation coefficients and radiation patterns, α_1 was fixed to unity. Figure 8.3 shows the optimized modal coefficients as functions of null steering angle. The optimized patterns for selected values of Ω_{null} are drawn in Figure 8.4.

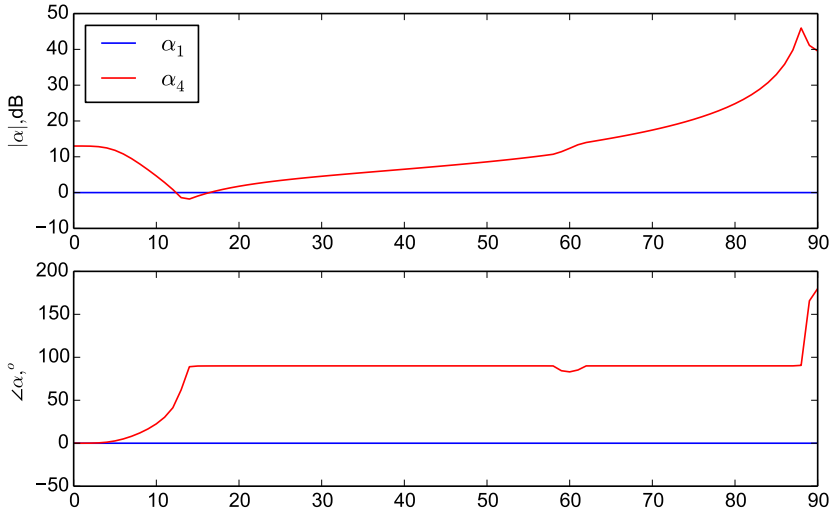

Figure 8.3: Amplitude (top) and phase (bottom) of modal coefficients optimized as functions of Ω_{null}. α_1 is fixed at $1\angle 0^o$.

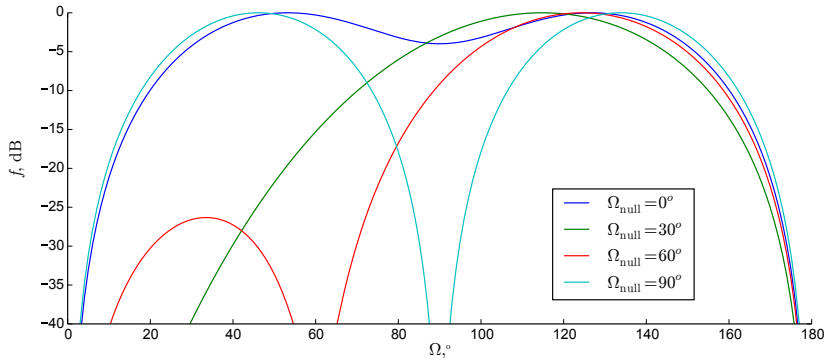

Figure 8.4: Radiation patterns optimized for nulls at $\Omega_{\text{null}} = 0^o, 30^o, 60^o$ and 90^o. Amplitude shown in dB re: pattern maximum.

The optimized modal coefficients have a maximum dynamic range of 47 dB. The intermodal phasing is under 90^o, except in the case of near-broadside

null steering. Near broadside, Mode 4 becomes very dominant, and intermodal phasing can be relaxed. Limiting the null steering to 80^o decreases the dynamic range to 25 dB. The resulting patterns clearly display a null in the specified direction when $\Omega_{\text{null}} > 30^o$. When the null is steered closer to the endfire direction, the pattern consists of one tipped lobe.

8.5 Heterogeneous antenna design

Two antenna elements must now be designed to excite the modal coefficients as specified by the optimization procedure. It is assumed that some amplitude and phase control will be implemented on at least one of the antennas to enable null scanning. In this example, two antennas will be used and two modes are required for the specified performance with coefficients determined as functions of the null steering as calculated in the previous section. Denoting the two antenna elements with subscripts A and B, the active element current on both antennas produce modal excitation coefficient vectors $\boldsymbol{\alpha}^A$ and $\boldsymbol{\alpha}^B$. To minimize the required phase shift and dynamic range of the scanning components, the antennas should be designed such that these vectors span the space of modal excitation coefficients, i.e., the antennas' modal excitations of Modes 1 and 4 should be as different as possible. This suggests using heterogeneous elements. Because the structure and behavior of radiation modes is relatively invariant with small perturbations to the base geometry, modal ratios can be fairly compared between models.

The antenna designs are restricted to the two opposite short edges of the ground plane. Three simple edge-mounted, planar antennas are chosen as candidates for this design, shown in Figure 8.5. None of the geometries are optimized for impedance match. A parametric study of modal excitations as functions of the feed location is run for each antenna to determine the best combination of antennas and feeds for diversity in Modes 1 and 4. The feed is displaced from 0.00 m (corner) to 0.03 m (center). Figure 8.6 displays the relative magnitude, $|\alpha_4/\alpha_1|$, and phase $\angle(\alpha_4/\alpha_1)$ of the Mode 1 and 4 excitation coefficients at each trial feed displacement. All three antenna topologies have modal magnitude ratios between -4 and -7 dB. The magnitude ratio changes slightly between the models, as does its dependence on feed displacement. Intermodal phasing stays constant with feed location

and changes only by a few degrees between antenna types.

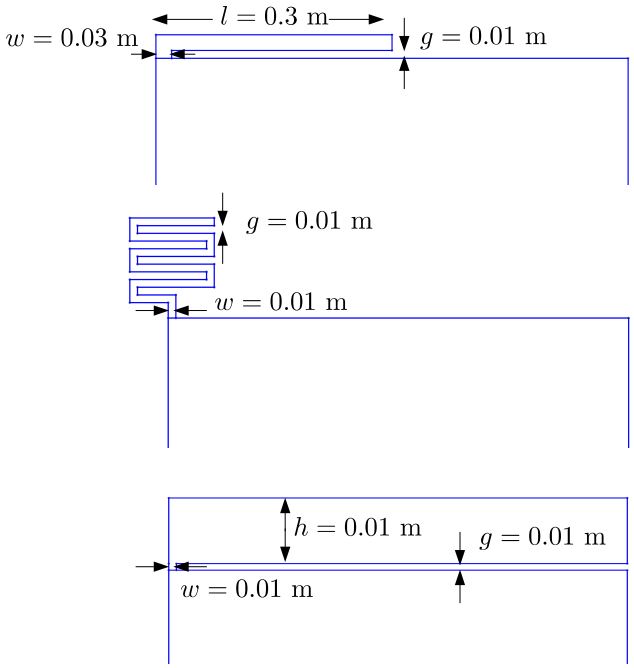

Figure 8.5: Planar L (top), meander monopole (middle), and plate monopole (bottom) antenna prototypes. All antennas shown with zero feed displacement, i.e., antennas mounted at the corner of the ground plane.

Using these data, two antennas are selected for maximum modal phase and amplitude difference. Antenna A is assigned as a meander monopole with feed offset of 0.02 m. Antenna B is a plate monopole with no feed displacement. The combined system is shown in Figure 8.7. Up until this point, both antennas have been considered in isolation. To examine the effects of mutual coupling on the radiation mode excitation coefficients, the active element current of each antenna was evaluated by driving the elements separately with the non-driven antenna terminated with a 50 Ω load [2]. The individual and combined modal excitations for each antenna are listed in Table 8.1. With mutual coupling included in this particular example, the antennas maintain their diverse relative modal magnitudes but now have nearly identical intermodal phasing. This suggests that in future design cycles modal diversity should be evaluated with the whole system intact, as opposed to separately on individual elements. This modification to the design methodology is discussed further at the end of the chapter.

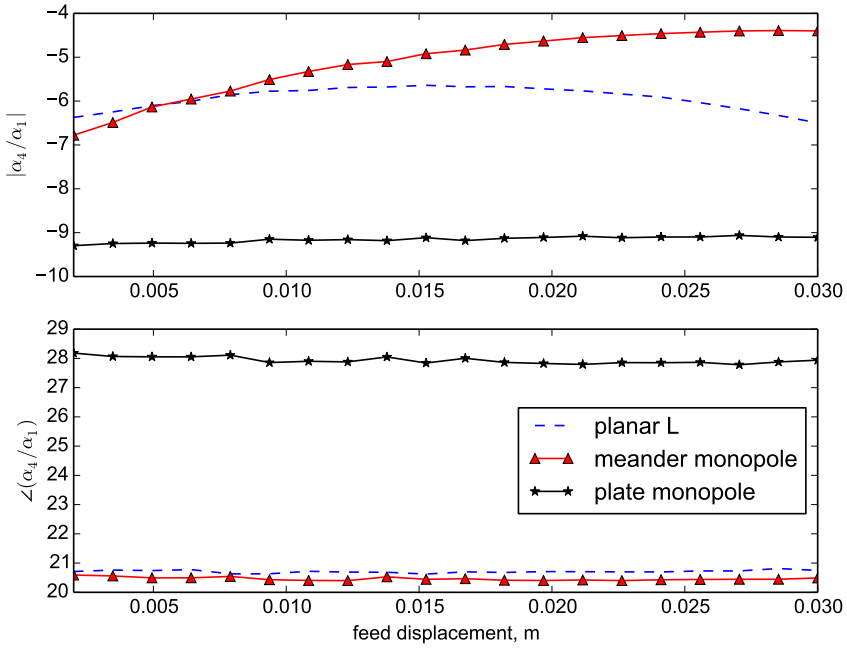

Figure 8.6: Relative excitation magnitude (top) and phase (bottom) of Modes 1 and 4 as a function of feed displacement location evaluated for the three antenna types shown in Figure 8.5.

To steer a null using this two-antenna configuration, the proper antenna excitation ratios must be determined at each null-steering angle. Using the antenna radiation mode coefficient (column) vectors $\boldsymbol{\alpha}^A$ and $\boldsymbol{\alpha}^B$, the antenna excitations $\beta^A(\Omega_{\text{null}})$ and $\beta^B(\Omega_{\text{null}})$ are given by

$$\begin{bmatrix} \beta^A(\Omega_{\text{null}}) \\ \beta^B(\Omega_{\text{null}}) \end{bmatrix} = \begin{bmatrix} \boldsymbol{\alpha}^A & \boldsymbol{\alpha}^B \end{bmatrix}^{-1} \begin{bmatrix} \boldsymbol{\alpha}(\Omega_{\text{null}}) \end{bmatrix}, \tag{8.12}$$

where $\boldsymbol{\alpha}(\Omega_{\text{null}})$ is the column vector of modal coefficients previously calculated by the pattern-fitting optimization procedure. The results of this calculation are shown in Figure 8.8 where the antenna driving voltages β^A and β^B have been normalized to radiate constant at all null steering angles. All excitation magnitudes are further normalized to the same global maximum, for clarity. The phase of β_A is fixed at 0^o.

Covering the entire range of null scan angles requires approximately 10 dB and 20 dB of gain control on antennas A and B, respectively. Upwards of 80^o of phase variation on antenna B is also required. Most of these ranges

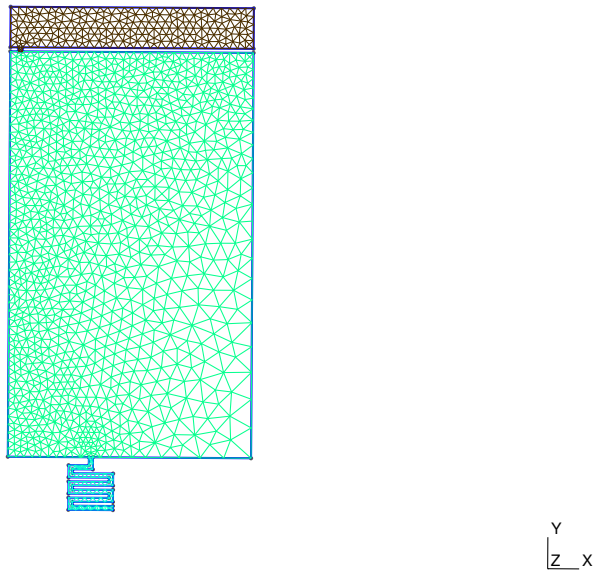

Figure 8.7: Combined antenna system. Antenna A, a meander monopole with 0.02 m feed displacement is located at the bottom of the ground plane. Antenna B, a plate monopole with no feed displacement is located at the top.

come from the span of $10^o < \Omega_{\text{null}} < 30^o$. Abandoning null steering within this range reduces the gain controls to less than 10 dB on both antennas, while reducing the required phase span on antenna B to approximately 40^o. In practice, a small device would likely not contain the circuitry required for precise null steering but rather would use reconfigurable circuitry to define a discrete set of pattern configurations.

8.6 Summary and future improvements

The design of the two element null-steering array in this chapter demonstrates the applicability of using radiation modes as proxy objectives for pattern-specification design problems. Using the modal current optimization objective keeps the number of unknowns involved in pattern optimization to a minimum while maintaining a physical picture of radiation mechanisms. This is particularly useful for antennas mounted on ground planes and con-

Table 8.1: Relative modal magnitude and phasing of both antennas calculated individually and within the combined system

	Individual $\lvert\alpha_4/\alpha_1\rvert$	Individual $\angle(\alpha_4/\alpha_1)$	Combined $\lvert\alpha_4/\alpha_1\rvert$	Combined $\angle(\alpha_4/\alpha_1)$
Antenna A	-4.63 dB	20.40^o	-3.44 dB	39.92^o %
Antenna B	-9.29 dB	28.18^o	-9.97 dB	39.77^o %

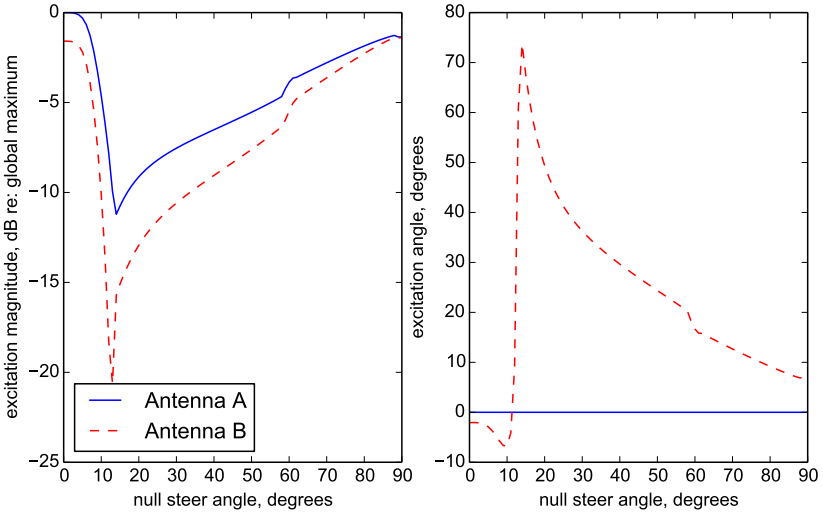

Figure 8.8: Antenna excitations β_A and β_B as functions of null-steering angle Ω_{null}. Excitation magnitudes are normalized to a global maximum and result in constant total radiated power over all steering angles.

ducting chassis, where the dominant sources of radiation are ground plane currents, not the antenna elements themselves. While characteristic modes have many useful properties, the lack of energy storage involvement in the calculation of radiation modes makes them less of a "moving target" when making small alterations to a structure (as illustrated in Figure 8.1).

The design example in this chapter consists of two main components: calculating the optimized radiation mode coefficients for achieving specific patterns, and designing antennas to best implement those modal combinations. The gradient descent method proved to be a fast, reliable way of solving the non-linear modal pattern optimization problem. In designing the antenna elements, a simple parametric study of three antenna types was used. For smaller, tuned antennas with specific impedance properties, radiation mode objectives could be combined with the geometry optimization techniques in

[16]. The fact that radiation modes are invariant to geometry changes on small objects make them powerful in comparing optimized antenna geometries, and could be combined with characteristic modes for efficient automated design of resonant, pattern-specified embedded antennas [42].

The presence of terminated ports in the multi-antenna system in this chapter results in significant mutual coupling which altered the effective modal excitations of the individual antenna elements. This suggests that radiation mode excitations should be evaluated within a complete system, not for individual antenna elements in isolation. To accomplish this, subdomain characteristic mode techniques [15] may be useful in expediting the calculation of active element currents in a multi-antenna system.

CHAPTER 9

CONCLUSIONS AND FUTURE WORK

9.1 Summary of findings

The goal of this research was to study the mapping between current distributions on conducting objects and antenna design deliverables such as bandwidth, radiation patterns, and efficiency. Instead of working directly with these engineering metrics, we studied the intermediate mapping of currents to radiated power an energy storage, as all antenna parameters ultimately arise from these quantities. Through the study of those mappings, the role of current mechanisms in manifesting antenna design metrics (bandwidth, radiation pattern, etc.) is made more approachable. An application area benefiting from this kind of analysis is embedded antennas, or small antennas near larger conducting bodies. As such, this class of systems were the focus of the later chapters of this dissertation.

The approach used in existing source-based analyses was summarized in Chapter 2, laying the groundwork for the novel radiation and energy storage mode expansions implemented throughout the dissertation using the numerical techniques outlined in Chapter 3. The mathematical properties of the matrix operators related to radiation and energy storage were used to draw conclusions about the physical mechanisms responsible for these quantities in practical antenna systems. The null space of the radiation matrix enables the separation of radiating and non-radiating currents. This null space also indicates the sparsity of radiation mechanisms and the presence of a large class of currents which can be arbitrarily added to a system with no consequence to radiation properties. In contrast, the lack of a large null space in the energy storage operators doesn't allow for a contributing / non-contributing separation, but modal mechanisms can still be identified. Radiation mode expansion facilitates the quantification of radiation sources in embedded an-

tennas, enabling quantification of the assumption that small ground planes are dominant sources of radiation in such systems, as demonstrated in Chapter 4.

In Chapter 5, it was shown via analytic means that radiation modes represent a fast method for calculating the low-order multipole moments of arbitrary currents and structures. The analytic study carried out in Chapter 5 also corroborates empirical observations regarding the invariance of radiation modes on electrically-small objects. As a current expansion basis, radiation modes provide a convenient way to describe and quantify radiation patterns during the design of embedded antennas due to this inherent invariance. This finding was used in Chapter 8, where radiation modes on a ground plane were used as a basis for pattern specification. The procedure for using a modal current expansion for the design of pattern-specified antennas has been previously reported in several capacities, but in this dissertation the advantages of radiation modes over characteristic modes was explicitly illustrated; namely, radiation modes' geometry invariance.

In Chapter 7, the behavior of ground plane radiation was linked to changes in quality factor and bandwidth by using radiation mode expansion. The dependence of Q (and by proxy bandwidth) with ground plane size was observed to correspond with the transition from single- to multi-mode radiation behavior. Generally speaking, this transition indicates the threshold where a larger ground plane ceases to increase effective electrical size, and thus ceases to improve bandwidth performance. This information can be used to provide a designer with *a priori* expectations which components in an embedded system will govern and bound radiation and bandwidth properties.

The loss of positive-semi-definiteness is a known issue preventing the calculation of Q bounds by convex optimization on larger structures. By using the energy storage eigenmode expansions, the current distributions associated with this loss of positive-semi-definiteness were isolated and characterized. The results from this analysis show that not only are negative energy modes simple in nature, they tend to represent fundamental radiating mechanisms. Characteristic modes of simple objects are also shown to produce negative energies. The combined data from Chapter 6 and 7 demonstrate that, while the loss of positive-semi-definiteness makes bounding Q by existing means impossible, the calculation of Q via the energy storage operators matches closely with "ground truth" values obtained by impedance or band-

width means for electrically large objects with $Q > 20$; even when the energy storage matrices are non-positive-semi-definite. This suggests that the loss of positive-semi-definiteness on large structures does not necessarily mean inaccurate results for Q calculations on high-Q systems.

9.2 Added engineering intuition

While this research focuses heavily on abstract problems, the mathematical and physical results can be synthesized into several useful additions to engineering intuitions.

The difference in matrix properties of radiation and energy storage operators elucidates interesting physical properties of electric currents. The large null space of the radiation matrix can be interpreted as allowing a large class of currents which do not radiate. In contrast, the lack of a null space of the energy matrices dictates that all currents must store energy. This confirms the concept that there exist many currents, particularly of those of electrically small support, which radiate in the same manner; leading to the conclusion that there exist many added degrees of freedom when designing an antenna with particular radiation properties. In other words, the radiating component of a current can be combined with any arbitrary non-radiating current with no effect on the radiation properties of the system. This is particularly interesting in the design of embedded antennas, where colloquially the antenna acts as a matching network and the ground plane is understood to be the dominant radiator. Using radiation mode expansion, this sort of ground plane radiation is quantified in a novel way. Later chapters of this dissertation explored the ground plane / element relations in terms of bandwidth (Q), radiation patterns, and negative energy storage; demonstrating how these expansions can be used on a variety of electromagnetic problems.

9.3 Open questions and future work

The development of radiation and energy storage modes and the findings in the later chapters of this dissertation leave many possibilities for future investigations.

Combining the pattern specification technique in Chapter 8 with the automated resonant embedded antenna design procedure described in the literature adds a dimension of control and efficiency to the field of automated antenna geometry synthesis. The use of radiation modes as an expansion basis in conjunction with automated design algorithms (e.g., genetic algorithm geometry optimization) may enable the bounding of radiation pattern complexity on embedded antennas. Continuing the work done in Chapter 8 on multi-port embedded MIMO antennas in the context of effective efficiency, bit-error-rate (BER) and other system-level metrics will help connect the physical concepts involved with radiation mode expansion to practical antenna design.

Further study on the validity of the energy storage matrices for calculating Q on large structures is required. From the results in Chapter 6 it appears that the loss of positive-semi-definiteness doesn't degrade the accuracy of Q calculations of high-Q currents. Further investigation via measurement of projections of negative energy modes in driven currents would help determine intuitive guidelines for the applicability of these methods, even when optimization Q-bounds are intractable. Explorations of the transient properties of currents represented by negative energy modes would also help connect these seemingly anomalous occurrences with physical phenomena.

The study of radiation modes, impedance, and Q in Chapter 7 spanned many antenna types, but did not explore in detail the effect of small design changes. A more in-depth examination of radiation mode convergence properties may aid in classifying antenna structures (e.g., PIFAs, loaded loops) which benefit from careful tailoring of ground plane size and could unify the conflicting or seemingly disparate results reported in the literature.

REFERENCES

[1] "IEEE standard for definitions of terms for antennas," *IEEE Std. 145-2013*, pp. 1–50, 2014.

[2] W. L. Stutzman and G. A. Thiele, *Antenna Theory and Design*. Hoboken, NJ: John Wiley and Sons, 2013.

[3] C. A. Balanis, *Antenna Theory: Analysis and Design*. Hoboken, NJ: John Wiley and Sons, 2005.

[4] C. Rowell and E. Y. Lam, "Mobile-phone antenna design," *IEEE Antennas and Propagation Magazine*, vol. 54, no. 4, pp. 14–34, 2012.

[5] S. R. Best, "The significance of ground-plane size and antenna location in establishing the performance of ground-plane-dependent antennas," *IEEE Antennas and Propagation Magazine*, vol. 51, no. 6, pp. 29–43, Dec. 2009.

[6] M. Capek, "Modal analysis and optimization of radiating planar structures," Ph.D. dissertation, Czech Technical University in Prague, 2014.

[7] R. F. Harrington and J. R. Mautz, "Theory of characteristic modes for conducting bodies," *IEEE Trans. on Antennas and Propagation*, vol. 19, no. 5, pp. 622–628, Sept. 1971.

[8] R. J. Garbacz and R. Turpin, "A generalized expansion for radiated and scattered fields," *IEEE Trans. on Antennas and Propagation*, vol. 19, no. 3, pp. 348–358, May 1971.

[9] M. Cabedo-Fabres, E. Antonio-Daviu, A. Valero-Nogueira, and M. F. Bataller, "The theory of characteristic modes revisited: A contribution to the design of antennas for modern applications," *IEEE Antennas and Propagation Magazine*, vol. 49, no. 5, pp. 52–68, Oct. 2007.

[10] G. A. E. Vandenbosch, "Reactive energies, impedance, and Q factor of radiating structures," *IEEE Trans. on Antennas and Propagation*, vol. 58, no. 4, pp. 1112–1127, Apr. 2010.

[11] G. A. E. Vandenbosch, "A simple procedure to derive lower bounds for radiation Q of electrically small devices of arbitrary topology," *IEEE Trans. on Antennas and Propagation*, vol. 59, no. 6, pp. 2117–2224, June 2011.

[12] M. Gustafsson and S. Nordebo, "Optimal antenna currents for Q, superdirectivity, and radiation patterns using convex optimization," *IEEE Trans. on Antennas and Propagation*, vol. 61, no. 3, pp. 1109–1118, Mar. 2013.

[13] M. Gustafsson, "Convex optimization for analysis of small antennas," *EUCAP*, pp. 437–438, 2013.

[14] M. Cismasu and M. Gustafsson, "Antenna bandwidth optimization with single frequency simulation," *IEEE Trans. on Antennas and Propagation*, vol. 62, no. 3, pp. 1304–1311, Mar. 2014.

[15] J. L. T. Ethier and D. A. MacNamara, "Sub-structure characteristic mode concept for antenna shape synthesis," *Electronics Letters*, vol. 48, no. 9, Apr. 2012.

[16] J. L. T. Ethier and D. A. MacNamara, "Antenna shape synthesis without prior specification of the feedpoint locations," *IEEE Trans. on Antennas and Propagation*, vol. 62, no. 10, Oct. 2014.

[17] S. R. Best, "Low Q electrically small linear and elliptical polarized spherical dipole antennas," *IEEE Trans. on Antennas and Propagation*, vol. 53, no. 3, pp. 1047–1053, Mar. 2005.

[18] J. J. Adams and J. T. Bernhard, "A modal approach to tuning and bandwidth enhancement of an electrically small antenna," *IEEE Trans. on Antennas and Propagation*, vol. 59, no. 4, pp. 1085–1092, Apr. 2011.

[19] J.-M. Jin, *The Finite Element Method in Electromagnetics*, 2nd ed. Hoboken, New Jersey: Wiley, 2002.

[20] L. J. Chu, "Physical limitations on omni-directional antennas," *J. Appl. Physics*, vol. 19, pp. 1163–1175, Dec. 1948.

[21] M. Capek, L. Jelinek, and P. Hazdra, "On the functional relation between quality factor and fractional bandwidth," *IEEE Trans. on Antennas and Propagation*, vol. 63, no. 6, pp. 2787–2090, Jun. 2015.

[22] R. E. Collin and S. Rothschild, "Evaluation of antenna Q," *IEEE Trans. on Antennas and Propagation*, vol. 12, no. 1, pp. 23–27, Jan. 1964.

[23] J. S. McLean, "A re-exmination of the fundamental limits on the radiation Q of electrically small antennas," *IEEE Trans. on Antennas and Propagation*, vol. 44, no. 5, pp. 672–676, May 1996.

[24] A. D. Yaghjian and H. R. Stuart, "Lower bounds on the Q of electrically small dipole antennas," *IEEE Trans. on Antennas and Propagation*, vol. 58, no. 10, pp. 3114–3121, Oct. 2010.

[25] W. Geyi, "A method for he evaluation of small antenna Q," *IEEE Trans. on Antennas and Propagation*, vol. 51, no. 8, pp. 2124–2128, Aug. 2003.

[26] A. D. Yaghjian and S. R. Best, "Impedance, bandwidth, and Q of antennas," *IEEE Trans. on Antennas and Propagation*, vol. 53, no. 4, pp. 1298–1324, Apr. 2005.

[27] P. Hazdra, M. Capek, and J. Eichler, "Comments to 'Reactive energies, impedance, and Q factor of radiating structures' by G. Vandenbosch," *IEEE Trans. on Antennas and Propagation*, vol. 61, no. 2, pp. 6266–6267, Dec. 2013.

[28] D. Tayli and M. Gustafsson, "Estimating antenna Q-factor from the MoM impedance matrix," in *Progress in Electromagnetics Research Symposium*, Prague, Czech Republic, 2015.

[29] J. Chalas, K. Sertel, and J. L. Volakis, "Q limits for arbitrarily shaped antennas using characteristic modes," *EUCAP*, pp. 1672–1673, 2011.

[30] J. Chalas, K. Sertel, and J. L. Volakis, "Compuation of the Q limits for arbitrarily shaped antennas using characteristic modes," *URSI*, pp. 772–774, 2011.

[31] M. Gustafsson, M. Cismasu, and B. L. G. Jonsson, "Physical bounds and optimal currents on antennas," *IEEE Trans. on Antennas and Propagation*, vol. 60, no. 6, pp. 2672–2681, Jun. 2012.

[32] M. Grant and S. Boyd, "CVX: Matlab software for disciplined convex programming, version 2.1," http://cvxr.com/cvx, Mar. 2014.

[33] M. Grant and S. Boyd, "Graph implementations for nonsmooth convex programs," in *Recent Advances in Learning and Control*, ser. Lecture Notes in Control and Information Sciences, V. Blondel, S. Boyd, and H. Kimura, Eds. Springer-Verlag Limited, 2008, pp. 95–110, http://stanford.edu/ boyd/graph_dcp.html.

[34] M. Capek, P. Hazdra, and J. Eichler, "A method for the evaluation of radiation Q based on modal approach," *IEEE Trans. on Antennas and Propagation*, vol. 60, no. 10, pp. 4556–4567, Oct. 2012.

[35] K. R. Schab, J. M. Outwater, Jr., M. W. Young, and J. T. Bernhard, "Eigenvalue crossing avoidances in characteristic modes," *IEEE Trans. on Antennas and Propagation*, to appear 2016.

[36] J. M. Outwater, Jr., K. R. Schab, and J. T. Bernhard, "Distinguishing physical and numerical crossing avoidances in characteristic mode analyses," in *Proc. 2015 Antenna Applications Symposium*, Monticello, IL, Sept. 2015.

[37] K. R. Schab and J. T. Bernhard, "Radiation and energy storage modes on conducting structures," *IEEE Trans. on Antennas and Propagation*, vol. 63, no. 12, pp. 5601–5611, Dec. 2015.

[38] S. M. Rao, D. R. Wilson, and A. W. Glisson, "Electromagnetic scattering by surfaces of arbitrary shape," *IEEE Trans. on Antennas and Propagation*, vol. 30, no. 3, pp. 409–418, May 1982.

[39] S. N. Makarov, *Antenna and EM Modeling with MATLAB*, 1st ed. Hoboken, New Jersey: Wiley, 2002.

[40] P. O. Persson and G. Strang, "A simple mesh generator in MATLAB," *SIAM Review*, vol. 46, no. 2, pp. 329–345, Jun. 2004.

[41] C. Geuzaine and J.-F. Remacle, "Gmsh: A three-dimensional finite element mesh generator with built-in pre- and post-processing facilities," *International Journal for Numerical Methods in Engineering*, vol. 79, no. 11, pp. 1309–1331, May 2009.

[42] K. R. Schab and J. T. Bernhard, "Analysis of optimized embedded antennas using radiation and energy storage modes," in *Progress in Electromagnetics Research Symposium*, Prague, Czech Republic, Jul. 2015.

[43] R. K. Eisenschitz, *Matrix Algebra for Physicists*, 1st ed. Plenum Press, 1966.

[44] P. Wriggers, *Computational Contact Mechanics*, 2nd ed. Springer, 2006.

[45] X.-Q. Sheng and W. Song, *Essentials of Computational Electromagnetics*. Singapore: John Wiley and Sons, 2012.

[46] MATLAB, *version R2014a*. Natick, Massachusetts: The MathWorks Inc., 2014.

[47] R. Kalaba, K. Spingarn, and L. Tasfatsion, "Individual tracking of an eigenvalue and eigenvector of a parameterized matrix," *Nonlinear Analysis, Theory, Methods, & Applications*, vol. 5, no. 4, pp. 337–340, Apr. 1980.

[48] M. Capek, L. Jelinek, and P. Hazdra, "On the functional relation between quality factor and fractional bandwidth," *Online*, Mar. 2014.

[49] B. D. Raines and R. G. Rojas, "Wideband characteristic mode tracking," *IEEE Trans. on Antennas and Propagation*, vol. 60, no. 7, pp. 3537–3541, Jul. 2012.

[50] Z. Miers and B. K. Lau, "Tracking of characteristic modes through far-field pattern correlation," in *Antennas and Propagation USNC/URSI National Radio Science Meeting, 2015 IEEE International Symposium on*, Jul. 2015, pp. 1470–1471.

[51] D. J. Ludick, J. v. Tonder, and U. Jakobus, "A hybrid tracking algorithm for characteristic mode analysis," *Electromagnetics in Advanced Applications (ICEAA), 2014 International Conference on*, pp. 455–458, Aug. 2014.

[52] S. R. Best, "A discussion on the quality factor of impedance matched electrically small antennas," *IEEE Trans. on Antennas and Propagation*, vol. 53, no. 1, pp. 502–508, Jan. 2005.

[53] N. L. Bohannon and J. T. Bernhard, "Design guidelines using characteristic mode theory for improving the bandwidth of PIFAs," *IEEE Trans. on Antennas and Propagation*, vol. 63, no. 2, pp. 459–465, Feb. 2015.

[54] J. T. Bernhard, J. J. Adams, M. D. Anderson, and J. M. Martin, "Measuring electrically small antennas: Details and implications," in *IEEE Workshop on Antenna Technology*, Mar. 2009, pp. 1–4.

[55] K. R. Schab and J. T. Bernhard, "Identifying radiation mechanisms on small objects using radiation modes," in *Proceedings of the 2015 Antennas and Propagation Symposium*, Vancouver, CA, Jul. 2015.

[56] J. A. Stratton, *Electromagnetic Theory*. New York: McGraw-Hill, 1941.

[57] L. Råde and B. Westergren, *Mathematics Handbook for Science and Engineering*, 5th ed. Springer, 2004.

[58] M. Gustafsson, C. Sohl, and G. Kristensson, "Illustrations of new physical bounds on linearly polarized antennas," *IEEE Trans. on Antennas and Propagation*, vol. 57, no. 5, pp. 1319–1327, May 2009.

[59] G. A. E. Vandenbosch, "Radiators in time domain - Part I: Electric, magnetic, and radiated energies," *IEEE Trans. on Antennas and Propagation*, vol. 61, no. 8, pp. 3995–4003, Aug. 2013.

[60] G. A. E. Vandenbosch, "Radiators in time domain - Part II: Finite pulses, sinusoidal regime, and Q factor," *IEEE Trans. on Antennas and Propagation*, vol. 61, no. 8, pp. 4004–4012, Aug. 2013.

[61] W. Geyi, "Stored energies and radiation Q," *IEEE Trans. on Antennas and Propagation*, vol. 63, no. 2, pp. 636–645, Dec. 2014.

[62] G. H. Golub and C. F. V. Loan, *Matrix Computations*, 3rd ed. John Hopkins University Press, 1996.

[63] K. R. Schab and J. T. Bernhard, "Classifying characteristic mode crossing avoidances with symmetry and energy coupling," in *Proceedings of the 2016 Antennas and Propagation Symposium*, Fajardo, Puerto Rico, Jul. 2016.

[64] M. Gustafsson and B. L. G. Jonsson, "Antenna Q and stored energy expressed in the fields, currents, and input impedance," *IEEE Trans. on Antennas and Propagation*, vol. 63, no. 1, pp. 240–249, Jan. 2015.

[65] T.-Y. Wu and K.-L. Wong, "On the impedance bandwidth of a planar inverted-f antenna for mobile handsets," *Microwave and Optical Technology Letters*, vol. 32, no. 4, pp. 249–251, 2002.

[66] A. T. Arkko, "Effect of ground plane size on the free-space performance of a mobile handset pifa antenna," in *ICAP 2003, International Conference on Antennas and Propagation*, vol. 1, Mar. 2003, pp. 316–319.

[67] K. R. Schab and J. T. Bernhard, "Examining finite ground plane effects using advanced techniques," in *Proc. 2015 Antenna Applications Symposium*, Monticello, IL, Sept. 2015.

[68] N. Inagaki and R. J. Gabacz, "Eigenfunctions of composite Hermitian operators with application to discrete and continuous operators," *IEEE Trans. on Antennas and Propagation*, vol. 30, no. 4, pp. 571–575, Jul. 1982.

[69] D. M. Pozar, "Antenna synthesis and optimization using weighted Inagaki modes," *IEEE Trans. on Antennas and Propagation*, vol. 32, no. 2, pp. 159–165, Feb. 1984.

[70] J. J. Adams and J. T. Bernhard, "Broadband equivalent circuit models for antenna impedances and fields using characteristic modes," *IEEE Trans. on Antennas and Propagation*, vol. 61, no. 8, pp. 3985–3994, Aug. 2013.

[71] R. H. Clarke, "A statistical theory of radio reception," *Bell System Technical Journal*, vol. 47, no. 6, pp. 957–1000, Aug. 1968.

[72] R. G. Vaughan, "Signals in mobile communications: A review," *IEEE Transactions on Vehicular Technology*, vol. 35, no. 4, pp. 133–145, Nov. 1986.

[73] R. G. Vaughan and J. B. Andersen, "Antenna diversity in mobile communications," *IEEE Transactions on Vehicular Technology*, vol. 36, no. 4, pp. 149–172, Nov. 1987.

[74] S. Blanch, J. Romeu, and I. Corbella, "Exact representation of antenna system diversity performance from input parameter description," *Electronics Letters*, vol. 39, no. 9, pp. 705–707, May 2003.

[75] C. B. Dietrich, K. Dietze, J. R. Nealy, and W. L. Stutzman, "Spatial, polarization, and pattern diversity for wireless handheld terminals," *IEEE Trans. on Antennas and Propagation*, vol. 49, no. 9, pp. 1271–1281, Sept. 2001.

[76] M. Pascolini, S. Oh, C. DiNallo, and M. Midrio, "Envelope correlation coefficient and mean effective gain for multiple antennas in different use cases," in *Antennas and Propagation, 2007. EuCAP 2007. The Second European Conference on*, Nov. 2007, pp. 1–7.

[77] K. R. Schab and J. T. Bernhard, "Beamforming with radiation modes of finite ground planes excited by heterogeneous arrays," in *URSI National Radio Science Meeting*, Boulder, CO, Jan. 2016.